LIGHT INDUCED EFFECTS IN OXIDE SEMICONDUCTORS

By

SYEED EHSAN AHMED

A dissertation submitted in partial fulfillment of
the requirements for the degree of

DOCTOR OF PHILOSOPHY

WASHINGTON STATE UNIVERSITY
Materials Science and Engineering

JULY 2022

To the Faculty of Washington State University:

The members of the Committee appointed to examine the dissertation of SYEED EHSAN AHMED find it satisfactory and recommend that it be accepted.

Matthew D. McCluskey, Ph.D., Chair

John S. McCloy, Ph.D.

Yi Gu, Ph.D.

ACKNOWLEDGMENT

Bismillah. I want to express my gratitude to my parents, Kaiser, and Parveen, for their unwavering support. Tamanna, my partner, for always being there for me. Friends and family who have always encouraged me to pursue my dreams.

My lab mates for always being willing to provide a helping hand. Violet Poole and Jesse Huso for all the lab training sessions and discussions.

My committee members, Dr. John McCloy, and Dr. Yi Gu.

Finally, my advisor, Dr. Matthew D. McCluskey for his guidance and patience. Believing in me and providing a platform for me to accomplish my goals.

The financial support from the National Science Foundation. This study was supported by the National Science Foundation (NSF) under Grant No. DMR-1561419 and Grant No. DMR-2109334.

LIGHT INDUCED EFFECTS IN OXIDE SEMICONDUCTORS

Abstract

by Syeed Ehsan Ahmed, Ph.D.
Washington State University
July 2022

Chair: Matthew D. McCluskey

Titanium dioxide (TiO_2) has many promising applications, including photocatalysis, hydrogen production, and solar cells. In this study, anatase TiO_2 was annealed in a vacuum at 800 ℃, resulting in a conductive thin film. Exposure to subgap laser light caused a seven order-of-magnitude increase in resistance. Laser-irradiated regions showed an increase in optical transmission, consistent with a reduction in oxygen vacancy concentration. Scanning electron microscopy and Raman spectroscopy indicate that laser irradiation did not change the morphology, composition, or phase of the material.

Defining the crystal phase of oxide semiconductors using a sub-bandgap laser could benefit transparent electronics. This work reports laser-induced localized phase transitions of TiO_2 thin films. A Raman map of the anatase E_g mode (144 cm^{-1}) and rutile A_g mode (608 cm^{-1}) revealed the formation of crystalline microstructures due to the laser treatment. Laser irradiation under vacuum results in an anatase-to-rutile phase transition. Irradiating the rutile region in air changes the crystal structure back to anatase, despite the thermodynamic stability of rutile. The results suggest that irradiated photons are absorbed by defects, resulting in localized electronic excitation that leads to a mixture of amorphous and crystalline regions. The phase of the crystalline regions depends strongly on the ambient conditions.

Carbon is one of the most recurring contaminants known to alter the properties of a material. The form of carbon in the sputtered TiO_2 thin films appeared undetectable to Raman spectroscopy. Annealing the films under vacuum results in Raman peaks at 1350 (D) and 1585 cm^{-1} (G), representing disorder and graphitic C=C bonds. Secondary ion mass spectrometry (SIMS) revealed a substantial amount of carbon in the sputtered films that persist after annealing. Irradiating the annealed sample with a subgap laser in air dissipates carbon locally.

Barium calcium titanate ($Ba_{1-x}Ca_xTiO_3$) annealed under a flowing humid 2% hydrogen gas mixture exhibits room temperature persistent photoconductivity (PPC) with a subtle increase in conductivity when exposed to visible light. Hydrogen in the annealing atmosphere induces PPC, implying that the process is analogous to that of PPC in $BaTiO_3$. Annealing the samples in air erased the PPC effect, indicating that the process is reversible.

TABLE OF CONTENTS

LIST OF TABLES

Page

LIST OF FIGURES

Page

Dedication

To my sunshine, Tamanna.

CHAPTER ONE: INTRODUCTION

The discovery, research, and engineering of semiconductors enabled the development of advanced electronics. Semiconductors are crucial components of devices used in a range of industries. Almost all modern electronics, including microelectronics, transistors, and junction technology rely on semiconductors. Before the emergence of the semiconductor transistor, vacuum tubes were important electronic devices. J. A. Fleming invented the first two-electrode thermionic vacuum tube in 1904,[1] which set the stage for the age of modern electronics. Lee De Forest 1906 created the Audion, a vacuum tube device that can amplify electrical signals.[2] J. Brattain and W. Bardeen created the first point-contact junction transistor in 1947,[3] while W. Shockley suggested the bipolar junction transistor (BJT) in 1948.[4,5] The transistor is widely regarded as one of the most significant inventions. The junction field-effect transistor (JFET) was the first field-effect transistor device to be successfully manufactured.[6] It replaced vacuum tubes with solid-state semiconductors, paving the way for compact and affordable electrical devices.

Oxide semiconductors are drawing much interest as next-generation semiconducting materials, adding unique features to modern electronics due to their distinct electrical structure and functional properties. Wide bandgap oxide semiconductors combine the properties of high conductivity and optical transparency in a single material.[7,8] These wide bandgap semiconductors are transparent in the visible spectrum. Titania (TiO_2), a wide bandgap transparent conducting oxide (TCO), is the primary focus of this dissertation. TCOs are preferred materials for "invisible electronics".[9–11]

In the present work, laser irradiation and characterization techniques were used to process and study thin-film TiO_2 and bulk $Ba_{1-x}Ca_xTiO_3$. The first chapter explains the fundamentals of semiconductors and provides a brief overview of the materials that were used. The methodologies and instrumentation used to characterize the materials are described in the second chapter. The third chapter covers the crystal growth techniques for thin film and single crystal semiconductors. The chapter also includes experimental procedures performed during sample preparation. The core emphasis of our study is detailed in chapter four, which describes the laser irradiation technique to introduce localized photo-induced resistivity and phase transitions in TiO_2 thin films. The chapter also discusses carbon contamination in thin-film oxide semiconductors and laser treatment as a potential candidate for minimizing contamination. The fifth chapter summarizes the findings on thin-film TiO_2 research and addresses prospective future works. Finally, chapter six describes room temperature persistent photoconductivity in $Ba_{1-x}Ca_xTiO_3$.

1.1: Introduction to semiconductors

In terms of electrical conductivity, materials are classified as conductors, insulators, or semiconductors. A conductor, or metal, is a substance that permits electricity to pass through it. In a conductor, electrons or ions can flow readily with an applied voltage. An insulator, on the other hand, is a material that prevents electric current from flowing freely due to tightly bound electrons that cannot move in response to an electric field. A semiconductor is a material whose electrical properties fall between conductors and insulators. Semiconductors are neither good conductors nor good insulators. They contain a small number of free electrons that depends on the doping level.

A basic understanding of matter is essential in understanding how semiconductors function. Atoms are made up of electrons, protons, and neutrons. A conductor must contain free electrons that can move between the atoms. These electrons come from the atoms outer orbit and are known as *valence electrons*. These valence electrons in the outer orbits are loosely bound to the nucleus. As a result, pulling an electron from the outermost orbits requires considerably less energy.

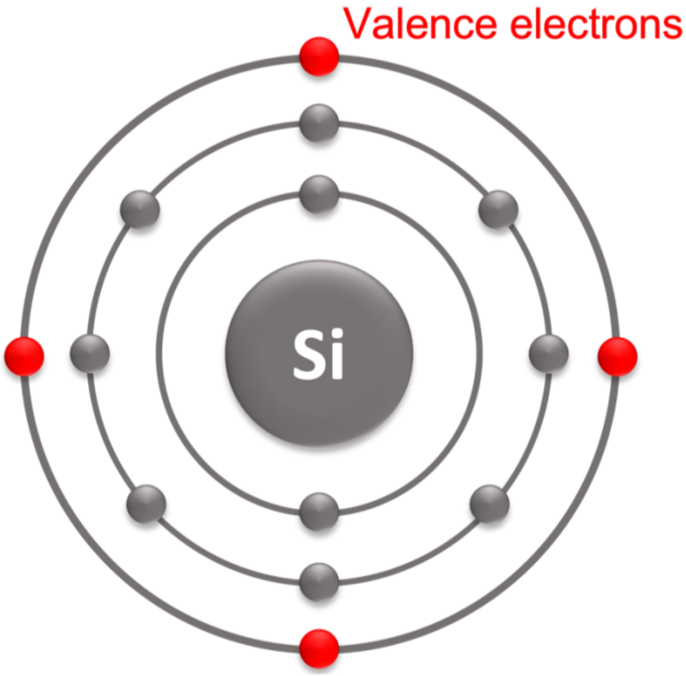

Figure 1.1: Atomic structure of silicon.

Semiconductors are divided into two major categories called intrinsic semiconductors and extrinsic semiconductors. An intrinsic semiconductor is a pure semiconductor. It has a band structure where the valence band comprises states filled with electrons. In contrast, the conduction band has unoccupied empty states at absolute zero temperature. The valence band maximum (VBM) is the highest level in the valence band. The conduction band minimum (CBM) is the lowest energy point in the conduction band. The bandgap is the energy difference between the VBM and CBM.

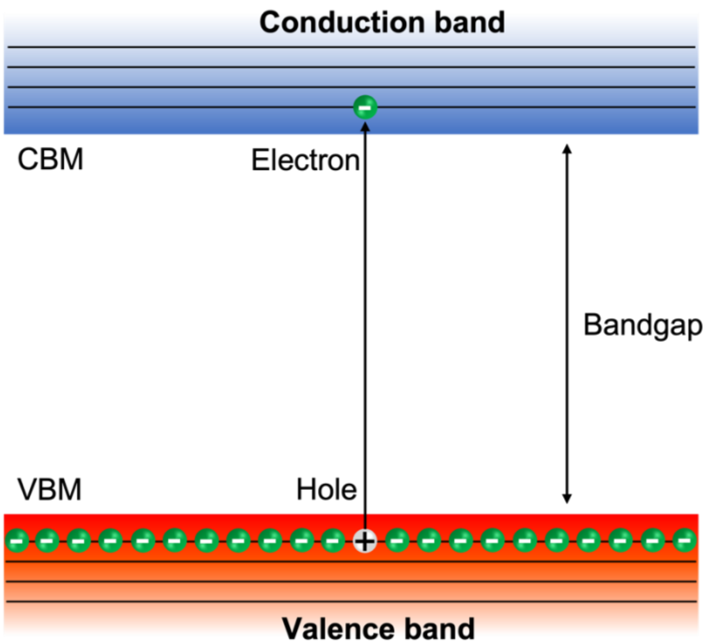

Figure 1.2: Schematic diagram of the band structure. An electron from the valence band is excited to the conduction band, leaving a positively charged hole behind.

An electron can be thermally excited to the conduction band, allowing it to move freely in the crystal. As a result of the electronic transition, a space is created in the valence band. The unoccupied positively charged space is known as a hole. Neighboring electrons in the valence band can readily migrate to fill the spot. Hence, holes in a semiconductor can travel across the lattice similarly to electrons, carrying a positive charge.

Electrons can also be excited from the valence band to the conduction band using electromagnetic radiation. A photon with energy equal to or greater than the bandgap energy can be absorbed by the semiconductor, creating an electron-hole pair. The excited electron tends to relax back to the valence band by emitting a photon. The underlying process is known as radiative recombination,[12] where an electron-hole pair is annihilated. The semiconductor is transparent for photon energies below the bandgap energy, where the incoming photon can transmit through.

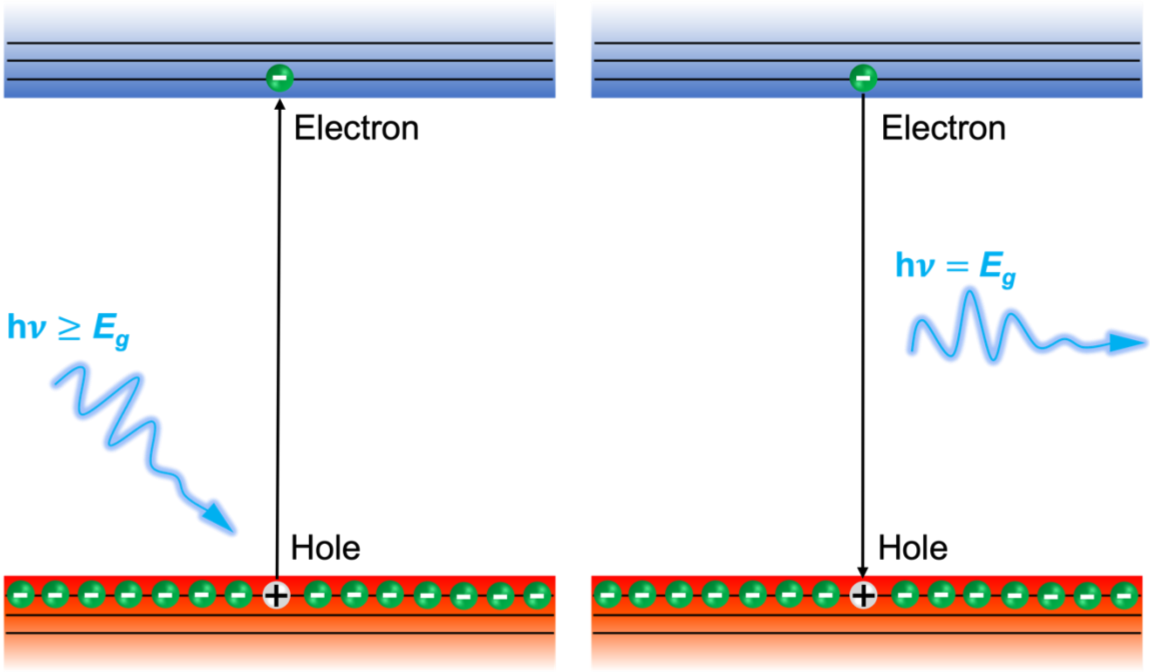

Figure 1.3: Energy diagram of photon-assisted excitation of an electron from the valence band to the conduction band. The electron tends to relax back to the valence band with the emission of a photon of equivalent energy.

There are two primary types of bandgaps for semiconductors: direct bandgaps and indirect bandgaps. Crystal momentum, expressed as the wavevector or **k**-vector in the Brillouin zone, distinguishes these two bandgap types. In a direct gap semiconductor, a photon is absorbed to excite an electron by forming an electron-hole pair. The transition takes place without the electron wavevector **k** significantly changing. The bandgap energy of such semiconductors at threshold frequency is simply the vertical transition between the CBM and VBM. However, CBM in an indirect bandgap semiconductor occurs at $\mathbf{k} \neq 0$. In general, the CBM and VBM have different **k**'s. A photon and a phonon are both involved in the indirect transition to conserve momentum. The phonon energy (meV) is minimal compared to the bandgap energy of the semiconductor, which results in almost horizontal changes in the band diagram. The indirect transition energy is given by

$$E_g = \hbar\omega + \hbar\Omega \tag{1.1}$$

Here $\hbar\Omega$ is the phonon contribution, where Ω is the frequency of the emitted phonon.

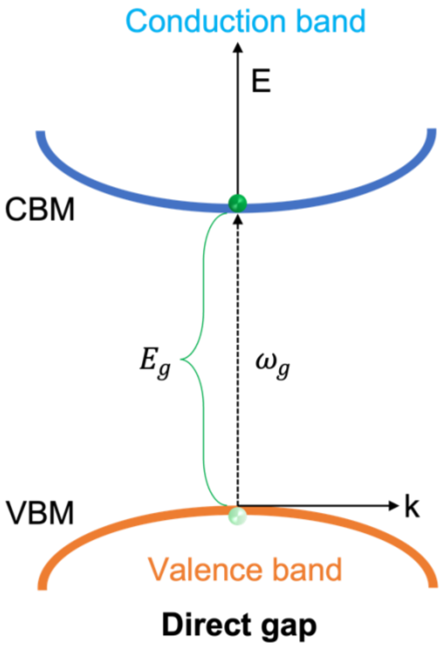

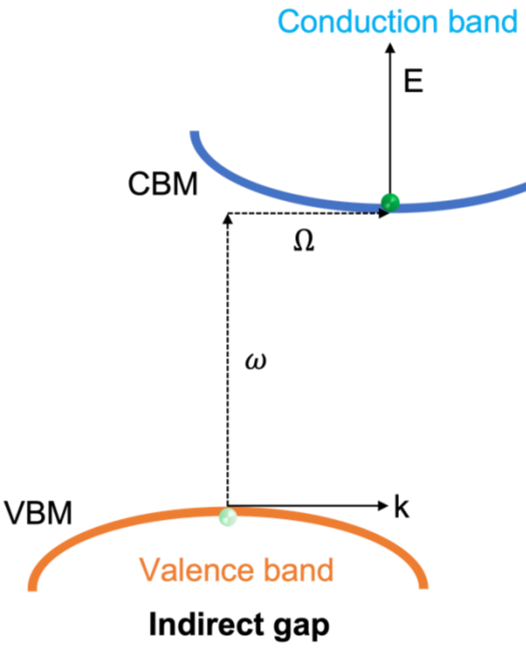

Figure 1.4: Direct and indirect optical absorption comparison.

An extrinsic semiconductor is just an intrinsic semiconductor that has been doped. Doping is a process of adding impurity to alter the properties of a semiconductor significantly. An impurity is referred to as a donor if it has more valence electrons than the atom it substitutes. The impurity atom is an acceptor if it possesses fewer electrons than the host atom. Semiconductors with excess donor electrons are called *n*-type semiconductors. A doped semiconductor with excess holes is referred to as *p*-type. In a *p*-type semiconductor, the number of acceptors exceeds the total number of donors. Both *n*-type and *p*-type semiconductors leverage the excess electrons and holes in the lattice to enhance their conductivity.

Defects can introduce electronic levels into the bandgap, impacting device performance and modifying the properties. Shallow defect states are near the conduction or valence band and can donate or accept electrons easily. Defect states are involved in several electronic transitions (Fig. 1.5). An electron can be readily excited from the shallow donor at room temperature. Similarly, a shallow acceptor has an energy state near the valence band and can easily accept an electron, leaving a hole behind. A deep defect requires a large amount of energy to add or remove electrons to or from the defect level.

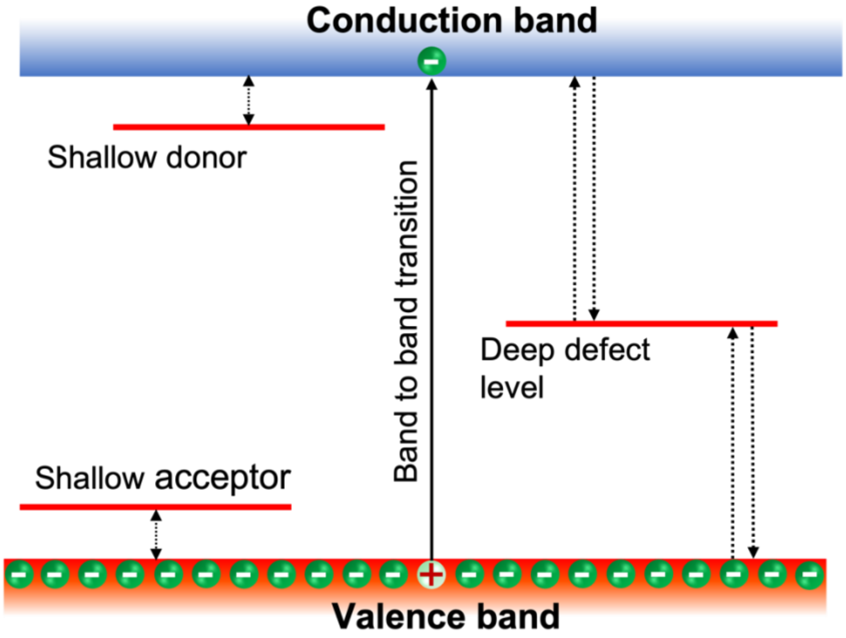

Figure 1.5: Defect states in the bandgap.

Defects in semiconductors can significantly alter their characteristics. Crystallographic defects are disruptions in a crystal's regular pattern. Crystallographic defects are divided into four categories: point defects, line defects, area defects, and volume defects. The subjects for consideration in this study include point defects and complexes. Point defects appear solely at or near a single lattice point. The defect is considered native if it only involves the atoms of the host crystal and extrinsic if it involves impurity atoms. Point defects are divided into four following categories:

1. *Vacancy* defects are unoccupied lattice sites that would be occupied in a perfect crystal. A vacancy or pair of vacancies is also referred to as a Schottky defect.

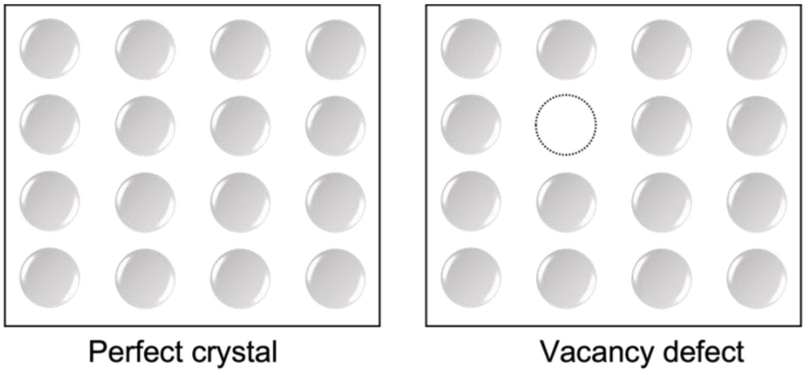

Figure 1.6: Vacancy point defect.

2. *Interstitial* defects are within the same crystal; one or more original atoms are displaced from the original lattice location to the interstitial position.

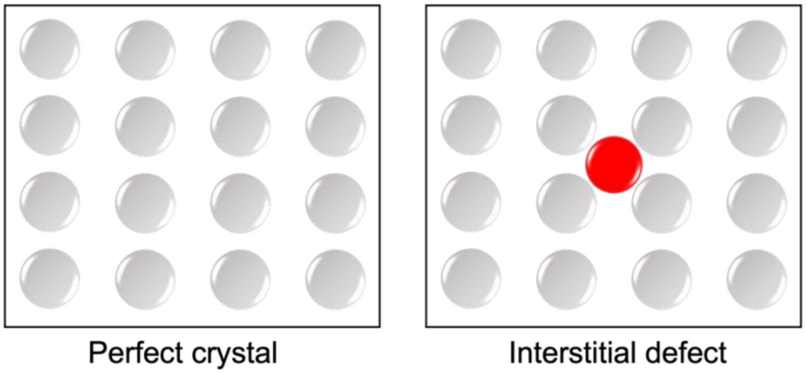

Figure 1.7: Interstitial point defect.

3. *Substitutional* defects arise when the original atom in a crystalline lattice point gets replaced with a substitute atom.

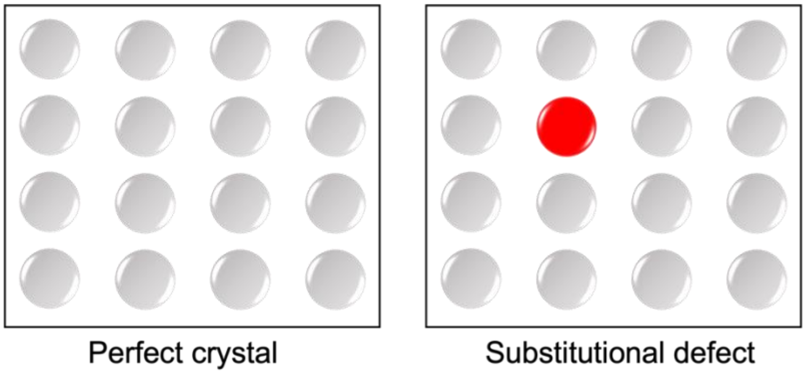

Figure 1.8: Substitutional point defect.

4. *Frenkel* defects are a composite of both vacancy and interstitial point defects. It occurs whenever an ion moves from its site to an interstitial location in the same crystal.

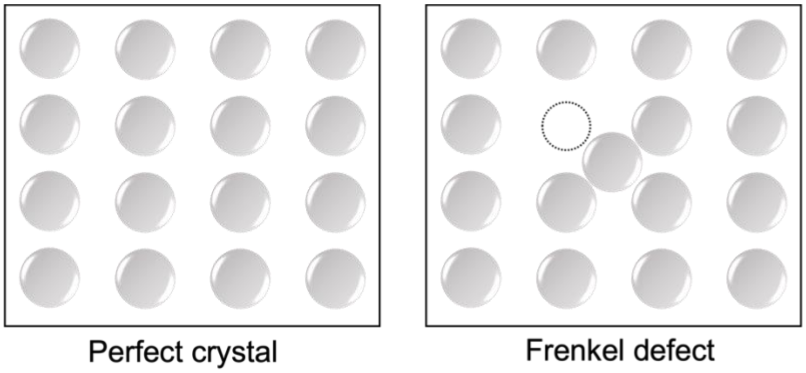

Figure 1.9: Frenkel point defect.

1.2: Oxide semiconductors

Oxide semiconductors are a promising class of engineered materials, found in various crystal forms, and show a wide range of electrical and optical characteristics. The invention of oxide-based semiconductor devices has made significant advances, notably in transparent electronics and optics.[13] Oxide semiconductors are pushing the boundaries of traditional semiconducting devices and paving the way for new fields such as thin-film transistors (TFTs),[14–17] liquid-crystal, and organic-light-emitting diode displays[18,19] and paper electronics.[20,21] Oxides are relatively inexpensive, robust, and chemically stable in ambient conditions.[22]

Metal oxide semiconductors (MOS) have attracted considerable interest in optoelectronic applications primarily due to their visible to near UV range transparency. Materials that transmit light while also conducting electricity are crucial in developing photovoltaic cells, displays, and photodiodes. Visibly transparent semiconductors require a large bandgap to prevent incident photons from being absorbed. Insulators typically have large bandgaps, whereas conventional semiconductors, which can easily carry electricity, have relatively narrow bandgaps that do not permit visible light to pass through. Oxides form native point defects that generate sub-bandgap energy levels due to oxygen vacancy and cation interstitials, form donors, and contribute to the oxide's enhanced conductivity. As a result, despite the large bandgap, transparent conducting oxides (TCO) combine optical transparency and high electrical conductivity.

Thin-film cadmium oxide (CdO), discovered in 1907, was the first transparent conductive oxide reported. However, tin-doped indium oxide (ITO) is the most used transparent conductive oxide semiconductor and is the costliest. As a result, aluminum-doped zinc oxide (AZO) and indium-doped cadmium oxide have been used as substitute materials. This material group has already established numerous potential uses in devices that require a transparent junction. Some applications include transparent contacts for solar cells and increased output in light-emitting diodes.

1.3: Titanium dioxide (TiO_2)

Titania, or titanium dioxide (TiO_2), is an inorganic compound. TiO_2 has a molecular weight of 79.9 g/mol and typical chemical composition of 59.9 wt% titania and 40.1 wt% oxygen. Metal titanium is one of the most common and abundant elements that can spontaneously react with surface oxygen to form titanium oxides. Titanium, which is bound to six oxygen anions, displays octahedral geometry. TiO_2 is an optically transparent wide bandgap semiconductor that exhibits various chemical and physical characteristics depending on its crystal structure.[23] It is polymorphic and contains three unique crystalline phases: anatase, rutile, and brookite. Anatase shows enhanced catalytic properties[24–29] as the electrons in anatase behave as free electrons rather than polarons.[30–32] Rutile, on the other hand, features a large refractive index at visible wavelengths and exhibits a notable high birefringence as well as strong dispersion. Anatase is stable at nanoscale crystallite sizes, but the rutile phase is most stable in bulk form.

Titanium dioxide (TiO_2) is a well-studied metal-oxide-semiconductor with applications in chemistry, electronics, and medicine.[33–39] TiO_2 is nontoxic, affordable, simple to deposit, and biocompatible. TiO_2 is a prime candidate for use in hydrogen generation, water purification, catalysis, and air purification.[40–44] TiO_2 is widely used in solar cells, optically functional coatings, memory devices, and microelectronic capacitors because of its high dielectric constant, large refractive index, resistivity, and simplicity of mass manufacture.[45–47]

Anatase TiO_2 exhibits photocatalytic activity when irradiated by an ultraviolet (UV) source. Akira Fujishima first discovered the photocatalytic properties of TiO_2 in 1967.[42,48] According to subsequent studies, this photoactivity is particularly prominent at anatase {001} planes.[49,50] Inorganic nanotubes and nanowires can be synthesized using anatase TiO_2.[51] Biphasic titanium dioxide has improved functionality as a photocatalyst since interfaces among rutile and anatase are thought to boost photocatalytic properties by allowing charge carrier segregation.[52] Additionally, thin-film TiO_2 is used as a reflecting optical coating for dielectric screens due to its large index of refraction.

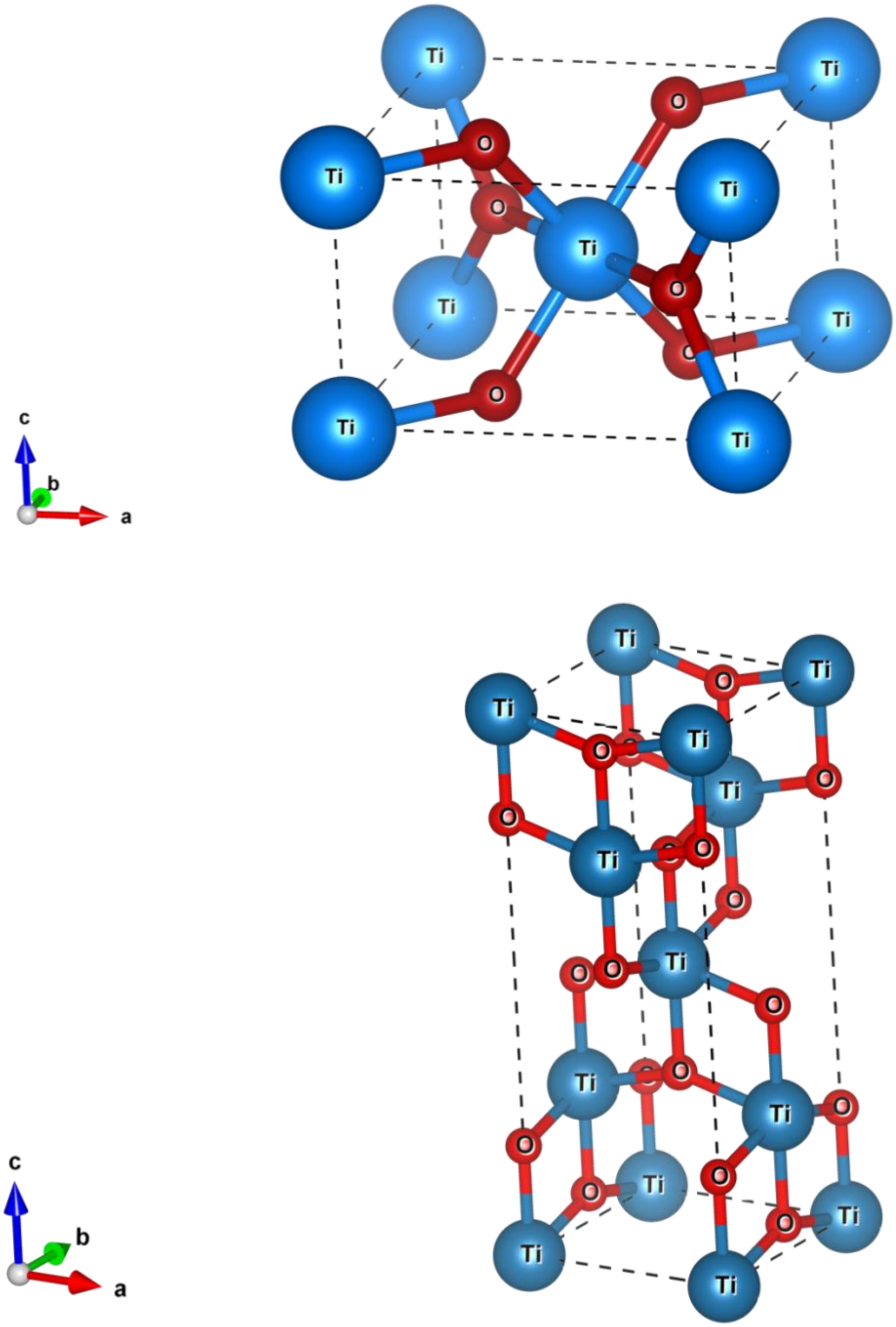

Figure 1.10: Crystal structure models for TiO_2. Top: Rutile. Bottom: Anatase.

Anatase is typically the initial phase to develop during TiO_2 synthesis.[53,54] This could be due to the less-constrained molecular structure[55] and the lower surface free energy of anatase relative to rutile. The phase transition from anatase to rutile (ART) involves nucleation and growth processes.[56,57] The transition is reconstructive, implying that the process is not instant and requires breaking and repairing bonds.[57–60] The transition kinetics are known to be influenced by several factors, including contaminants, processing methods, morphology, and heat transfer conditions. In pure anatase, rutile may nucleate at anatase twin interfaces[56,61] as these sites resemble rutile structurally. The dynamics of the anatase to rutile transition are significantly influenced by oxygen defect levels, with oxygen vacancies promoting the transformation.[57,62–64] On the other hand, rutile is more stable than anatase at all temperatures and pressures (Fig. 1.11). As a result, the transition to rutile is irreversible. This is supported by thermodynamic investigations,[65–69] which suggest negative pressures would be necessary for such a transition.[58]

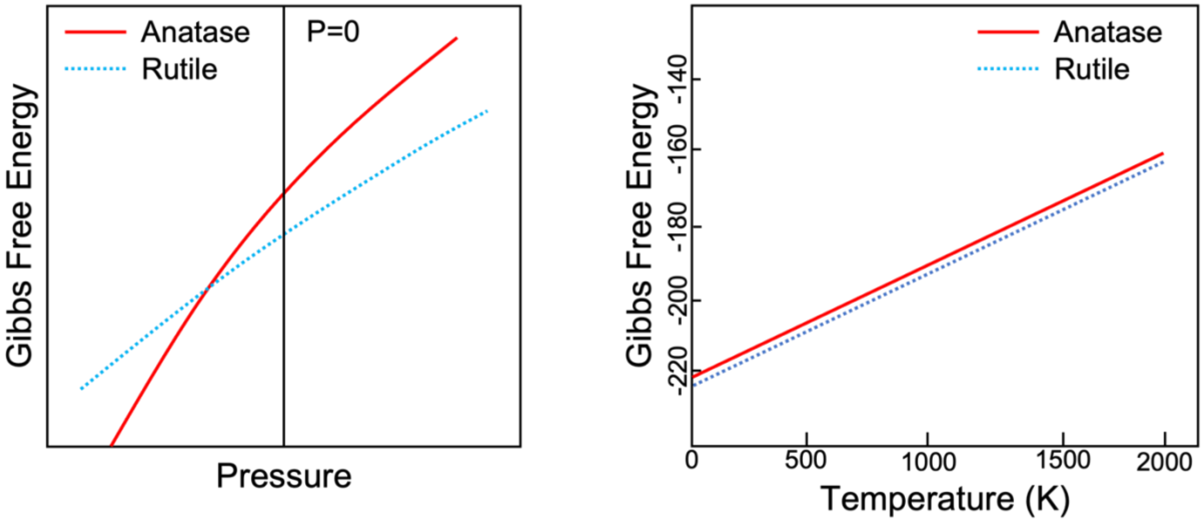

Figure 1.11: Schematic plots of Gibbs free energy versus pressure[58] and temperature[70] of anatase and rutile TiO_2. [Hanaor et al., 2011]

The most explored TiO_2 phases are anatase, rutile, and a combination of anatase-rutile. Despite having a higher bandgap, anatase outperforms rutile in photocatalytic activity. Anatase has an indirect bandgap, whereas rutile has a direct bandgap. The indirect bandgap of anatase aids in photoinduced electron-hole pair recombination latency.[71] Furthermore, since anatase has the lowest average effective mass compared to rutile excitons, anatase can efficiently migrate to the interface to participate in photoreduction and photooxidation processes.[72] Anatase-rutile mixtures demonstrate enhanced photocatalytic and reduction.[73] The anatase-rutile heterojunction facilitates carrier segregation, prolonging the electron-hole separation interval.

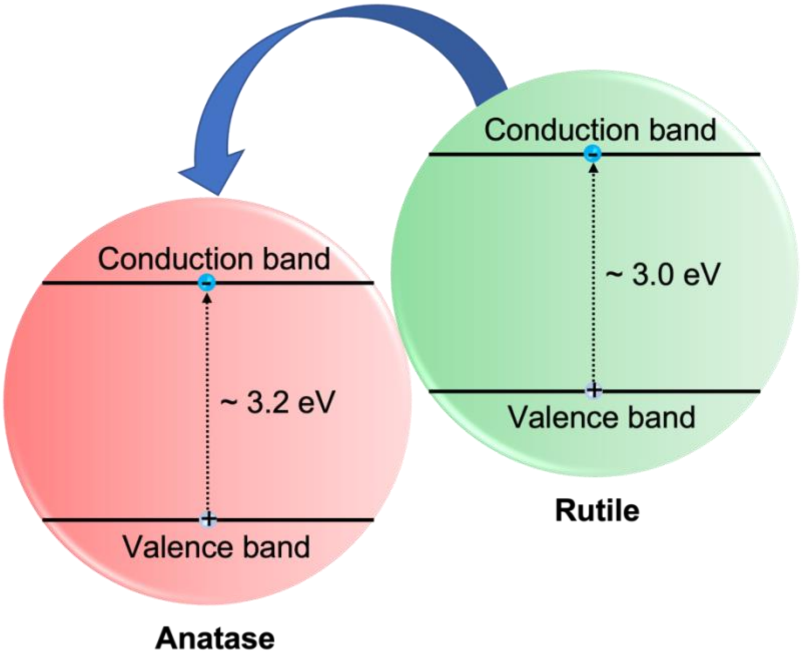

Figure 1.12: Schematic of heterojunction in an anatase-rutile mixture.

Oxygen vacancies, titanium vacancies, and titanium interstitials are the known intrinsic point defects in TiO_2.[74–76] They are essential for the majority of TiO_2 surface reactions, such as photocatalysis.[77,78] One of the most critical aspects of this work is the formation of oxygen vacancies (V_O). An oxygen vacancy is simply the absence of an oxygen ion at its lattice site.[79,80] TiO_2 can shed oxygen under specific atmospheric conditions, resulting in oxygen vacancies. Such vacancies can potentially alter the electrical and chemical properties of the material and are known for contributing to the formation of Ti^{3+} point defects. These titanium defects are known for participating in crystal charge transport[81]:

$$\mathrm{Ti}^{4+} - \mathrm{O} - \mathrm{Ti}^{4+} \rightarrow \mathrm{Ti}^{3+} - V_{\mathrm{O}} - \mathrm{Ti}^{3+} + \frac{1}{2}\,\mathrm{O}_2 \qquad (1.2)$$

Concentration of V_O decreases in presence of higher oxygen partial pressures

$$\mathrm{Ti}^{3+} - V_{\mathrm{O}} - \mathrm{Ti}^{3+} + \mathrm{O}_2 \rightarrow \mathrm{Ti}^{4+} - \mathrm{O} - \mathrm{Ti}^{4+} \qquad (1.3)$$

Bridging oxygen vacancies are formed during vacuum annealing of TiO_2. Heat treatment generates surface oxygen vacancies and Ti^{3+} defects.

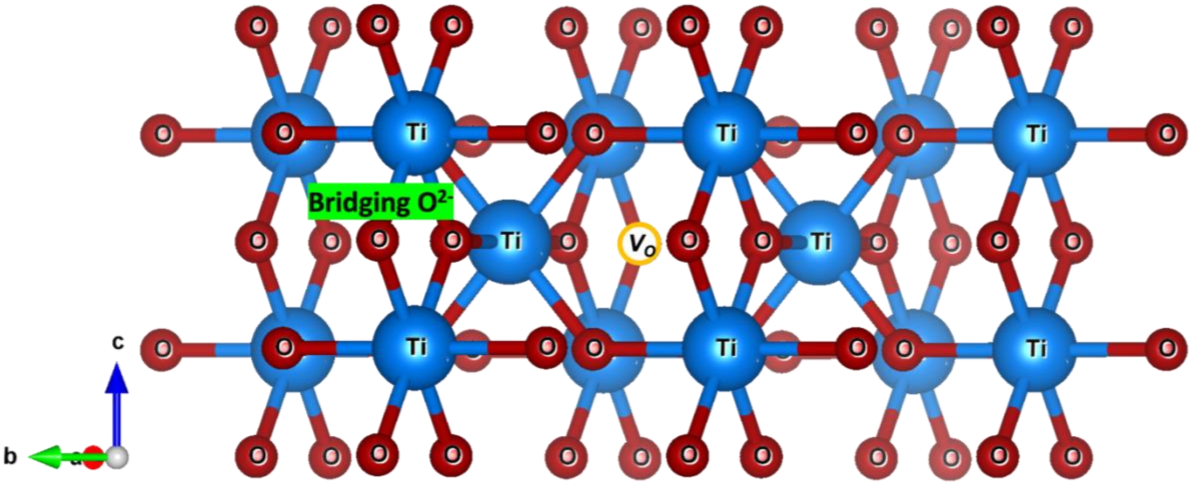

Figure 1.13: Depiction of bridging oxygen vacancy in rutile TiO_2.

1.4: Barium calcium titanate ($Ba_{1-x}Ca_xTiO_3$)

Barium titanate, $BaTiO_3$ (BTO) is a well-known transparent perovskite lead-free ferroelectric material that is used in electronic devices due to its large dielectric constant, robust ferroelectricity, and piezoelectric characteristics.[82–84] The local displacement of Ti atoms is known for driving the ferroelectricity and dielectric responses in BTO.[85,86] Perfect BTO crystals have small piezoelectric coefficients and low Curie temperatures (T_c = 120 ℃).[87] Doping the pure BTO crystal with calcium to form a barium calcium titanate ($Ba_{1-x}Ca_xTiO_3$, BCT) ceramic solid solution has sparked considerable interest due to its electromechanical properties. The substitution of barium with calcium in BTO (Fig. 1.14) enhances the electrical and mechanical responses of the host crystal. It prevents the onset of the unwanted hexagonal non-ferroelectric phase from forming, allowing the formation of large single crystals. The substitution stabilizes the tetragonal phase, which is the active phase at ambient temperatures.[88,89]

Persistent photoconductivity (PPC) is a light-induced photocurrent that persists after the illumination source is cut off. Room temperature PPC in strontium titanate (STO) was introduced by sub-bandgap light (~2.9 eV).[90] BTO showed a similar PPC effect after illumination.[91] Oxygen and hydrogen are the critical components responsible for inducing PPC in STO,[92] where a hydrogen atom inside an oxygen vacancy shifts to an interstitial site adjacent to a strontium vacancy, releasing an electron to the conduction band during the process. The model may also be able to explain the kinetics behind room temperature PPC in BCT.

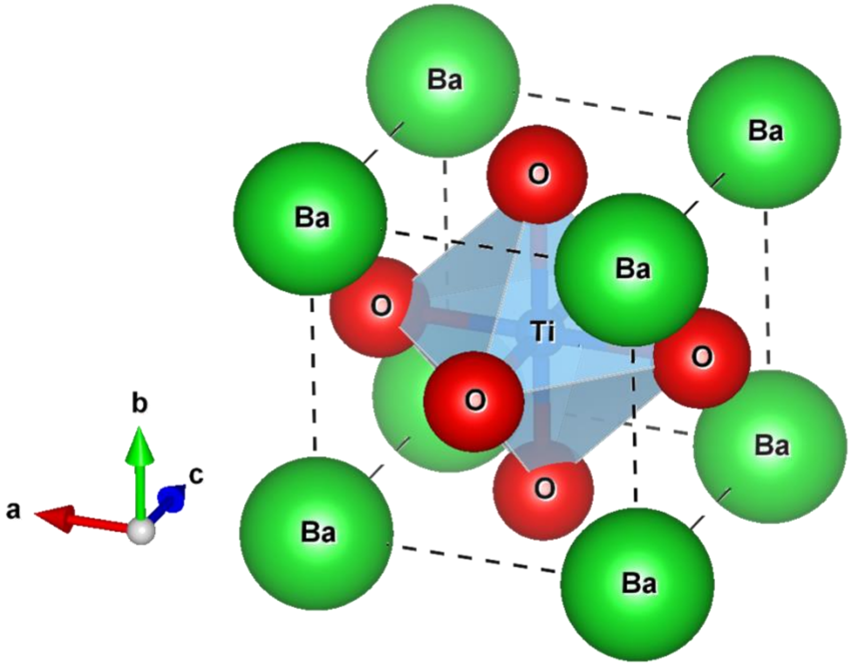

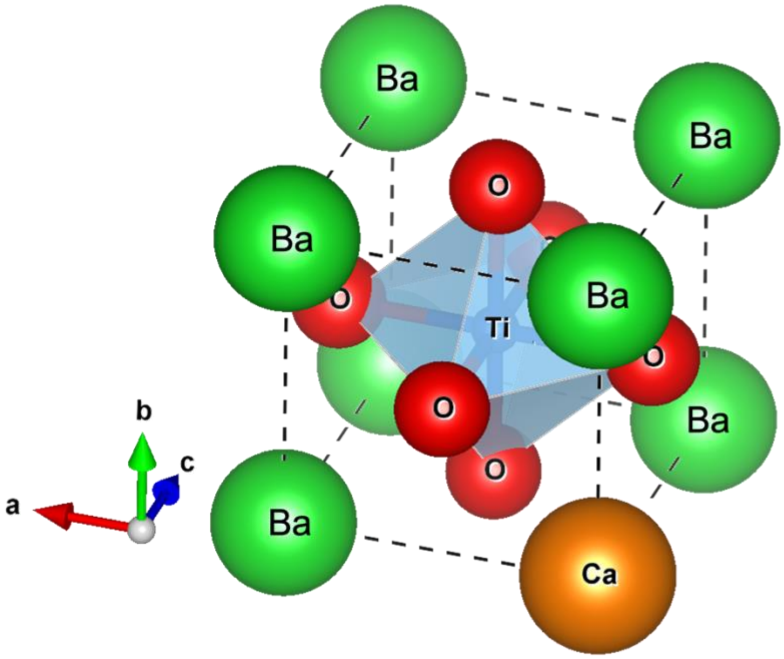

Figure 1.14: Crystal structure models for $BaTiO_3$ *(top) and* $Ba_{1-x}Ca_xTiO_3$ *(bottom).*

CHAPTER TWO: EXPERIMENTAL TECHNIQUES

2.1: Raman spectroscopy

C. V. Raman, an Indian physicist, discovered the Raman effect in 1928.[93] Raman spectroscopy is a widely used method to determine the vibrational modes of molecules. It is a technique for non-destructive chemical analysis that offers extensive information on chemical structure and molecular interactions.[94] As a result, it is commonly employed to generate a structural fingerprint to identify chemical compounds.[95]

Raman is a light scattering technique. *Rayleigh scattering* occurs whenever a source of monochromatic light, often a laser, is incident on a molecule and is elastically dispersed with the same wavelength as the incoming photons. However, Raman scattering occurs when a tiny percentage of photons are scattered inelastically with different wavelengths depending on the chemical composition of the material. It encompasses Stokes Raman scattering, in which the incoming photon excites a vibrational mode, and anti-Stokes scattering, in which the photon gains energy thermally.[96]

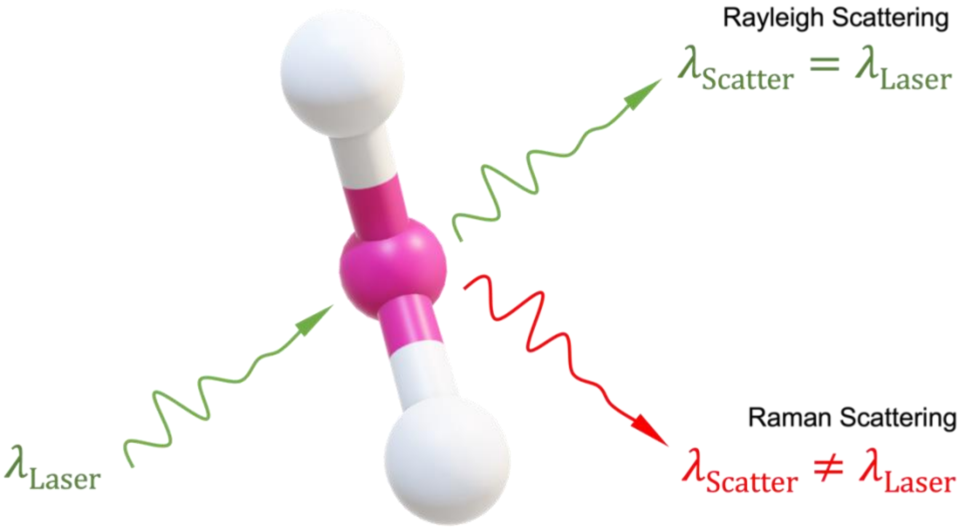

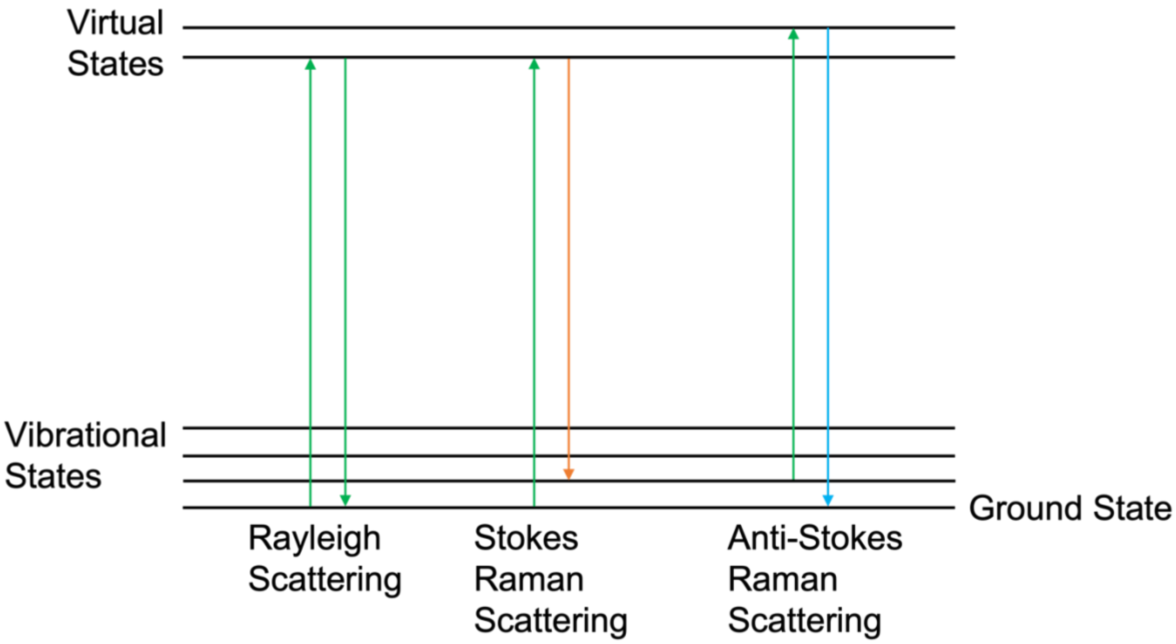

Figure 2.1: Schematic of the Raman principle.

A material's polarization P is related to its polarizability α and incident electric field E.

Here,

$$E = E_0 \cos(\omega_0 t) \tag{2.1}$$

$$P = \alpha E_0 \cos(\omega_0 t) \tag{2.2}$$

The normal mode oscillation of atoms at frequency ω_ϑ is given by

$$x = x_0 \cos(\omega_\vartheta t) \tag{2.3}$$

Taylor expanding the polarizability α and combining equations 2.1 – 2.3,

$$P = \alpha E_0 \cos(\omega_0 t) + \left(\frac{\delta\alpha}{\delta x}\right) x_0 E_0 \cos(\omega_\vartheta t) \cos(\omega_0 t) + \cdots \tag{2.4}$$

Re-writing the 2nd term of equation 2.4 using a trigonometric identity,

$$P = \alpha E_0 \cos(\omega_0 t) + \left(\frac{1}{2}\right)\left(\frac{\delta\alpha}{\delta x}\right) x_0 E_0 \left[\{\cos(\omega_0 - \omega_\vartheta)t\} + \cos(\omega_0 + \omega_\vartheta)t\right] + \cdots \tag{2.5}$$

The first term in equation 2.5 describes *Rayleigh scattering.* Raman scattering at two distinct frequencies described in the second term, where $(\omega_0 - \omega_\vartheta)$ and $(\omega_0 + \omega_\vartheta)$ are called the Stokes and anti-Stokes frequencies.

A schematic diagram of Raman spectroscopy is shown in Figure 2.2. To illuminate the sample, a strong laser excitation source is used, which transmits through a beam splitter. Only the inelastic scattered photons, which contain the vibrational information, return through the beam splitter into the monochromator, and finally to the detector. Low-intensity Raman signals are detected while excitation photons are suppressed by a notch filter. To demonstrate the related modes, the Raman intensity is represented as a function of wavenumber.

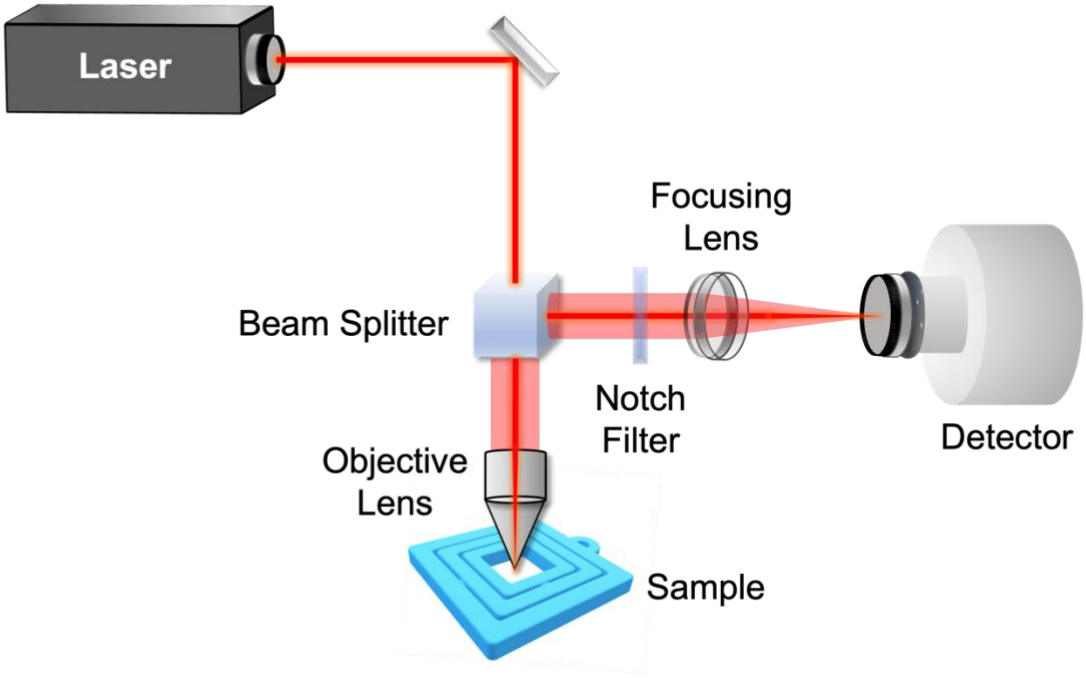

Figure 2.2: Schematic diagram of a Raman spectroscope.

The Raman scattering experimental setup is almost identical to photoluminescence (PL). However, Raman signals are much weaker than PL signals. As a result, Raman scattering typically requires substantially longer acquisition times. Resonance Raman spectroscopy is a

Raman enhancement technique for increasing the strength of the signal. The laser excitation frequency is selected to be near the frequency of an electronic transition in the material. Resonance Raman can increase the intensity of Raman scattering by a factor of 10^2-10^6 and maximize the signal-to-noise ratio.

Raman mapping is a technique for creating precise images based on the Raman spectrum of a material. Compared to Raman spectroscopy, which gives information at distinct positions within the sample, Raman mapping provides spectroscopic information combined with spatial data. The laser light scans the sample area with a predetermined step size and the Raman spectrum is recorded for each pixel on the sample. These data are then analyzed to generate Raman images with structural and compositional information about the material.

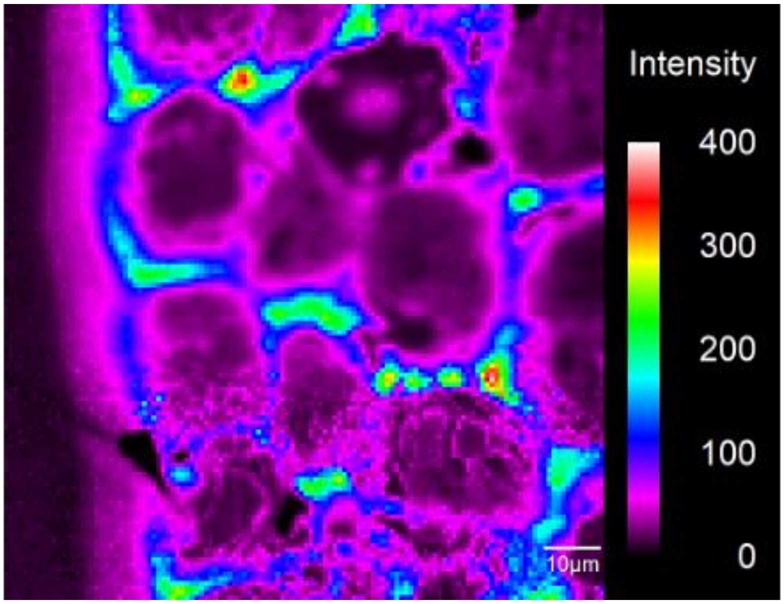

Figure 2.3: Raman map of a TiO_2 thin film.

2.2: Fourier transform IR (FTIR) spectroscopy

Fourier-transform infrared (FTIR) spectroscopy is a technique for obtaining an infrared spectrum of absorption or emission. FTIR spectroscopy is non-invasive, sensitive, and precise.

FTIR has a wide array of applications in identifying compounds and determining components. Compared to a scanning grating spectrometer, which detects intensity through a narrow slit. FTIR acquires high-resolution across a broad spectrum with high signal-to-noise ratios.

The Michelson interferometer serves as the basis for an FTIR. A beam splitter divides a beam of collimated infrared light. The rays bounce off a stationary mirror and a moving mirror with a precisely regulated pathlength. The beam splitter combines the two beams and is fed to the detector through the sample. The phase differences cause interference, and the output signal is called an interferogram.

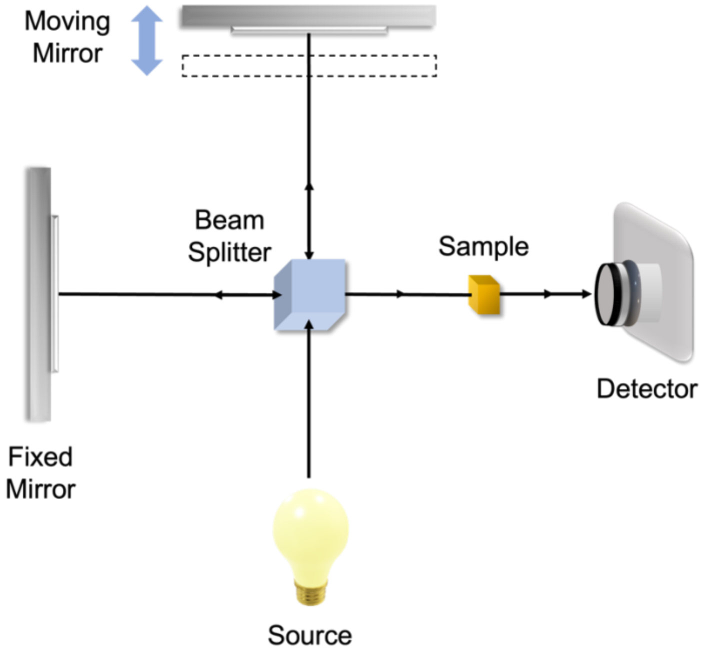

Figure 2.4: Fourier transform infrared spectrometer (FTIR).

This interferogram signal includes information across all detected frequencies simultaneously. The detector processes the interferogram signals, and the system performs fast Fourier transforms (FFT) to convert the data into a spectrum.

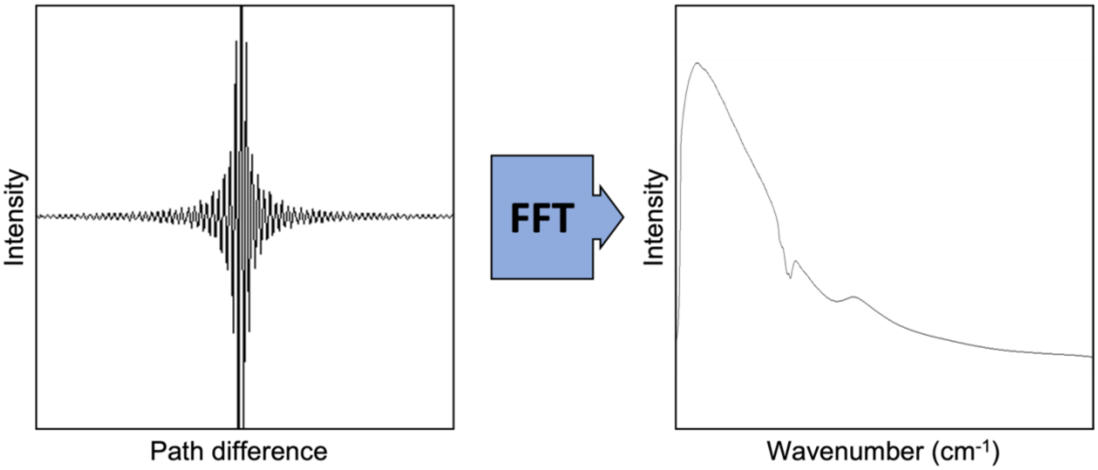

Figure 2.5: Fourier transformation of an interferogram into a spectrum.

FTIR measurements are significantly quicker than dispersive techniques, which use a monochromator to scan across frequencies independently. Besides averaging over multiple scans, FTIR facilitates scanning in a relatively short period and boosts the signal significantly. FTIR has a far higher throughput than grating-based systems, which rely on narrow slits for resolution. In contrast, the resolution of FTIR instruments is related to the length of the mirror travel.

2.3: UV/Visible spectroscopy

UV-Vis spectroscopy is a broadly adopted method in many fields of research and technology. The technique relies on light and is relatively inexpensive and easily implemented. UV-Vis spectroscopy is a spectroscopic method that correlates and analyzes the amount of UV or visible photons absorbed or transmitted by a material to the intensity of light passing through a reference sample or blank. It compares the light intensity before (I_0) and after (I) it travels through the medium. The I/I_0 ratio gives the transmittance T. The absorbance A is based on the transmittance and is given by

$$A = \log\left(\frac{1}{T}\right) \tag{2.6}$$

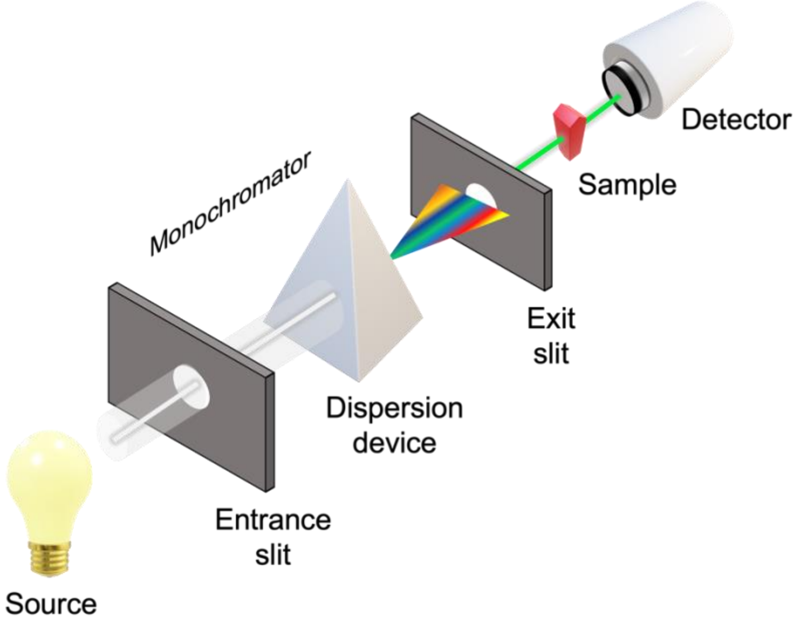

Figure 2.6: Schematic diagram of a UV/Visible spectroscope.

The Perkin Elmer Lambda 900 UV/VIS/NIR spectrometer with a double-beam, double monochromator ratio recording device was used for this study. The spectrometer is equipped with tungsten-halogen and deuterium lamps as sources. The wavelength ranges between 190 and 3300 nm, with 0.08 nm and 0.3 nm accuracy in the UV and near-IR zones. The deuterium lamp is the UV source, while the tungsten lamp is the visible/near-IR source. The spectrometer detects wavelengths spanning from 200 to 3300 nm. The photomultiplier tube (PMT) is used to detect photons in the UV visible ranges, whereas a lead sulfide (PbS) detector detects light in the infrared (IR) region. The spectrometer disperses light into a spectrum with 1440 lines/mm in the UV Visible and 360 lines/mm in the near-IR using holographic gratings. The spectrometer can readjust the light source and detectors automatically. The scans in this study were performed at a resolution of 1 nm and an integration time of 1 sec/nm.

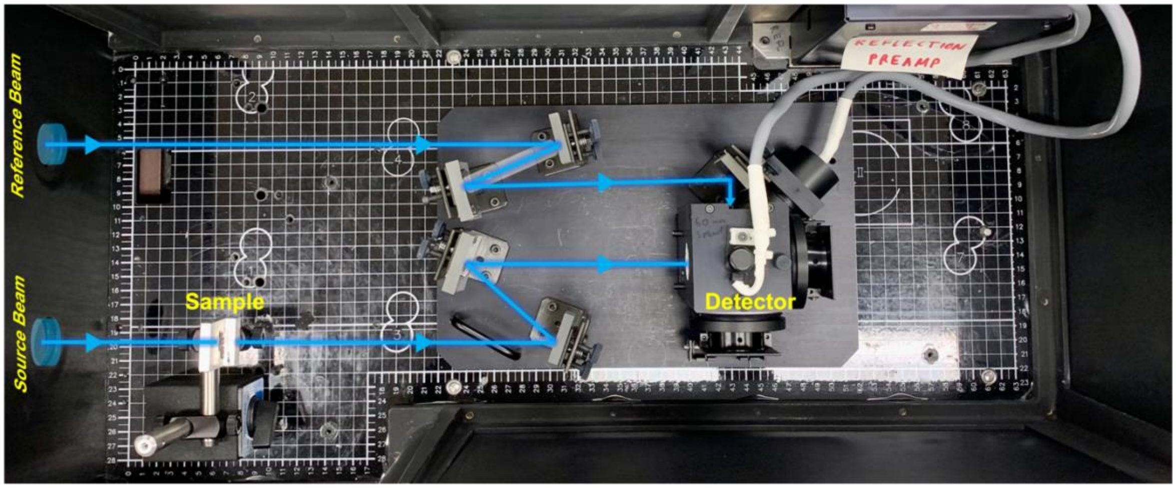

Figure 2.7: Perkin Elmer Lambda 900 UV/Vis/NIR.

UV/Vis spectroscopy is essential for probing the defect levels in semiconductors. The method is non-destructive, enabling the sample to be reused or analyzed multiple times. Measurements can be obtained quickly, and the data generally requires minimal processing. Drawbacks associated with the method include light scattering and interference.

2.4: Hall effect

The Hall effect measures the potential difference using a magnetic field perpendicular to the charge flux. It is an excellent method for determining the electrical properties of semiconductors like resistivity, carrier density, carrier type, and mobility.

The Hall effect is a result of the Lorenz force. Charge carriers deflect and accumulate on the edges in the presence of an external magnetic field, as seen in Fig. 2.8. As a result, an observable quantity known as the Hall voltage is formed, which is then used to compute the electrical characteristics of the sample.

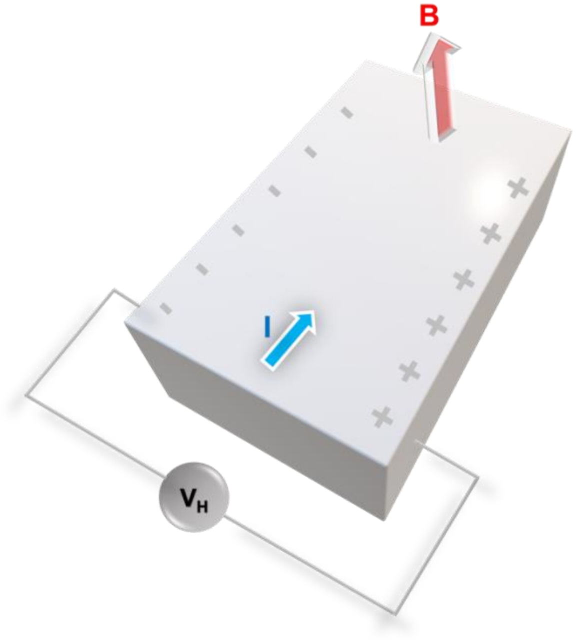

Figure 2.8: Schematic diagram of the Hall effect.

The Hall effect is measured using a four-probe method. The method is suited to samples that are homogeneous and free of spatial flaws, since imperfections on the surface may result in incorrect results. Four small ohmic contacts are put on the sample, which is mounted to the Hall stage. A current is applied between points 1 and 2, and the potential difference between points 3 and 4 is measured. This is for resistivity. For Hall, with magnetic field B on, different combinations are measured. This measurement is repeated with combinations of applied current and voltage contact points.

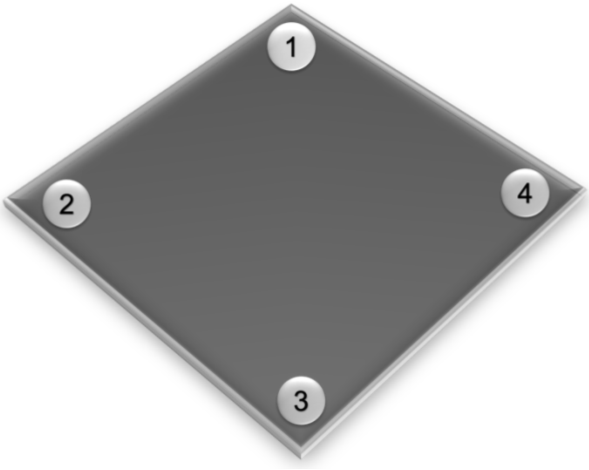

Figure 2.9: Contact geometry.

A variable temperature Hall measuring device was used to acquire the Hall effect data for this study. The sample was mounted on a stage equipped with a thermocouple and heating wire using a small amount of thermal paste. The temperature is controlled using an MMR K2000 digital temperature controller that can be adjusted from 80 to 700 K. The Hall effect measurement was performed using the MMR H5000 controller.

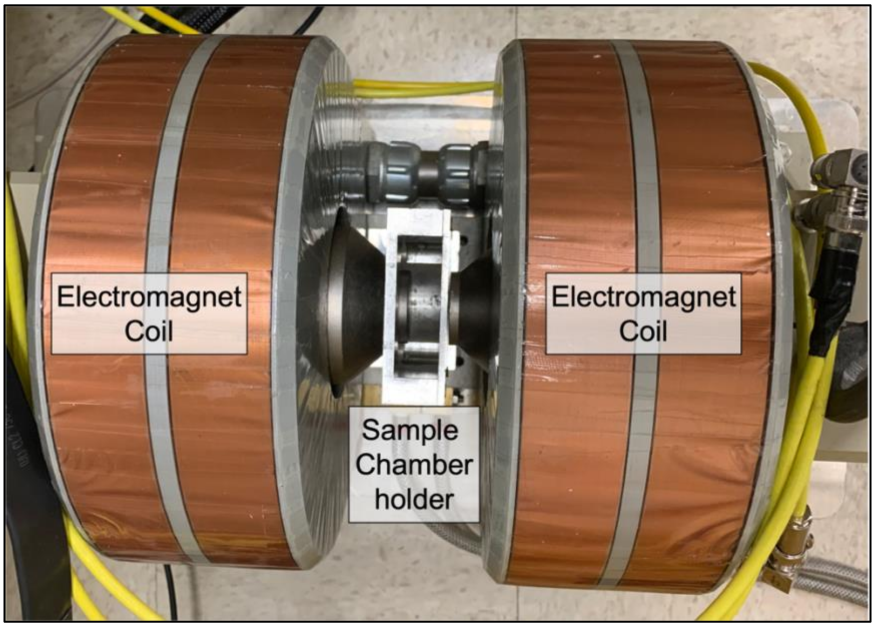

Figure 2.10: MMR Hall effect measurement tool.

2.5: Scanning electron microscopy (SEM)

A scanning electron microscope (SEM) is an electron microscope that creates images by focusing a beam of high-energy electrons. It was first developed in the early 1950s. The SEM is a microscope that produces sample images using electrons instead of light. In an optical microscope, the wavelength of the light used for illumination determines how sharply the microscope can focus. As a result, the wavelength became the limiting element in optical microscopes. This led to the development of the electron microscope, since electrons have far shorter wavelengths, allowing for higher resolution. In SEM, electrons collide with atoms in the sample, generating data that reveal information on the sample's morphology and chemical composition.

In a scanning electron microscope, electrons interact with atoms at varying depths of the material, creating a variety of signals such as secondary electrons, backscattered electrons, and characteristic X-rays. When the electron beam strikes the surface of a sample, it penetrates to a depth determined by the applied potential, ejecting secondary electrons and X-rays collected by detectors to generate a picture of the sample.

When an electron from a higher energy level fills an inner-shell vacancy, an electron known as the Auger electron may be emitted. The primary beam impacting the sample causes Auger electrons to be created from the top atomic layer. These electrons carry surface-sensitive information for an analysis depth of a few nanometers. Inelastic scattering between the primary electron beam and the sample produces secondary electrons. A low-energy electron’s small mean free path limits it to the top few nanometers of the sample surface. As a result, secondary electrons are emitted from the sample surface and are highly localized, allowing images of the specimen surface to be collected at nm resolutions. Back-scattered electrons are reflected from a sample due to the elastic scattering. These energetic electrons originate from deeper regions of the sample and can provide information like the crystal structure and orientation.

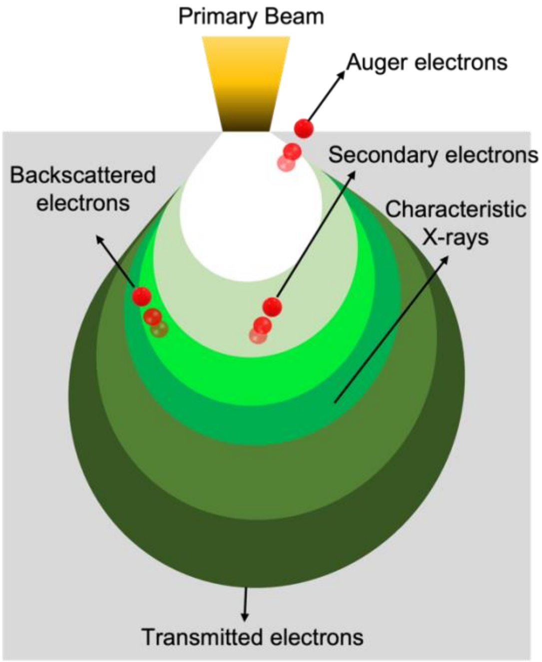

Figure 2.11: Electron-matter interaction volume and the generated signals.

X-rays are produced by inelastic collisions between incident electrons and electrons in the sample. When an inner shell electron is stripped from the material by the energetic electron beam, a higher-energy electron fills the shell, resulting in the emission of characteristic X-rays. The energy of these characteristic X-rays can be detected using energy-dispersive X-ray spectroscopy and used to map the distribution and chemical composition.

Electron microscopy works by scanning a sample surface area with electron beams in a raster pattern. An electron gun generates a beam of electrons, which is then collimated using the anode plate that attracts the electrons and accelerates through the column using the magnetic lens. The condenser lens regulates the beam size and the number of electrons in the beam, which determines the image resolution. The electron beam travels vertically through the microscope, enclosed in a vacuum, preventing molecules or atoms from colliding with the energetic electron beam. This ensures better imaging quality with minimal noise and vibrations. A combination of lenses, electromagnetic fields, and apertures are utilized to focus the electron beam. The scanning coils farther down the line redirect the beam along the axes, allowing a raster scan. The objective lens focuses the beam to a small point on the sample.

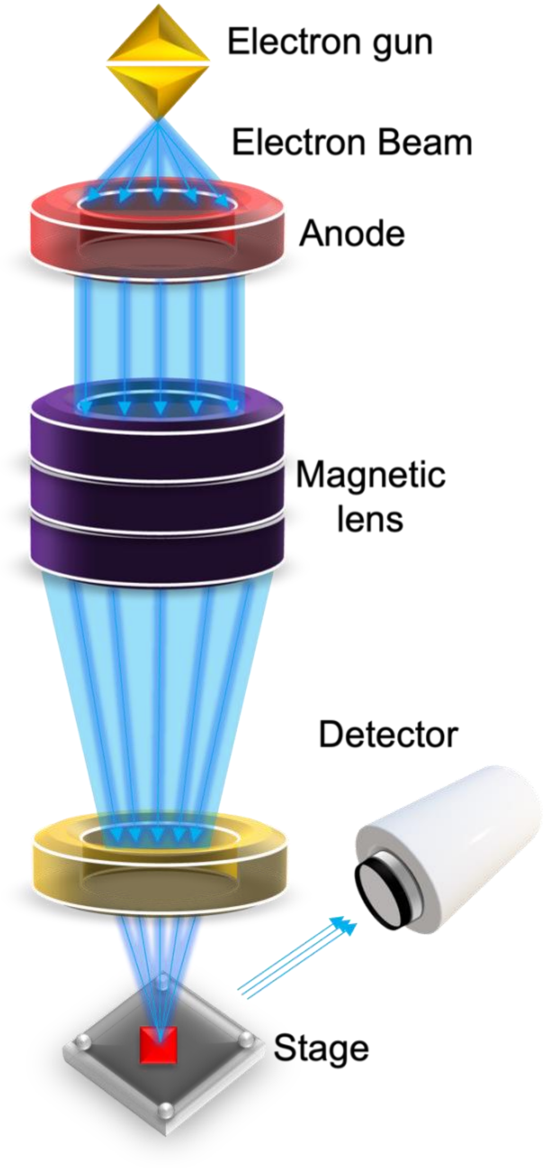

Figure 2.12: Schematic diagram of an SEM.

2.6: Additional techniques

The microscopic and spectroscopic techniques summarized below were performed in the current study.

2.6.1: Atomic force microscopy (AFM)

Atomic force microscopy is a versatile and accurate method used to examine materials. AFM scans in three dimensions and provides surface measurements. AFM can generate imaging resolution on the angstrom scale and can image practically any surface. In an AFM, a motorized tip "touches" the surface to obtain information about the material. Piezoelectric components enable accurate and precise movements for precision scanning.

An AFM produces images by scanning a cantilever across the sample surface with a very sharp tip. The attractive force between the surface and the pointed tip causes the cantilever to deflect toward the surface as it approaches the surface. However, when the end contacts the surface, electrostatic repulsive force kicks in and pushes the cantilever away from the surface. The deflections are measured by reflecting an incident laser beam off the cantilever's flat top.

2.6.2: X-ray photoelectron spectroscopy (XPS)

X-ray photoelectron spectroscopy (XPS) is a method for examining the surface chemistry of a material. XPS is a photoelectric effect based surface-sensitive quantitative spectroscopic method. XPS can determine a material's chemical state, electronic structure, and atomic composition.

XPS spectra are created by irradiating a sample surface with a monochromatic X-ray beam and calculating the resulting kinetic energy of electrons emitted by the sample. A spectrum is constructed by measuring emitted electrons at various kinetic energies. The emission energies are characteristic for different elements and charge states.

2.6.3: Secondary ion mass spectrometry (SIMS)

Secondary ion mass spectrometry (SIMS) is used to investigate the composition of solid surfaces and thin films by etching them with a focused primary ion beam and then examining the ejected secondary ions using a mass spectrometer. SIMS depth profiles with excellent detection limits and depth resolution can identify very low concentrations of dopants and contaminants.

The energetic primary beam provides enough energy to ionize the sample surface, and ions created by this process from the secondary beam are then accelerated to a mass spectrometer in a high vacuum environment. As a result, SIMS is the tool of choice for various analytical tasks. On the other hand, SIMS is destructive due to the strong primary beam, and samples must be vacuum compatible. The EAG Laboratories carried out all of the SIMS analyses for this investigation.

2.6.4: Photoluminescence (PL) and photoluminescence excitation (PLE) spectroscopy

Photoluminescence (PL) spectroscopy is a non-destructive, contactless method for studying a material's electronic structure. Photoexcitation is a process involving absorption of the incident photons and exciting the electrons to a higher energy state. The electron is then in an energetically excited state. These states are unstable; eventually, the system will revert to its initial condition by releasing excess energy. The electrons can return to the lower energy state by radiating the extra energy in the form of a photon, a process known as photoluminescence.

In PL, the sample is illuminated using a fixed wavelength source, and the emitted photons are funneled via a monochromator and into a detector. Photoluminescence excitation (PLE) is a method that is like photoluminescence but functions in the opposite direction. A monochromator in PLE varies the incident wavelength while the detector only detects a particular wavelength of the emitted light.

CHAPTER THREE: SEMICONDUCTOR GROWTH AND PROCESSING

3.1: Thin film growth

A thin film is a layer of material that ranges in thickness from nanometers to typically less than a micrometer. Thin film deposition is the technique of depositing an engineered layer of material on a substrate material. These films can be made of a range of materials, including metals, oxides, and compounds. Thin films show a wide range of properties that can be used to alter or improve the chemical, electrical, optical, and physical characteristics of the substrate material.

Thin film deposition is a critical manufacturing step. Films can be deposited using a range of methods, and a variety of instruments and equipment can be used to ramp up and improve the film deposition process.[97–99] Film deposition methodology can be classified into two basic groups based on the type of the process: physical or chemical.

3.1.1: Physical vapor deposition (PVD)

Physical vapor deposition (PVD) refers to a class of thin-film growth that includes vaporizing a solid material in a vacuum and depositing it as a condensed phase on a substrate. PVD comprises a range of techniques used to deposit thin films and coatings. The most common PVD techniques are sputtering, evaporation, ion plating, and pulsed laser deposition.

3.1.1.a: Sputtering

Sputtering is a process for depositing thin films that has been used extensively in the scientific and industrial community to make various commercial and consumer-based products. W.R. Grove first invented the sputtering process as a coating technology in 1852. Sputtering is typically utilized because of its ease of usage, capacity to deposit a wide range of materials, and excellent scalability. The TiO_2 thin film studied in Chapter 4 was deposited using sputtering.

When an energetic ion collides with an atom of a target, it causes an exchange of momentum and a collision cascade. Such cascades can follow various trajectories. If the residual energy exceeds the target's surface binding energy, an atom is ejected. This phenomenon is referred to as sputtering.

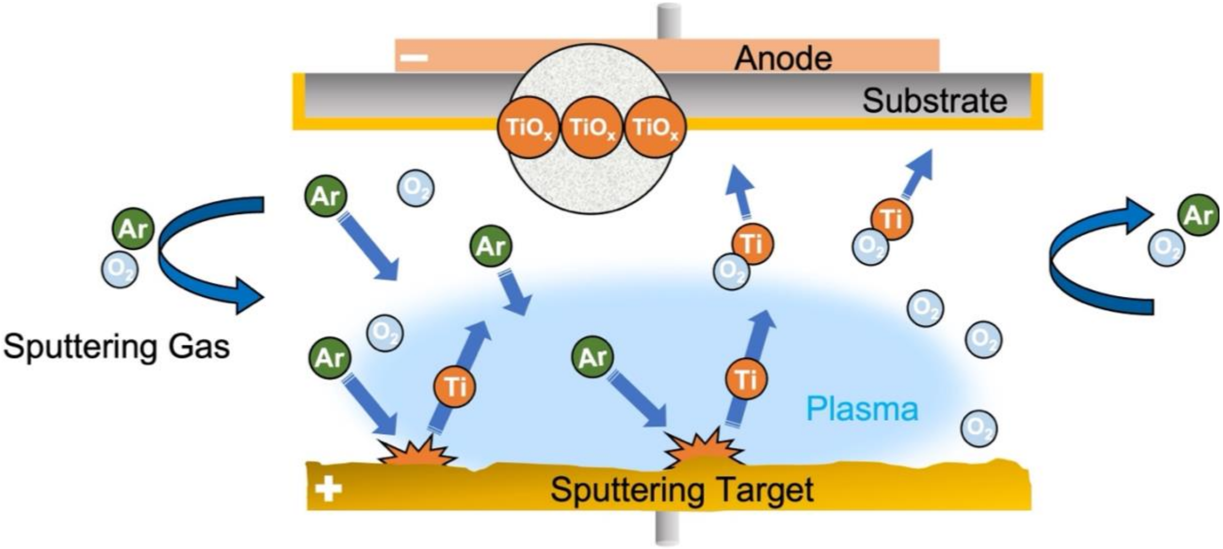

Figure 3.1: Schematic diagram of the sputtering process.

A negative anode and a positive cathode are placed opposite each other inside a sputtering chamber. On the anode, a target of the desired coating substance is mounted, and the substrates to be coated are placed on the cathode. The chamber is then evacuated and a functional gas like argon is introduced. When an electric field is applied across the terminals, it causes a cascade of ionization of the gas, forming a plasma. The applied electric field directs the plasma towards the target, bombarding and knocking ions off the target. The ejected atoms then move to the substrate and deposit a thin layer of the target substance.

Typically, a direct current (DC) power source is used for a conductive target. Unfortunately, in case of an insulating material, the target is unable to disperse the incoming current. It accumulates a considerable amount of positive charge over time and eventually repels the plasma. As a result, the sputtering rate decreases with time, and finally the process ceases altogether.

The use of radio frequency (RF) sputtering is one of the most effective and reliable methods for addressing the issue of target charging. RF sputtering uses an alternating electric field. Instead of using a fixed voltage, a certain frequency is used to create an alternating field. The positively charged ions are propelled toward the target during the first half of the cycle, while negatively charged electrons are directed toward the substrates. The target begins to accumulate a positive charge during this portion of the cycle. The polarity of the field reverses in the second half of the cycle, and the electrons are now propelled toward the positively charged target. These electrons neutralize the accumulated positive charge, allowing the sputtering process to continue. Because sputtering occurs for only half of the cycle, the sputtering rate is cut in half.

Sputtering by utilizing powerful magnets to confine the electrons in the plasma at or near the surface of the target can boost sputtering yield. The process is called magnetron sputtering. Confining the electrons results in a more substantial density of plasma, which leads to significantly increased deposition rates. The method also facilitates shielding the substrate or film from damage caused by direct electron contact. The magnetron configuration is effective for both RF and DC sputtering.

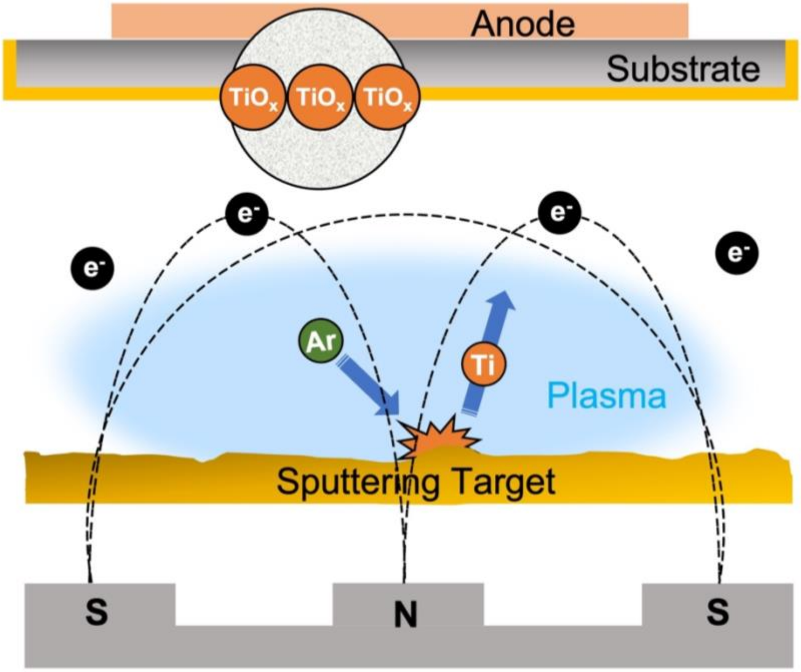

Figure 3.2: Schematic diagram of the magnetron sputtering process. The electrons become trapped and form a dense plasma near the target due to the applied magnetic field.

3.1.1.b: Evaporation

Evaporation is a common thin-film deposition process. Some of the most basic kinds of PVD include thermal and vacuum evaporation. In a vacuum, the source material is evaporated by raising its temperature. The vaporized material is then transported through the vacuum directly to the substrate, where it condenses. Before the process begins, sources of contamination can be reduced by baking out the chamber under vacuum.

3.1.1.c: Ion plating

Ion plating or ion aided deposition (AID) is a vacuum deposition technique. The process of ion plating entails blasting the substrate with high-energy particles. First, atomic-sized particles are used to clean the substrate. At the end of the cleaning phase, energetic particles are bombarded in a concurrent or periodic pattern to obtain good adhesion.[99] To ensure an atomically smooth surface, the irradiation must be continuous between the cleaning and deposition stages of the process.

3.1.1.d: Pulsed laser deposition

Another typical PVD technique is pulsed laser deposition (PLD), in which an intense laser pulse is focused and impinges on a particular target inside a vacuum chamber. The concentrated pulsed laser beam vaporizes the irradiated target material, which is then deposited onto a substrate facing the target. When a laser pulse strikes the target, its energy is initially converted to electrical excitation before being translated into thermal, chemical, and mechanical energy. This results in evaporation, ablation, plasma generation, and even exfoliation.[100]

3.1.2: Chemical vapor deposition (CVD)

Chemical vapor deposition (CVD) is a vacuum deposition technique to produce high-quality coatings and is used extensively in the semiconductor industry. In CVD, the substrate is exposed to thermally induced chemical reactions with reagents supplied in the gaseous phase to form the intended thin film. Vapor phase epitaxy (VPE) and metal-organic chemical vapor deposition (MOCVD) are common types of CVD.

3.1.2.a: Vapor phase epitaxy (VPE)

In VPE, gas molecules are used to deposit atoms on the substrate. VPE is widely used in the semiconductor industry to grow chips on a silicon substrate. In the reaction chamber, reactant gases are pumped, which under the right conditions react and are deposited onto the substrate. As the film expands, subsequent reactions help move the atoms to their respective lattice sites. The by-products desorb and are transported away from the reaction zone by convection and diffusion.

When it comes to semiconductor growth, CVD offers some key advantages. CVD deposition is very fast due to significantly high flow rates of the precursors and can be used to make high-quality and high-performance uniform films. Furthermore, in CVD, variables in the growing process can be precisely regulated.

3.1.2.b: Metal-organic chemical vapor deposition (MOCVD)

Compared to conventional epitaxy processes, metal-organic chemical vapor deposition (MOCVD), also known as metal-organic vapor phase epitaxy (MOVPE), offers a substantially greater throughput. MOCVD is a deposition technique use to make crystalline and polycrystalline thin films for compound semiconductor devices. It is well suited for creating semiconductor multilayer structures.

MOCVD is comparable to VPE in that at least one metal-organic precursor includes both metal and organic components. MOCVD involves passing ultrapure precursors, often in the liquid phase, into a reactor, generally with a non-reactive carrier gas such as hydrogen (H_2) or nitrogen (N_2). The precursors undergo thermal decomposition when they approach the substrate, and the materials get adsorbed onto the substrate surface. During the surface reaction, the materials get incorporated into an epitaxial layer of the crystal lattice. The deposition occurs at pressures comparable to atmospheric pressure. Accumulating reactive species in the gaseous phase drives growth in the MOCVD reactor. MOCVD uses heated gas flow and surface reactions; hence requires higher substrate temperatures during device growth than other conventional epitaxy techniques. Furthermore, samples can be rotated to introduce improved uniformity and film quality.

3.2: Bulk crystal growth

Any solid substance in which the component atoms are organized in a specific pattern is referred to as a crystal. The most basic method of forming a crystal is to cool the melt until it solidifies. The growth usually occurs after an early phase of either amorphous or crystalline nucleation. Introducing a seed crystal can stimulate growth and eliminate the variability of spontaneous crystal growth.

Crystallization, growth, and coarsening are the three steps in the crystal growth process. A tiny nucleus containing the initially growing crystal is formed when atoms collide in precise directions. The unbound atoms or molecules latch to the stable nucleus and spread its crystalline structure outwards. During the growth stage, the crystal can develop rapidly if the structure contains dislocations and other form of defects. Defects in the structure cause the crystal to expand rapidly by functioning as a catalyst. Perfect crystals, on the other hand, would develop relatively slowly.[101] During the coarsening stage, microscopic crystals are replaced by fewer larger crystals.[67]

3.2.1: Czochralski (CZ) method

The Czochralski (CZ) technique is the most widely used method for growing bulk semiconductor crystals. It is also known as "crystal pulling" or "melt pulling." The BCT samples used in this work were grown by the McCloy research group at the Institute for Materials Research (IMR) at Washington State University using the CZ method.

The configuration for CZ growth is relatively basic and scalable. The process starts with the feed material, also known as the charge, being placed in a cylindrically shaped crucible, and melted using resistance or radio frequency (RF) heaters. After the charge has been entirely melted, a millimeter-wide pure seed crystal of the same material with desired orientation is submerged from the top into the melt layer. A melt meniscus is formed around the seed crystal by modulating the furnace heat rate. Once a small portion of the seed has been re-melted, it is extracted gradually under rotation, and the melt solidifies at the seed surface by forming a new crystal component. As the melt temperature drops, the diameter of the drawn crystal grows. The shape of the crystal is generally maintained by precisely regulating the heating power, drawing rate, and speed of rotation of the crystal. A proper mix of crystal and crucible rotation mounted on shafts is employed throughout the process to regulate the radiative heating and material flow inside the melt.

The benefits of the CZ approach include the ease of doping with impurities, a rapid growth rate of high-quality uniform crystals, reduced lattice defects, and the ability to manufacture massive crystals for industrial applications.

A downside of the CZ method is the incorporation of impurities from the crucible, which can limit the carrier mobility. The most common crucible material for silicon synthesis is silica, which degrades into the melt over time. While contamination of the melt by the crucible material is unavoidable, the effect can be mitigated by carefully selecting crucible material and appropriate growth temperatures. Furthermore, the CZ technique can be costly, mainly when growing oxide crystals, which demand a higher growth temperature and, as a result, crucibles made of precious metals such as platinum or iridium.

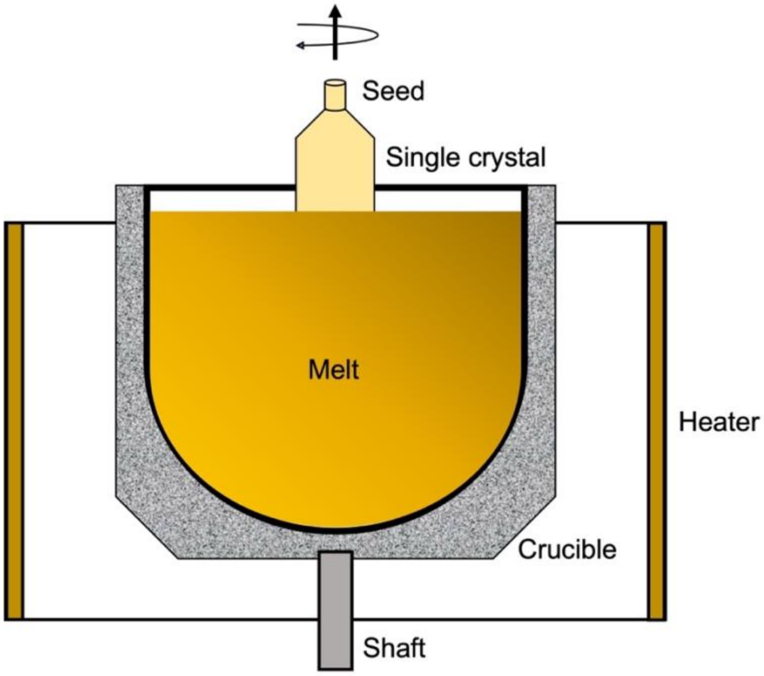

Figure 3.3: Schematic diagram of Czochralski crystal growth.

3.2.2: Verneuil method

The Verneuil method, also known as the flame fusion method, was discovered by the French scientist Auguste Verneuil in 1902. This was the first viable way of creating synthetic gemstones on larger scales. It was used to manufacture ruby, diamond, and strontium titanate. The Verneuil method is still used to grow a variety of materials with relatively high melting points.

The process involves melting a finely powdered charge over an oxy-hydrogen flame at a controlled rate. Combustion occurs with a flame of at least 2000 ℃ at its core. The melt moves through the system as tiny droplets and gradually forms a sinter cone. The seed crystal develops at the tip of the cone, and a boule begins to form. As the crystal grows, the seed is rotated for a uniform growth profile and lowered, resulting in a pure crystal with an even liquid coating.

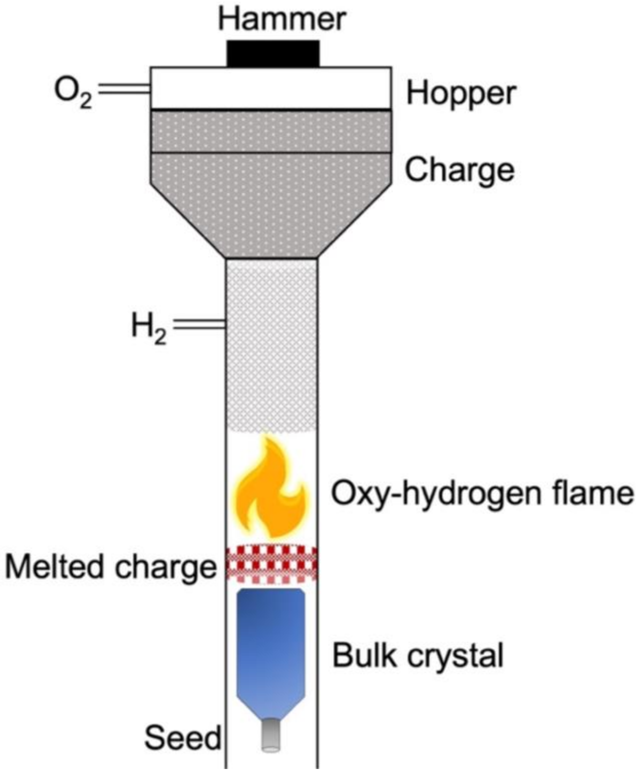

Figure 3.4: Schematic diagram of the Verneuil flame fusion method.

3.2.3: Floating zone method

The floating zone (FZ) method is a crystal-growing technique that does not need the use of a crucible. The main principle is to move a liquid domain across the material to form a single crystal. In the FZ method, the molten zone is confined between two vertical polycrystalline rods. The complete process is carried out in an inert atmosphere. A radio frequency (RF) induction heating coil forms the melt. The melt solidifies on the seed, forming single crystals.

Since no crucible is necessary for this procedure, contamination can be minimized. As a result, highly reactive materials are particularly well-suited to the process. This is certainly relevant for oxygen, which really is unavoidable in the formation of CZ crystals. When reduced oxygen concentrations are required, FZ crystals are always employed. The fundamental disadvantage of the FZ approach is the absolute limit of crystal diameter, which is caused by the surface tension associated with holding it in place.

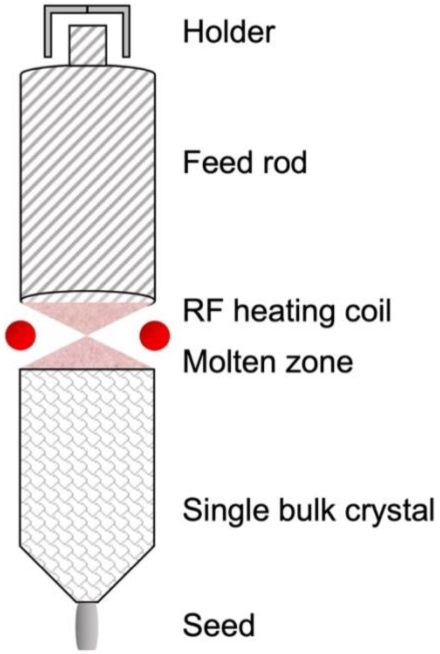

Figure 3.5: Schematic diagram of the floating zone crystal growth method.

3.3: Semiconductor processing

3.3.1: Annealing

Annealing is a thermal treatment that modifies a material's physical and chemical characteristics. Annealing treatments in semiconductor device processing are designed for various effects, including interface modification, dopant activation, repair of implant-related defects, and driving impurities.

3.3.1.a: Sealed ampoule anneal

TiO_2 thin films, as presented in Chapter 4, were annealed under vacuum within a sealed "quartz" ampoule. Before annealing, the sample and quartz ampoule along with the cap, were cleaned with acetone, isopropanol, and high-performance liquid chromatography (HPLC) water wash. The wash removed any dust particles and debris that may interfere with the quality of the seal. The ampoule and quartz cap were placed in a vacuum adapter attached to the sealing station and heat-treated using an oxygen-hydrogen torch while pulling the vacuum with the attached pump to evaporate any remaining cleaning agents. The sample was then placed inside the ampoule, and the cap was fused to the ampoule body to prevent it from sliding during evacuation.

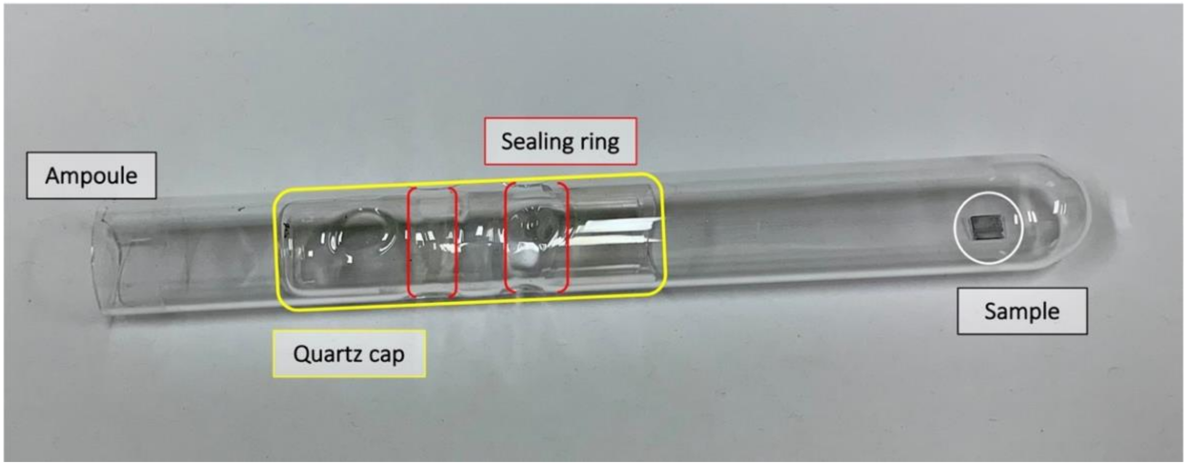

Figure 3.6: Sealed ampoule with TiO_2 thin film under vacuum.

Once the desired pressure of ~16 mTorr was reached, the ampoule was sealed by melting the two pieces of quartz. A moist paper towel was wrapped over the area of the ampoule where the sample was positioned to prevent it from getting warm during the sealing process. The sealed ampoule was annealed for 3 hours in a tube furnace at 800 °C. The temperature ramp rate was set at 650 °C/hour. Prior to extracting the sample from the furnace, it was left to cool overnight. Annealing the thin layer oxide semiconductor under vacuum results in the out-diffusion of oxygen from the crystal, resulting in oxygen vacancies.

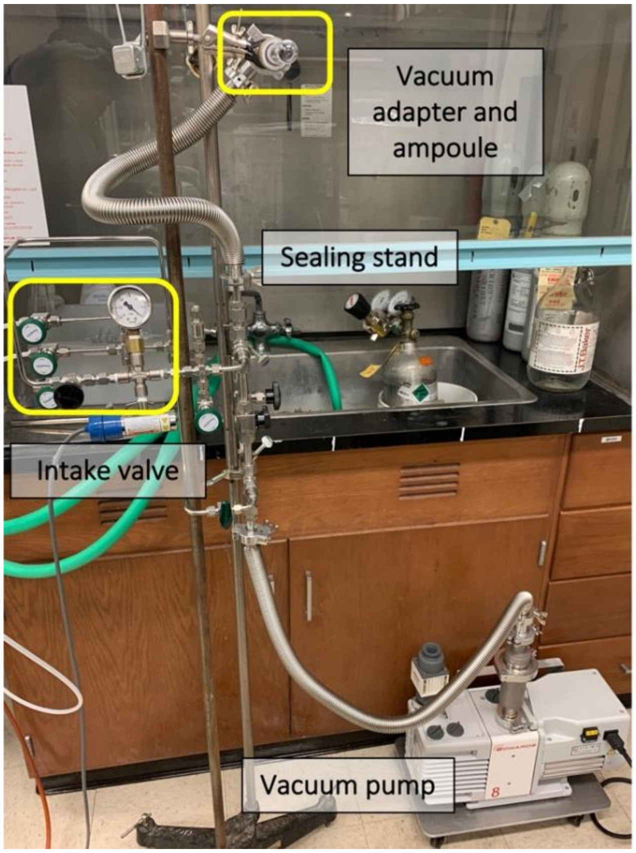

Figure 3.7: Ampoule sealing station.

3.3.1.b: Hot plate anneal

Atmospheric annealing was performed using a Thermo Scientific CIMAREC hot plate. To evaluate the reversibility of the fabricated devices, samples were annealed on the hot plate. After mounting the samples on a glass slide, the hot plate was pre-heated to the desired temperature. Annealing TiO_2 thin films for 15 minutes on a heated plate at 400 °C under normal air pressure reduces the concentration of oxygen vacancies. $Ba_{1-x}Ca_xTiO_3$ was annealed for 30 minutes at 400 °C in the dark to erase the PPC effect.

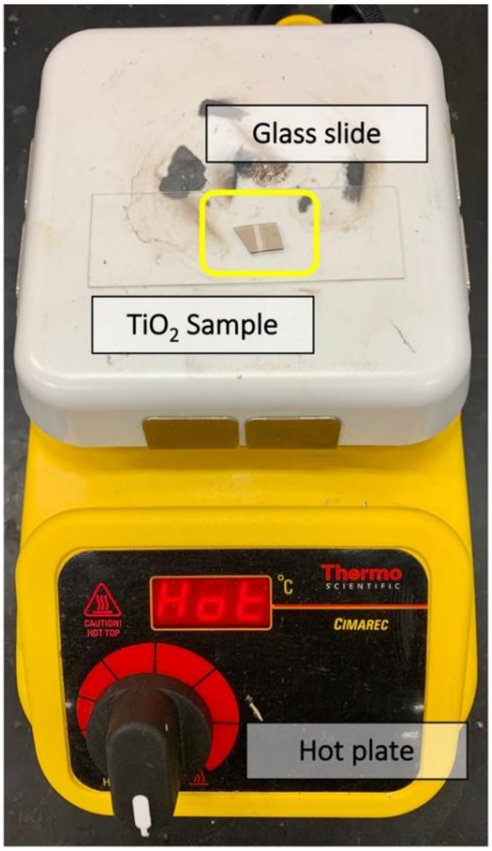

Figure 3.8: Atmospheric annealing of a processed TiO_2 *thin film on a glass slide using a hot plate.*

3.3.1.c: Flowing H_2 anneal

Anneals on barium calcium titanate (BCT) alloys were carried out in a process known as the flowing gas anneal. The hydrogen flow rate was regulated using a mass-flow controller. Argon flow was controlled using a needle valve and measured using a flow meter.

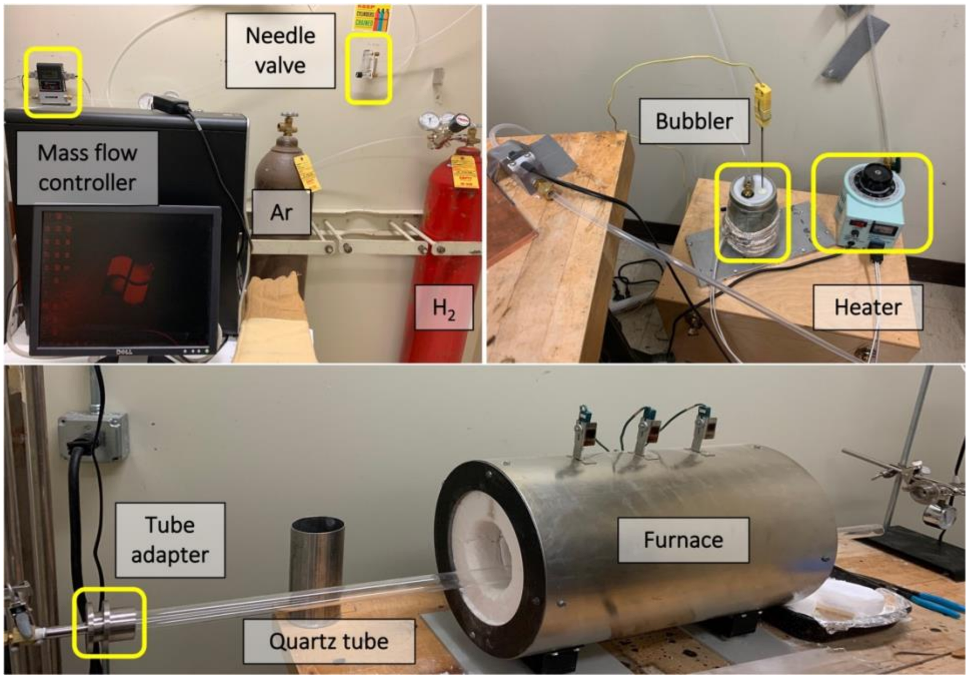

Figure 3.9: Flowing gas anneal setup with horizontal furnace and quartz tube.

A quartz tube fitted with locking adaptors at each end was placed in a horizontal furnace to generate the flowing atmosphere. The sample was positioned at the center of the tube. The sources of gas were a mixture of humid argon and 98% argon + 2% hydrogen gas. The humid argon was produced by blowing ultra-high purity argon through the water. A variable voltage-controlled heater was connected to the bubbler for additional control of the humidity. The escaping gas was released into the atmosphere through a fume hood. The chamber was then purged, and the samples were annealed for an hour at 1200 °C.

3.3.2: Laser irradiation

A Coherent Verdi G5 optically pumped semiconductor laser was used for laser treatment. The laser can generate a diffraction-limited, power-invariant beam with low noise and stability for optimal pumping performance. The 532±2 nm continuous wave (CW) laser has a beam waist diameter of 2.25±10% mm and a maximum power of 5 W. The laser beam was focused to a diffraction-limited diameter of ∼100 μm using a 200 mm focal length coated biconvex lens**.** The sample chamber was mounted on a manual 2D (XY) stage. The laser irradiation was performed in a raster pattern using ~25 μm horizontal step sizes.

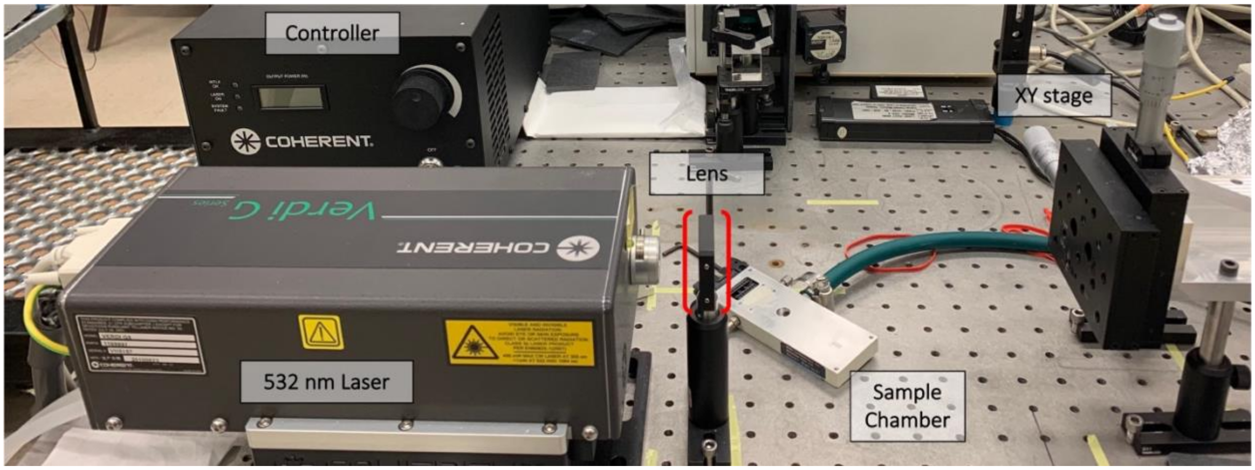

Figure 3.10: Laser processing setup with a Verdi G series laser, 200 mm biconvex lens, and a 2D stage.

CHAPTER FOUR: TITANIUM DIOXIDE

4.1: Publications

The information presented in this chapter has been published in two papers.

- Syeed E. Ahmed, Jesse Huso, Jacob R. Ritter, John Igo, Yi Gu, *and* Matthew D. McCluskey, "*Insulating regions in a TiO_2 thin film defined by laser irradiation*", Journal of Vacuum Science & Technology B 38, 032203 (2020)
- Syeed E. Ahmed, Violet M. Poole, John Igo, Yi Gu, *and* Matthew D. McCluskey, "*Localized phase transition of TiO_2 thin films induced by sub-bandgap laser irradiation*", Journal of Vacuum Science & Technology A 39, 053402 (2021)

The authors gratefully thank Matthew Gabel and Louis Scudiero for performing AFM and XPS measurements, respectively.

4.2: Material growth

Among metal oxide semiconductors, titanium dioxide (TiO_2) is considered a prime candidate for applications due to its diverse electrical and optical properties, nontoxicity, high chemical stability, and ease of mass production. Applications include catalysis, hydrogen production, controlled drug release, and sensing.[40–43] TiO_2 is also used in solar cells and optical coatings due to its high refractive index and are widely used in memory devices and microelectronic capacitors because of its high dielectric constant and resistivity.[45–47] Furthermore, TiO_2 plays a significant role in water purification and antibacterial applications including the decomposition of organic pollutants.[44]

TiO_2 thin films can be deposited using a range of methods. Sputtering, a sol-gel dip-coating method, evaporation, chemical vapor deposition, and metalorganic chemical vapor deposition (MOCVD),[59,102–104,104–108] a popular epitaxial-growth technique with the advantage of large-area deposition, have all been used to fabricate TiO_2 thin films. Among those methods, RF magnetron sputtering can fabricate uniform films with good adherence to the substrate. The technique enables mass-scale large area film deposition, which is suitable for industrial applications. In this work, TiO_2 thin films were deposited onto fused silica substrates via RF magnetron sputtering by LGA Thin Films, Inc.

TiO_2 thin films of 300 nm thickness were deposited onto fused silica substrates by RF magnetron sputtering following an argon (Ar^+) etch with 300 V etching bias for 2 minutes at 1 KW etching power. The sputtered deposition was carried out at room temperature for 6.5 h under a gas mixture of 80% Ar and 20% O_2 and a pressure of 10 mTorr. The TiO_2 target bias voltage was set to 450 V with a deposition rate of 0.8 nm/min.

4.3: Transparent electronics and devices

The field of transparent electronics has grown rapidly and paved the way for developing technologies like transparent displays, smart windows, light-sensitive sensors, and printed transparent electric circuits. Though the possibilities and applications of these transparent electronics are well understood, a proper understanding of a non-invasive fabrication technique and the efficient material candidate is still lacking. This project seeks the advancement of fabricating transparent electronic circuits and phase transformed micro-patterned devices using sub-bandgap laser irradiation. The project also aims to pattern localized conductive/resistive and transformed crystal phase regions using visible laser irradiation on titania (TiO_2) as the active material.

Laser patterning without chemicals and photoresist masking can simplify the traditional fabrication process and is both flexible and cost-effective. Our proposed approach produces a reversible change in electrical resistance and crystal phase, unlike traditional laser processing, which permanently modifies the material.[109] A continuous wave (CW) visible laser simplifies the process and does not ablate the material, unlike a pulsed laser. Photons generate electronic excitations that alter the concentration of oxygen vacancies (V_O) hence conductivity in the treated region. The laser is scanned in a user-defined pattern of insulating regions on an otherwise conductive wafer (Fig. 4.1). Annealing the wafer in a vacuum erases the entire pattern, making the process reversible and the wafer re-usable.

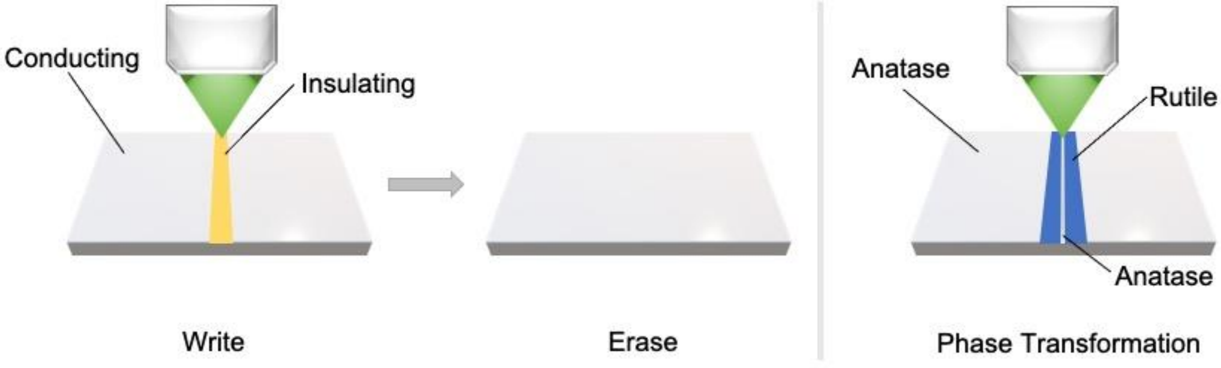

Figure 4.1: Insulating region defined by laser irradiation. Annealing the sample in a vacuum erases the entire pattern. Irradiating the sample under different conditions triggers a phase transformation.

In addition to changing the conductivity, laser irradiation under different processing conditions can also be used to locally transform the material's crystal phase. The selectivity of laser induced phase change has the potential to maximize the reactivity and efficiency of patterned devices. The project focuses on using titania (TiO_2) as the active material. TiO_2 is a transparent conducting oxide (TCO), which is a preferred material for transparent electronics,[10,11] especially with liquid crystal displays due to its optical transparency and electrical conductivity.

4.4: Persistent photo-resistivity

TiO_2 is a wide bandgap semiconductor that has three distinct crystalline phases: rutile, anatase, and brookite. In the case of thin films, anatase and rutile structures are the most common.[110] Anatase is a low-temperature metastable phase that transforms into the more stable rutile phase at high temperatures.[103] Electrons in the anatase phase behave as free electrons rather than small polarons,[30–32] which makes the anatase structure preferable for applications that require conductive materials. In particular, catalysis is enhanced by free electrons.[24–29]

The *n*-type conductivity of anatase depends strongly on the concentration of oxygen vacancies (V_O), which act as shallow donors.[111,112] Heating a nonstoichiometric sample in oxygen lowers the V_O concentration and hence increases the resistivity.[30] V_O defects have been reported to cause optical absorption in the visible range.[113] In this work, green laser light is absorbed by the defect, resulting in electronic excitation. This excitation, perhaps accompanied by localized heating, leads to a dramatic increase in resistance. Unlike typical photoconductivity, which results from photoexcited carriers, in the present case, light appears to cause a photochemical reaction that permanently reduces the oxygen vacancy concentration. Localized laser irradiation was performed to optically define insulating regions. A reversibility experiment demonstrated the potential to write, and rewrite localized electronic circuits on TiO_2 thin films using a laser. The laser irradiation technique does not damage the film nor appreciably change the surface morphology and composition.

4.4.1: Defining localized insulating regions

The experimental approach for optically writing insulating regions on thin-film TiO_2 is outlined in this section. Continuous-wave irradiation was performed using an optically pumped semiconductor laser (Coherent Verdi G series) with a wavelength of 532 nm and a beam diameter of 2.25 mm. A biconvex lens with a focal length of 200 mm was used to focus the laser beam to a diffraction-limited diameter of ∼100 μm. The sample was mounted and scanned in a raster pattern using a manual 2D (XY) stage to define resistive regions.

Two-probe resistance measurements were carried out using a Keithley 6487 picoammeter with pressed indium contacts, copper wire, and silver paint. Surface structure, morphology, and composition of the film were investigated using a scanning electron microscope (SEM) with an in-lens detector and energy-dispersive x-ray spectroscopy (EDS). Atomic force microscopy (AFM) measurements were performed with a Bruker Multimode 8 AFM. Scans were performed in contact mode maintaining the same force constant between the tip and sample. Optical transmission spectra of TiO_2 thin films were measured at room temperature by a UV-Vis-NIR spectrometer (PerkinElmer Lambda 900) in the wavelength range between 300 and 800 nm. X-ray photoelectron spectroscopy (XPS) measurements were performed on an AXIS-165 with an Ultra spectrometer from Kratos Analytical, Inc. The X-ray source was a monochromatized Alka source (1486.6 eV). The spectrometer was calibrated against Au 4f 7/2 at 84 eV and Ag 3d 5/2 at 368.3 eV.

To investigate the phase transformation of a laser treated TiO_2 thin film, a Raman microscope (Renishaw inVia) was used to collect Raman spectra in backscattering geometry. A He–Ne laser was used as a monochromatic excitation source with a 632 nm excitation wavelength at a magnification of 100Å~ under ambient conditions. The Raman spectrometer was adjusted carefully to ensure regions of the samples undergo similar testing conditions with a spectral resolution of about 1 μm. For signal processing, a Savitzky–Golay filter was used to smooth the spectra, followed by subtraction of the splined background.

TiO_2 thin films were vacuum annealed at 32 mTorr pressure and 800 °C for 3 h. Vacuum annealing increases the concentration of oxygen vacancies in the film, resulting in higher conductivity, as shown by Cronemeyer[114] for rutile TiO_2. To optically define insulating regions, we performed localized irradiation using the 532 nm laser operating at 1.5W power. Laser irradiation in the air apparently decreases the concentration of oxygen vacancies, resulting in a substantial increase in resistance. Laser treatment also increases optical transparency, consistent with a reduction in the oxygen vacancy concentration.

Figures 4.2(a) and 4.2(b) show the laser-treated stripe with a width of approximately 1.5 mm, along with pressed indium contacts, silver paint, and copper wires. The insulating stripe is composed of approximately 60 laser lines drawn consecutively 25 µm apart. Figure 4.2(a) also shows thin insulating stripes made by variable laser output power. The sample once again went through vacuum annealing after laser treatment to investigate the reversibility of the process. Figure 4.2(b) shows that the laser-treated stripe is mostly erased after vacuum annealing.

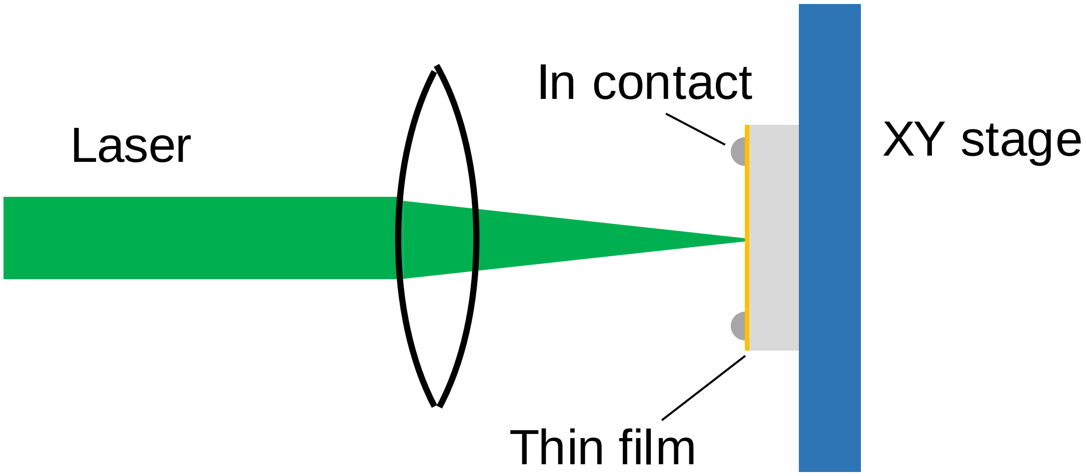

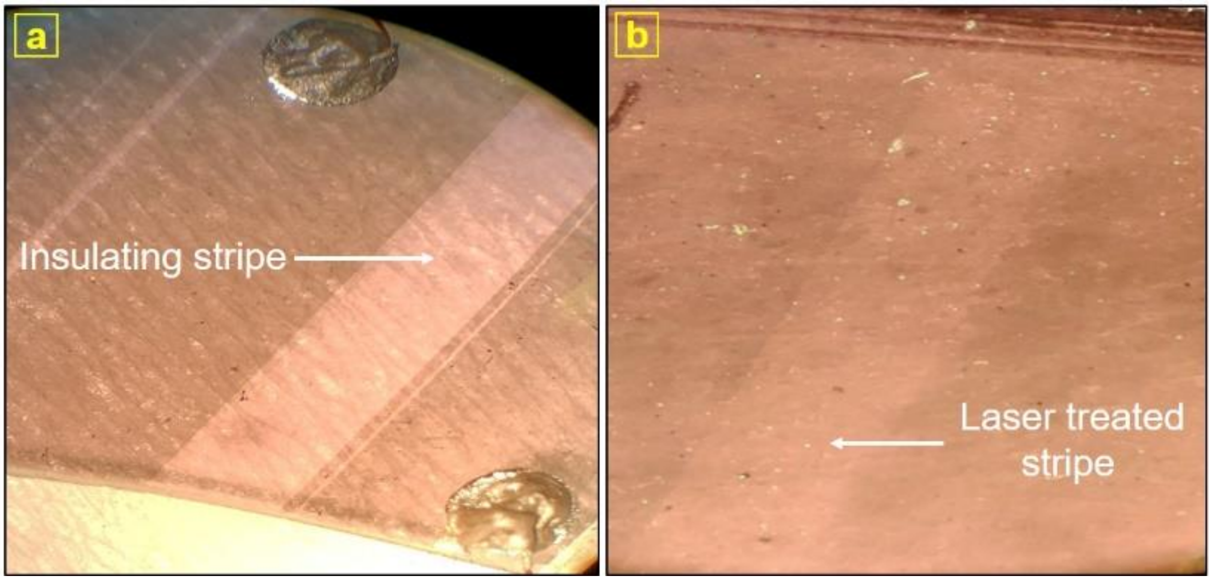

Figure 4.2: Top: Schematic diagram of the experiment. (a) Photograph of TiO_2 thin film on SiO_2 substrate with pressed indium contacts and laser-treated insulating stripe (1.5 mm width). (b) Photograph of the laser-treated sample after vacuum annealing.

4.4.2: Results and discussion

4.4.2.a: Electrical measurements

Oxygen vacancies in TiO_2 thin films act as shallow donors[111,112] and are likely responsible for *n*-type conductivity. As shown in Fig. 4.3, the resistance of our vacuum-annealed thin film is ∼170 kΩ. A current-voltage measurement taken across the laser-treated stripe, in contrast, showed nonlinear behavior with resistance on the order of 109 kΩ. (A measurement taken with contacts on the stripe showed a similar result.) This extremely high resistance was at the edge of detectability; large applied voltages were required to obtain measurable currents.

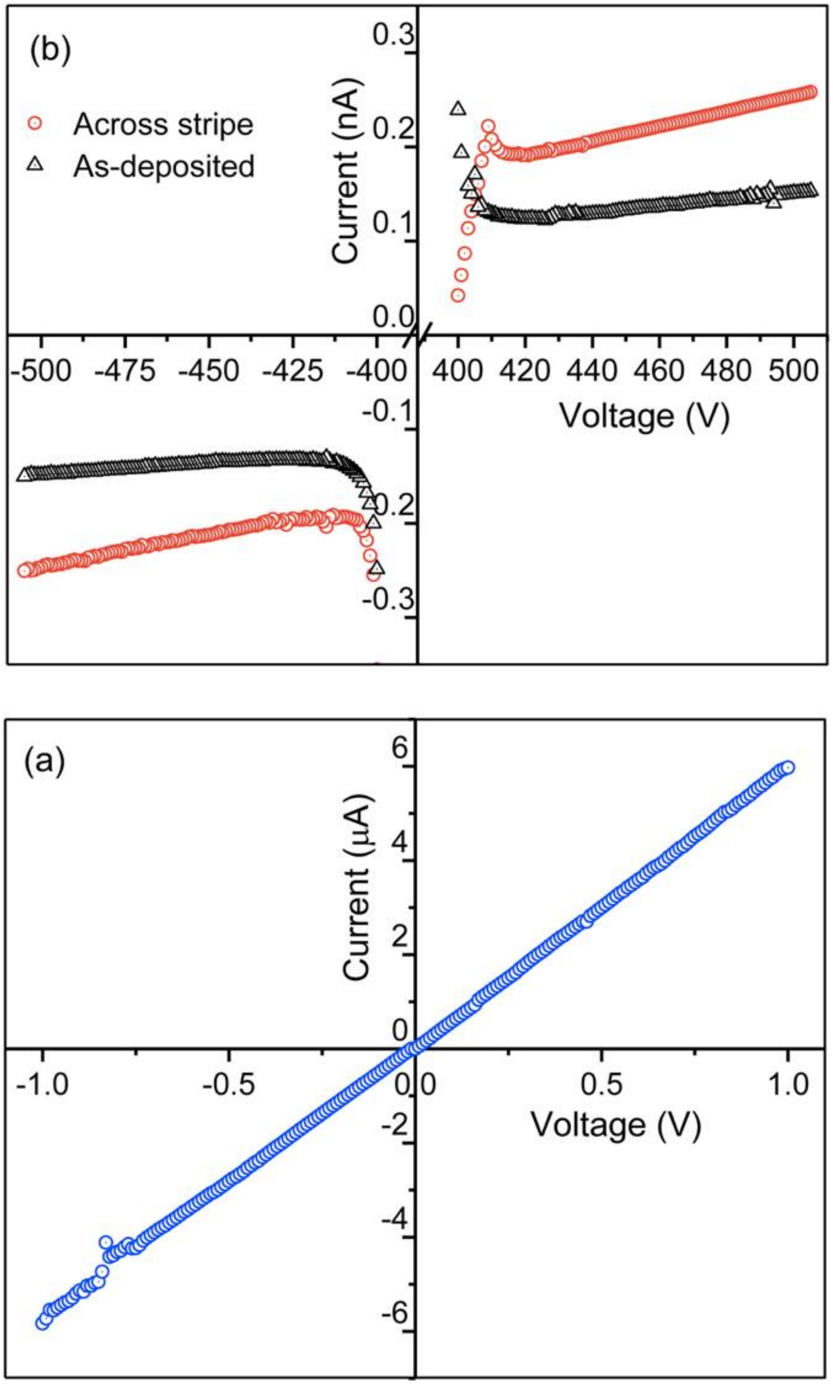

Figure 4.3: I–V characteristics of TiO_2 thin films for the (a) vacuum-annealed region and (b) laser-treated stripe and as-deposited sample.

The resistance was measured across the laser-irradiated band in the dark, under fluorescent light, and with a UV lamp. Figure 4.4 depicts the change in conductivity as a function of illumination time under various lighting conditions, indicating that conductivity increases during UV illumination.

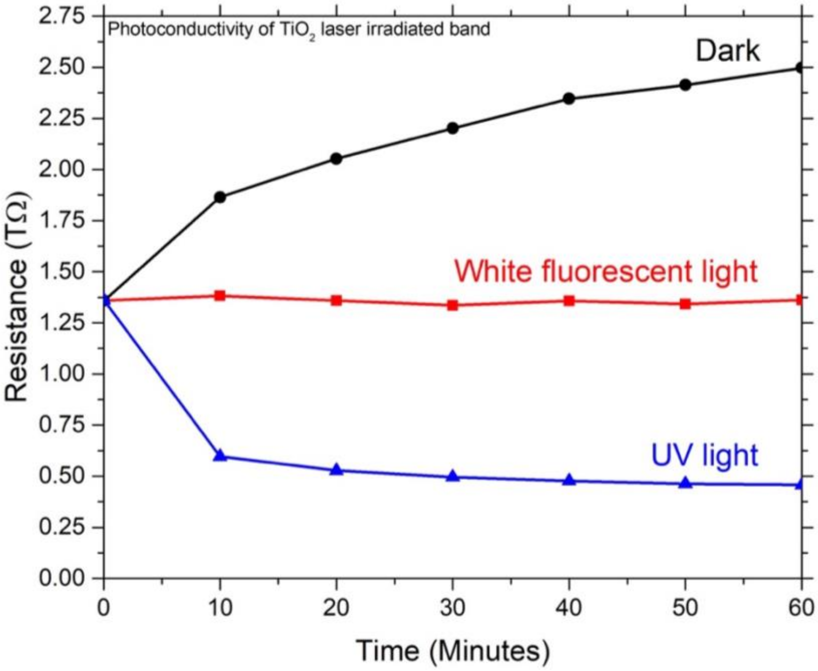

Figure 4.4: Resistance across laser irradiated TiO_2 band under different lighting conditions.

To further understand the change in conductivity induced by illumination in the laser-irradiated band, we used a Horiba Fluorolog as an excitation source. The excitation range of the Xenon lamp utilized in the apparatus is 240 - 600 nm. Figure 4.5 illustrates the change in resistance across the laser irradiated band due to absorption in the visible and UV ranges. The highest conductivity occurs in the UV region around 340 nm, which can be attributed to bandgap absorption.

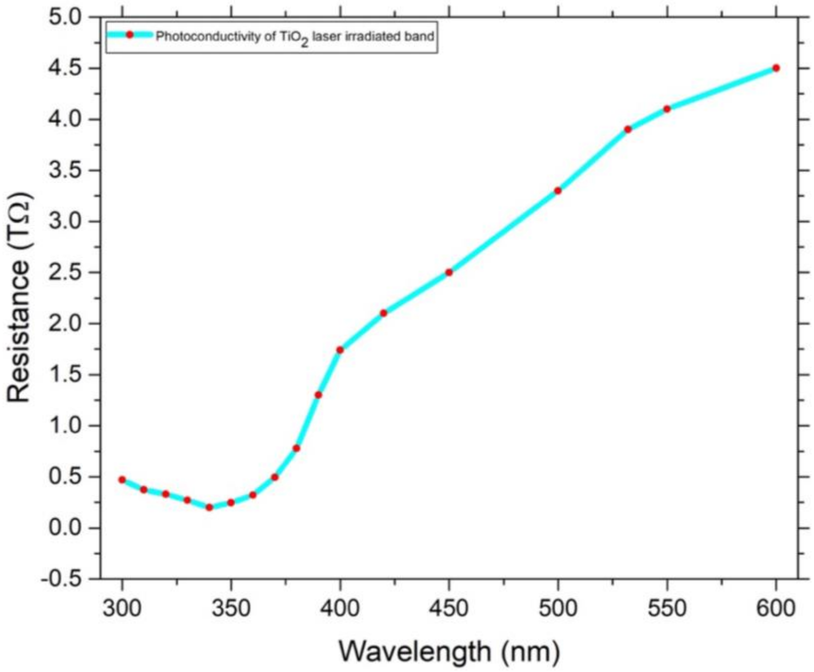

Figure 4.5: Change in resistance of a laser irradiated TiO_2 band using a Xenon lamp as excitation source.

4.4.2.b: Scanning electron microscopy (SEM)

The TiO_2 thin films were analyzed by SEM and EDS in order to study the surface structure and chemical composition. Figure 6 displays SEM images of a vacuum-annealed, laser-treated TiO_2 thin film. As shown in Fig. 4.6(a), there is significant contrast between the laser-treated stripe and the surrounding region. This change in contrast is due to the highly insulating stripe charging and deflecting the scanning electron beam. Figures 4.6(b) and 4.6(c) are high-magnification images of the regions inside and outside the laser-treated stripe, respectively. They indicate no obvious changes in the surface morphology or grain size due to laser irradiation.

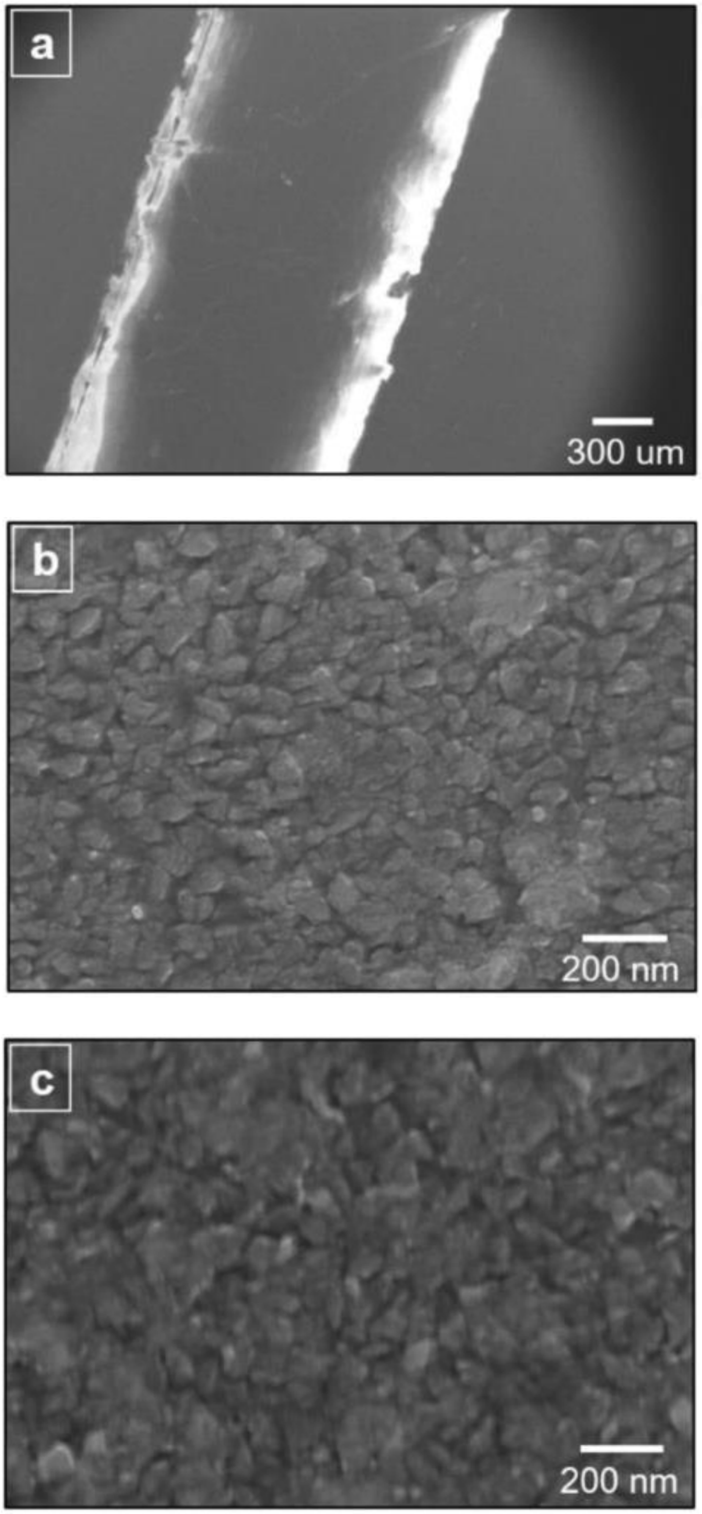

Figure 4.6: SEM micrographs of vacuum annealed TiO_2 *thin film on the* SiO_2 *substrate. (a) Laser-treated stripe. (b) High-magnification image of a region inside the laser-treated stripe. (c) High-magnification image of a region outside the stripe.*

4.4.2.c: Atomic force microscopy (AFM)

As seen in Figure 4.7 atomic force microscopy (AFM) images indicate that the root mean squared roughness for the vacuum-annealed and laser-treated regions are nearly the same; 3.4 and 3.5 nm, respectively.

(a)

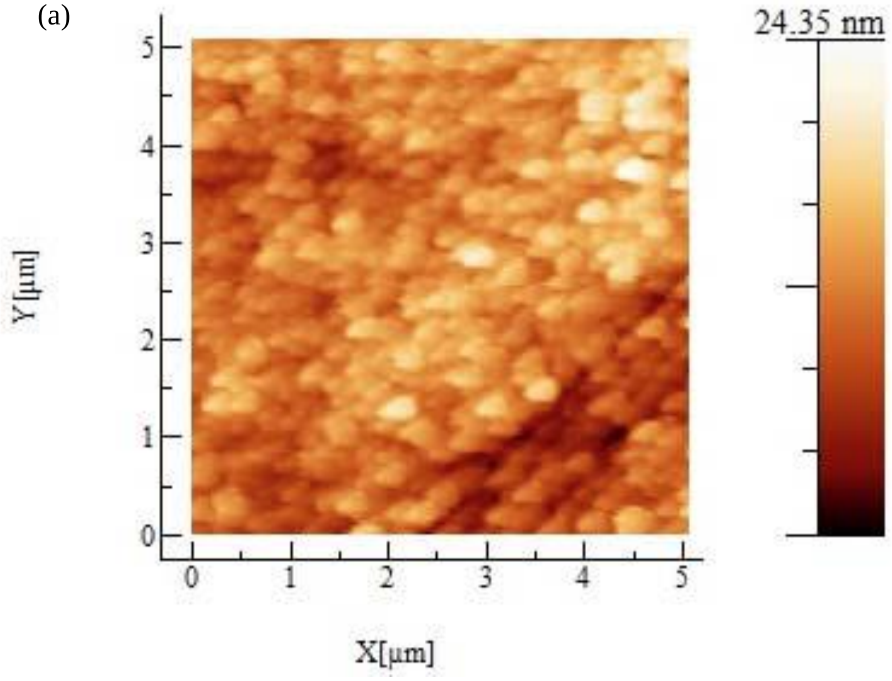

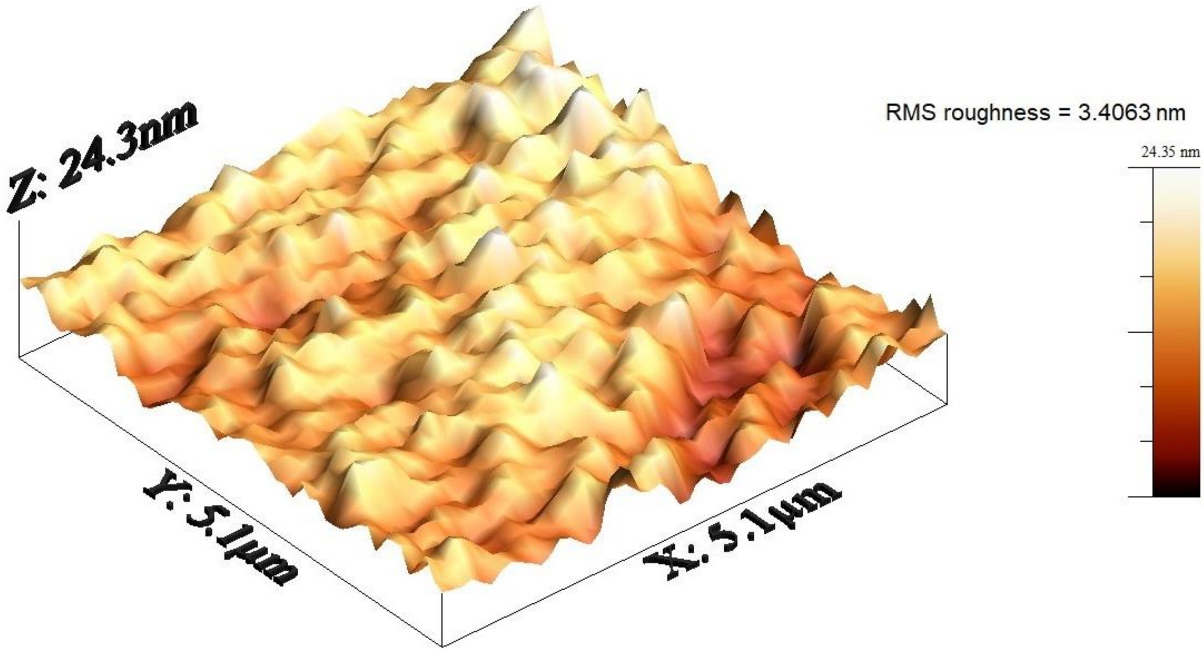
Z: 24.3nm
Y: 5.1μm
X: 5.1μm
RMS roughness = 3.4063 nm
24.35 nm

(b)

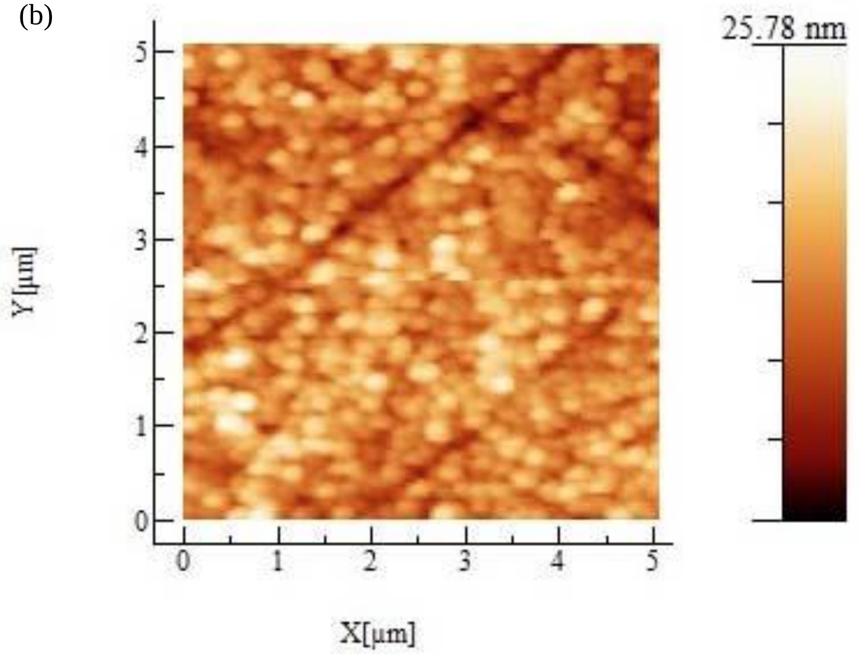
25.78 nm
Y[μm]
X[μm]
0
1
2
3
4
5

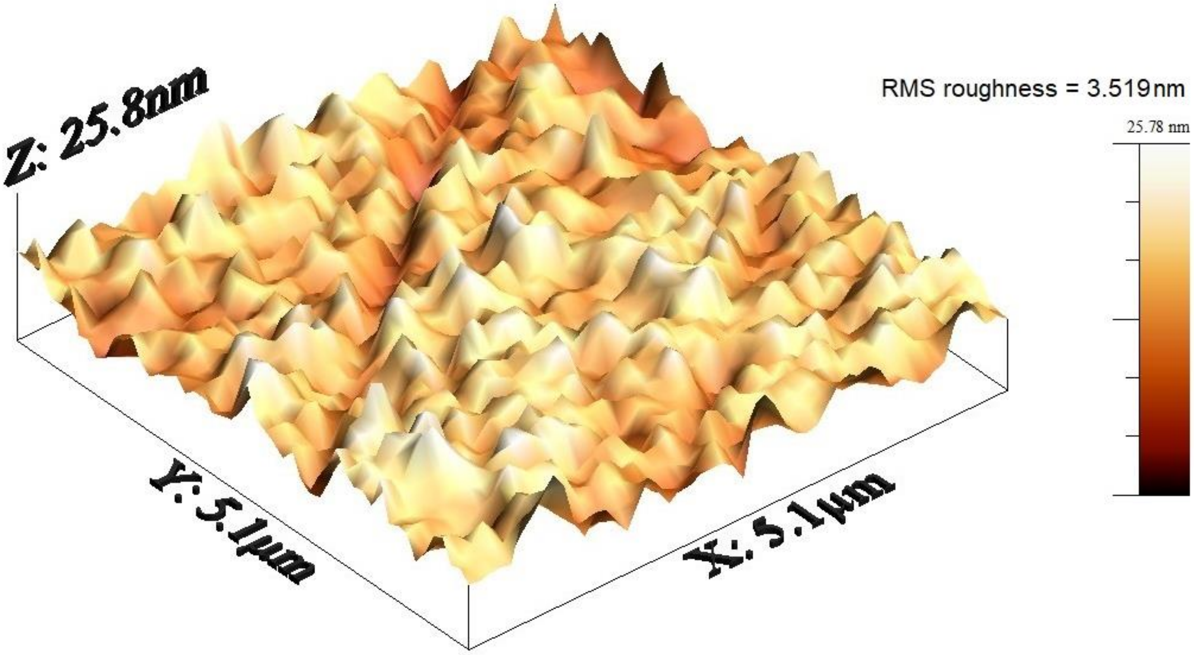

Figure 4.7: AFM images of vacuum-annealed TiO_2. (a) Region outside the laser-treated stripe. (b) Region inside the stripe.

4.4.2.d: Energy dispersive spectroscopy (EDS)

The EDS spectrum of the laser-treated TiO_2 thin film shows a significant amount of Si, Ti, and O (Fig. 4.8), as expected, where the Si and O signals come from the substrate. The spectrum also indicates the presence of C with very low intensity. EDS element mapping of the sample demonstrates that there are no substantial changes in the composition due to localized laser heating and confirms that the composition of the film is intact after the treatment. As seen in Fig. 4.8, the composition of Si, Ti, and O are uniform across the laser-treated and vacuum-annealed interface.

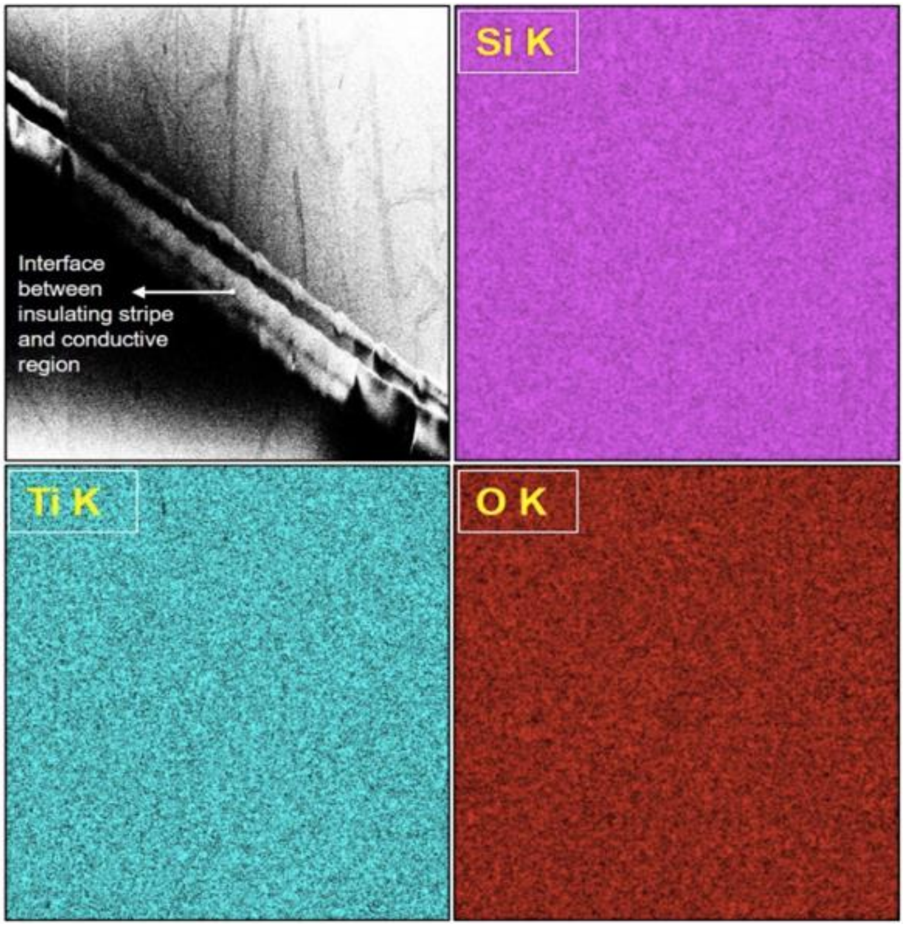
Interface between insulating stripe and conductive region
Si K
Ti K
O K

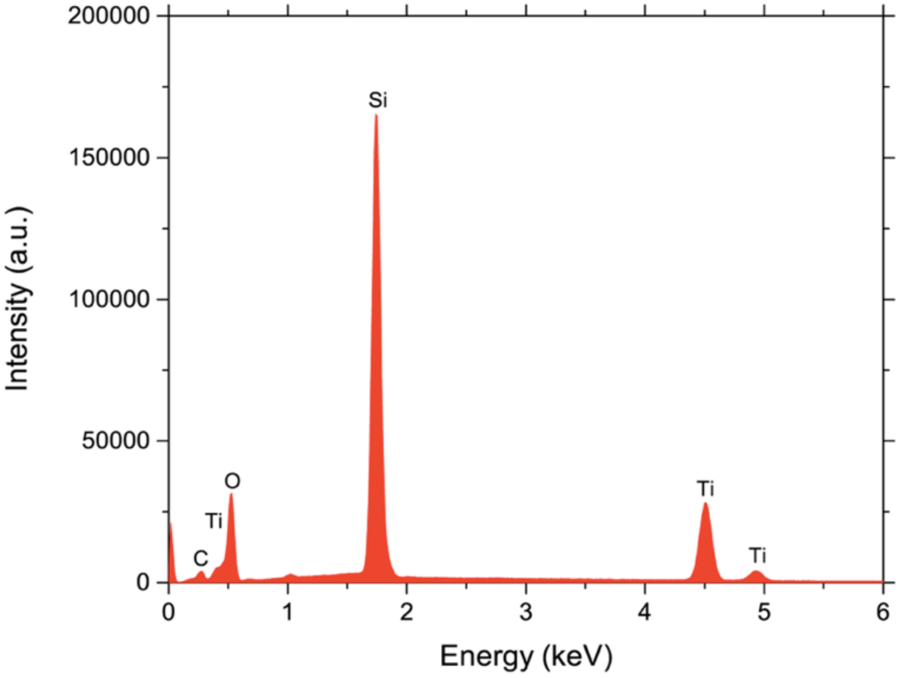
Intensity (a.u.)
200000
150000
100000
50000
0
Energy (keV)
0
1
2
3
4
5
6
C
Ti
O
Si
Ti
Ti

Figure 4.8: Top: SEM micrograph and EDS mapping, Bottom: EDS spectrum of TiO_2 thin film on the SiO_2 substrate.

4.4.2.e: X-ray photoelectron spectroscopy (XPS)

The results of x-ray photoelectron spectroscopy (XPS) as shown in Fig. 4.9 suggest that the vacuum annealed surface contains more surface hydroxyl (OH) molecules. It is possible that these molecules are driven off by laser treatment. The Ti/O ratio does not change significantly, consistent with the EDS results.

(a)

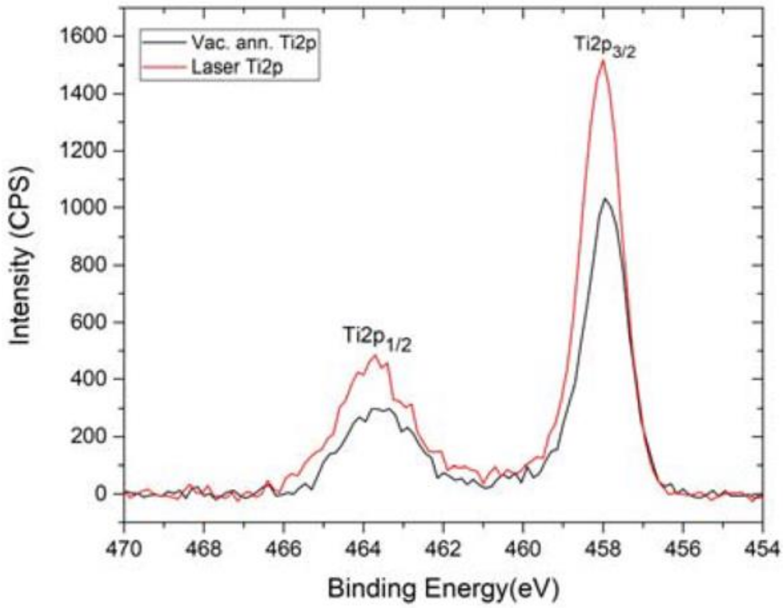

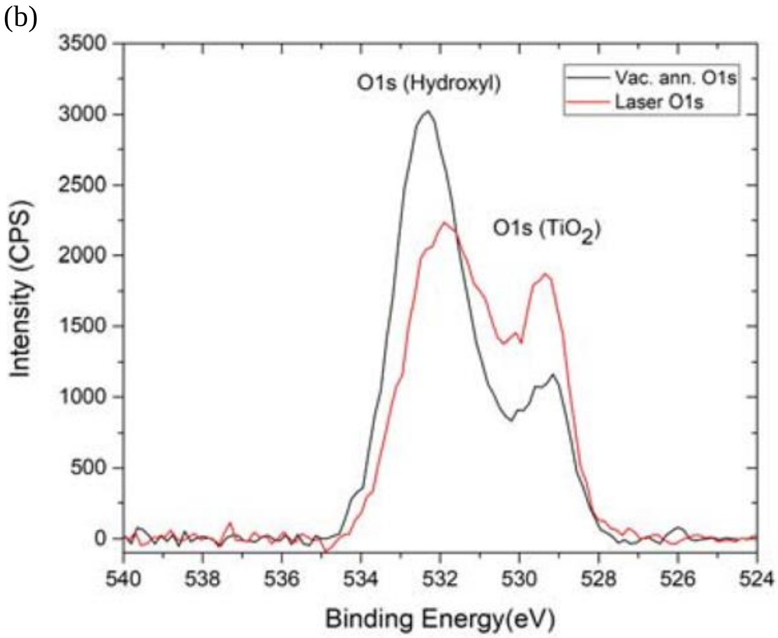

Figure 4.9: XPS spectra of (a) vacuum-annealed and (b) laser-treated TiO_2 thin film.

4.4.2.f: UV-Vis spectroscopy

Transmission spectra were collected to analyze the optical bandgap and refractive index of the vacuum-annealed, laser-treated TiO_2 thin film. Figure 4.10(a) shows optical transmission spectra of as-deposited, vacuum-annealed, and laser-treated TiO_2. The as-deposited film was highly transparent in the visible region with a transparency of > 85%. There is a drop in transmittance to < 60% for the vacuum-annealed region, which is consistent with the formation of oxygen vacancies.[113] For the laser-heated region, the transmittance is restored to 70%, attributed to a decrease in oxygen vacancies. The sharp decrease in transmittance below 400 nm is due to bandgap absorption.

The bandgap absorption threshold is shown in a Tauc plot [Fig. 4.10(b)]. By extrapolating the slopes to zero, bandgaps of ~3.7 eV are obtained, with no significant changes due to laser treatment. This bandgap value concurs with prior experimental[115] and theoretical[116] estimates in the 3.6 – 4.0 eV range.

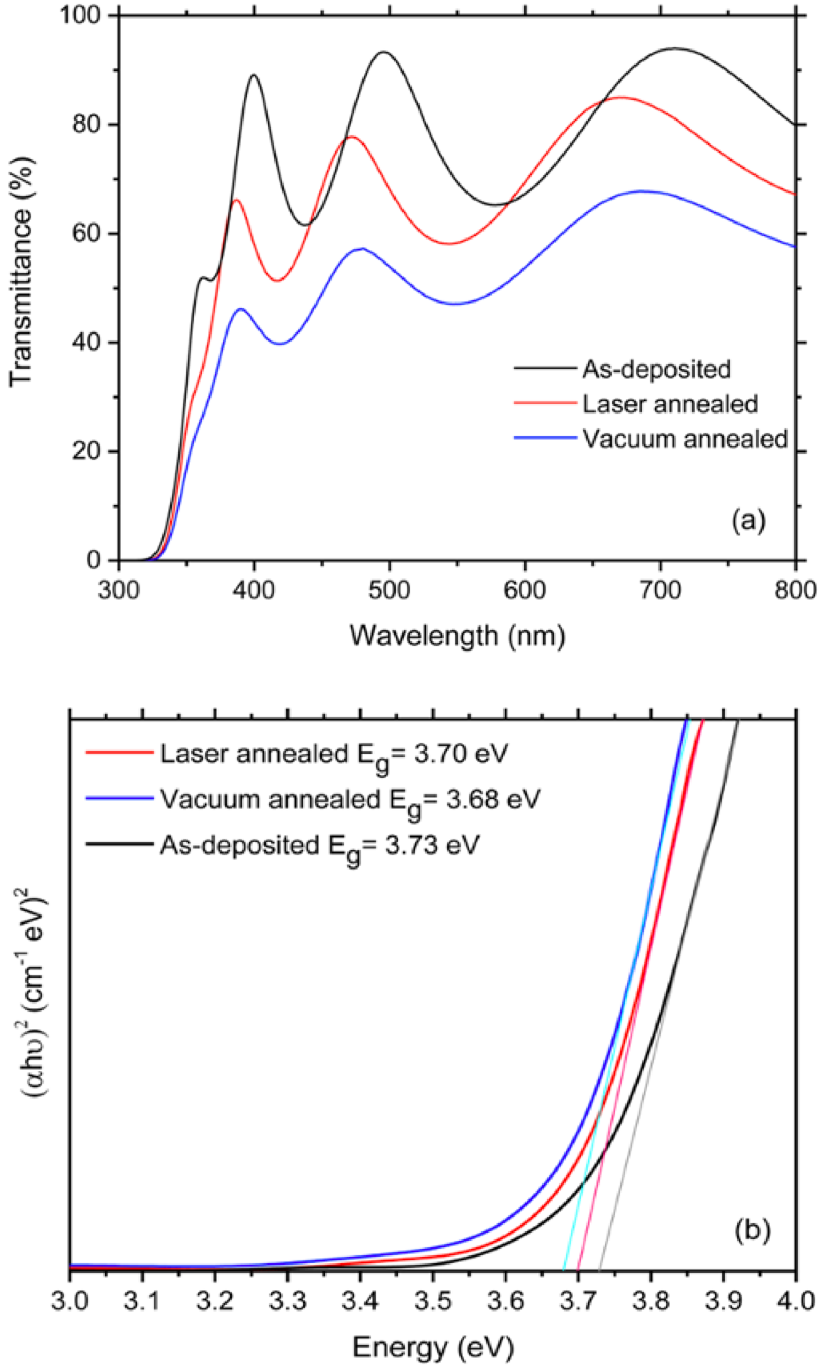

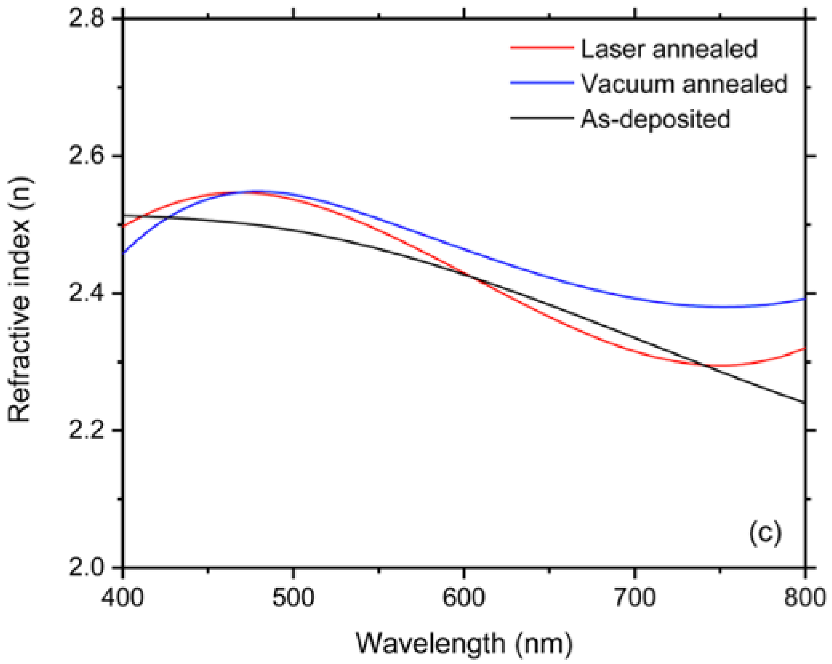

Figure 4.10: (a) Optical transmission spectra, (b) optical bandgap, and (c) refractive index of as-deposited, vacuum-annealed, and laser-treated TiO_2 thin films on the SiO_2 substrate.

Figure 4.10(c) shows the refractive index as a function of wavelength. The Swanepoel method[117] was used to calculate the refractive index from the transmittance spectra of the films, which shows interference effects. Envelope curves were formed using a local maximum method combined with a cubic spline interpolation of the experimentally collected transmission dataset. Given the known refractive index of the SiO_2 substrate, the refractive index was calculated from the envelope functions.[117] The refractive index can be calculated using the equation:

$$n(\lambda) = \sqrt{\left(\frac{2n_s\left(T_{max}(\lambda) - T_{min}(\lambda)\right)}{T_{max}(\lambda)\,T_{min}(\lambda)} + \frac{n_s^2+1}{2}\right) + \sqrt{\left(\frac{2n_s\left(T_{max}(\lambda) - T_{min}(\lambda)\right)}{T_{max}(\lambda)\,T_{min}(\lambda)} + \frac{n_s^2+1}{2}\right)^2 - n_s^2}} \qquad (4.1)$$

Here n_s is the refractive index of the SiO_2 substrate

$$n_s = \frac{1}{T_s} + \sqrt{\frac{1}{T_s^2} - 1} \tag{4.2}$$

For $T_s = 0.91$, our $n_s = 1.554$. $T_{max}(\lambda)$ and $T_{min}(\lambda)$ are the normalized maximum and minimum transmittances at the same wavelength on the envelope curves of the sample. As shown in Fig. 10(c), the refractive index is similar for all three samples and is comparable to that measured in other sputtered TiO_2 films.[118] The TiO_2 thin film thickness was calculated by

$$d = \frac{A\lambda_1\lambda_2}{2[n(\lambda_1)\lambda_2 - n(\lambda_2)\lambda_1]} \tag{4.3}$$

where A = 1 for two matching adjacent extremes and A = 0.5 for two unmatched adjacent extremes. λ_1 and λ_2 are the corresponding wavelengths for the adjacent extremes. For the as-deposited film, we found $d_{as\text{-}deposited} = 297 \pm 5$ nm, which is close to our chosen deposition parameter. For the vacuum-annealed and laser-treated region, we obtained $d_{vacuum\ annealed} = 296 \pm$ nm and $d_{laser\ treated} = 293 \pm 5$ nm, which suggests that the laser treatment did not degrade the films.

4.4.2.g: Raman spectroscopy

Raman spectroscopy was used to study the change in the vibrational structure due to vacuum annealing and localized laser irradiation. Anatase has a tetragonal symmetry with space group D_{4h}^{19}. There are six active Raman modes in anatase: $A_{1g} + 2B_{1g} + 3E_g$,[119] the three E_g modes with frequencies of 144, 197, and 640 cm^{-1}. The strongest mode at 144 cm^{-1} is the characteristic peak of anatase TiO_2 due to its correspondence with symmetric lattice angular vibration.

Figure 4.11(a) shows Raman spectra of TiO_2 as-grown, vacuum annealed, and laser-treated thin films. Four Raman-active vibrational modes at 143, 394, 517, and 635 cm^{-1} confirm the tetragonal anatase phase for the as-deposited sample. Both the laser-treated and vacuum annealed regions show the same characteristic peak but slightly shifted to 146 cm^{-1}. The Raman spectra suggest that there was no phase transition due to localized laser irradiation.

As seen in Fig. 4.11(b), vacuum annealing causes the E_g (1) mode to blueshift from 143 to 146 cm^{-1}. The shift may be due to residual strain from the thermal expansion mismatch between the film and the substrate. The peak remains unchanged during laser treatment, which further indicates no significant change in internal stress and grain size.[120,121] Fitting the peak to a pseudo-Voigt function indicated that vacuum annealing causes the linewidth (FWHM) to increase from 15.8 ± 0.3 to 16.5 ± 0.1 cm^{-1}. Laser treatment decreases the width to 14.7 ± 0.1 cm^{-1}. The slight broadening that occurs in the vacuum-annealed sample is consistent with disorder due to oxygen vacancies.

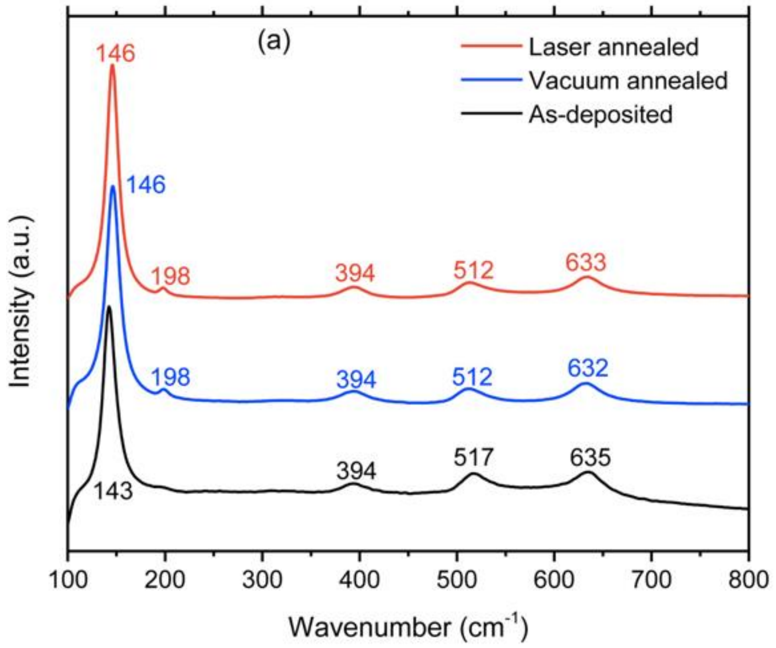

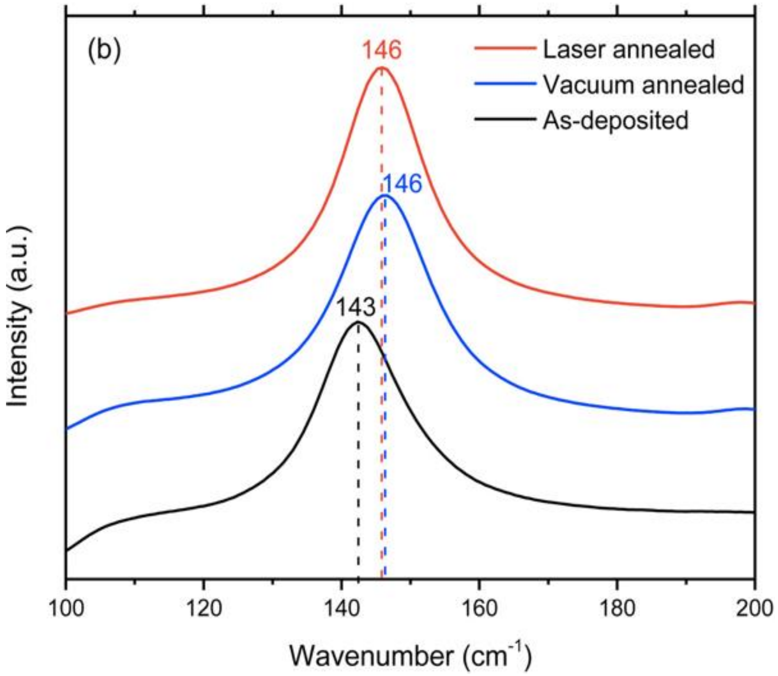

Figure 4.11: (a) Raman spectra of as-deposited, vacuum-annealed, and laser-treated TiO_2 *thin films. (b) Comparison of the anatase* E_g *(1) Raman mode of as-deposited, vacuum-annealed, and laser-treated* TiO_2 *thin films.*

4.5: Localized phase transition

TiO_2 demonstrates a variety of chemical and physical properties based on its crystal structure.[23] Networks of distorted TiO_6 octahedral units are used to construct the crystal structures.[122] The octahedral structures of the anatase and rutile crystals have a distorted four corners and four edges sharing center and a non-distorted two corners six edges sharing center, respectively.[123] Rutile has a symmetry of tetragonal $P4_2/mnm$, whereas anatase has a symmetry of tetragonal $I4_1/amd$. Anatase has improved catalytic properties.[24–32] Rutile, on the other hand, is more thermodynamically stable.[103]

The oxygen vacancy (V_O) has a low formation energy[111,112] and is known to be responsible for anatase's *n*-type conductivity, which is linked to optical absorption in the visible range.[113] Although the thermal donor level (0/+) is near the conduction-band minimum, calculations show that the optical transition threshold is ~1 eV, which may account for the observed absorption.[111] A 532 nm green sub-bandgap laser was used in this study to irradiate TiO_2 thin films under vacuum and ambient conditions. Laser photons are absorbed by defects, which are assumed to be V_O, causing electronic excitation of the treated region. A phase transition occurs as a result of this electronic excitation. Crystal strain and surface defects such as oxygen vacancies and Ti interstitials influence TiO_2 phase transformations.[111,123,124] Laser irradiation under various ambient conditions resulted in different phase transitions in the current study. The ability to define micrometer-sized anatase and rutile phase regions may result in improved photocatalytic properties[125,126] and solar conversion efficiency.[127]

4.5.1: Defining phase transformed paths

Anatase TiO_2 thin films of 300 nm thickness were deposited onto fused silica substrates by RF magnetron sputtering following an argon (Ar^+) etch with 300 V etching bias. A gas mixture of 80% Ar and 20% O_2 and a pressure of 10 mTorr were used to carry out the sputter deposition at room temperature for 6.5 h. The TiO_2 target bias voltage was set to 450 V with a 0.8 nm/min deposition rate.

Laser irradiation was performed with a continuous wave (CW) optically pumped semiconductor laser (Coherent Verdi G series) with a 532 nm wavelength and a beam diameter of 2.25 mm. The laser beam was focused to a diffraction-limited diameter of ∼100 μm using a 200 mm focal length biconvex lens. The sample was mounted inside a chamber fitted with a quartz glass window and scanned in a raster pattern using a manual 2D (XY) stage to define regions of transitioned phases. Laser irradiation in vacuum was performed under dynamic vacuum conditions with a residual pressure of ~2.2×10^{-5} mbar at room temperature. Laser irradiation in the air was then performed to define phase-transformed stripes on regions previously irradiated in vacuum. 1.8 W laser power in vacuum was necessary to trigger the anatase-to-rutile phase transition, while 3.5 W in air was required to cause rutile-to-anatase transition.

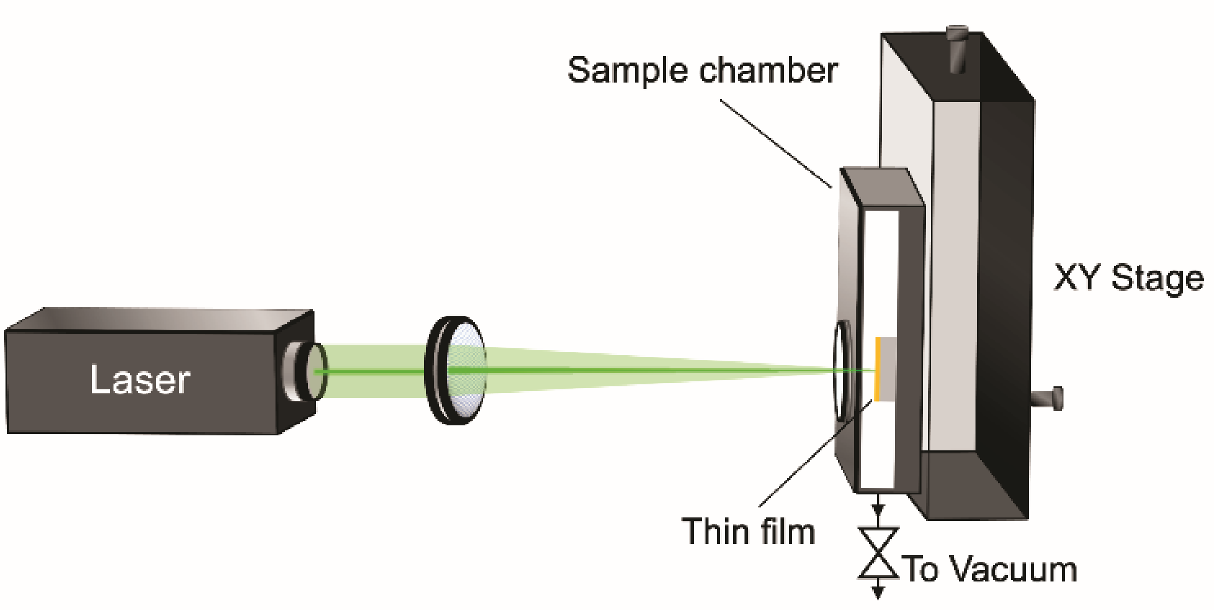

Figure 4.12: Schematic diagram of the experimental setup.

To investigate the phase transformation of the laser treated TiO_2 thin film, a Raman microscope (Renishaw inVia) was used to collect Raman spectra in a backscattering geometry. A He–Ne laser was used as the excitation source with 632 nm excitation wavelength at a magnification of 100×. The Raman spectrometer was adjusted carefully to ensure regions of the samples undergo similar testing conditions with a spatial resolution of about 1 μm. For signal processing, a Savitzky–Golay filter was used to smooth the spectra, followed by subtraction of the splined background.

To study the spatial distribution of phases within the laser-irradiated TiO_2 thin film, Raman measurements were performed using a Klar Mini Pro microscope. The microscope was equipped with a fiber-coupled 532 nm CW laser and Ocean Insight QE Pro spectrometer. A total of 15,876 individual spectra were scanned for each 100×100 μm^2 area of the sample with a spatial resolution of 0.8 μm. The sample thickness of 300 nm was less than the depth resolution of either microscope. The laser power at the sample was 9 mW. Despite the relatively high laser power density, the microscope laser did not cause phase transitions. The acquisition time was set to 5 s per point for the region laser irradiated in vacuum and 8 s per point for the region treated in air. The detected spectral region was 100 to 4000 cm^{-1}. Each spectrum was fit with 8 Lorentzian peaks (144, 197, 236, 395, 436, 515, 608, and 636 cm^{-1}), known to be the typical Raman peaks of TiO_2 anatase and rutile phases.

Anatase and rutile both have a tetragonal symmetry with six active Raman modes in anatase: A_{1g}+ $2B_{1g}$ + $3E_g$. The A_{1g}, B_{1g}, and E_g Raman modes are related to asymmetric bending, symmetric bending, and symmetric stretching vibrations of O–Ti–O bonds, respectively.[128] The three E_g modes have frequencies 144, 197, and 640 cm^{-1}. The strongest mode at 144 cm^{-1} that corresponds to the symmetric lattice angular vibration is a characteristic peak of anatase TiO_2. Rutile exhibits four active Raman modes: A_{1g}+B_{1g}+B_{2g}+E_g with frequencies 143, 235, 445, and 608 cm^{-1}.[61] Modes E_g (445 cm^{-1}) and A_{1g} (608 cm^{-1}) are characteristic peaks of rutile TiO_2.[126]

4.5.2: Results

As shown in Fig. 4.13, laser irradiation in vacuum caused a visible change in the TiO_2 thin film. The irradiated region had a cellular structure [Fig. 4.13(b)] with feature sizes ~10 μm.

When this region was then irradiated in air [Fig. 4.13(d)], the material darkened and formed spherical regions ~3.5 µm in diameter.

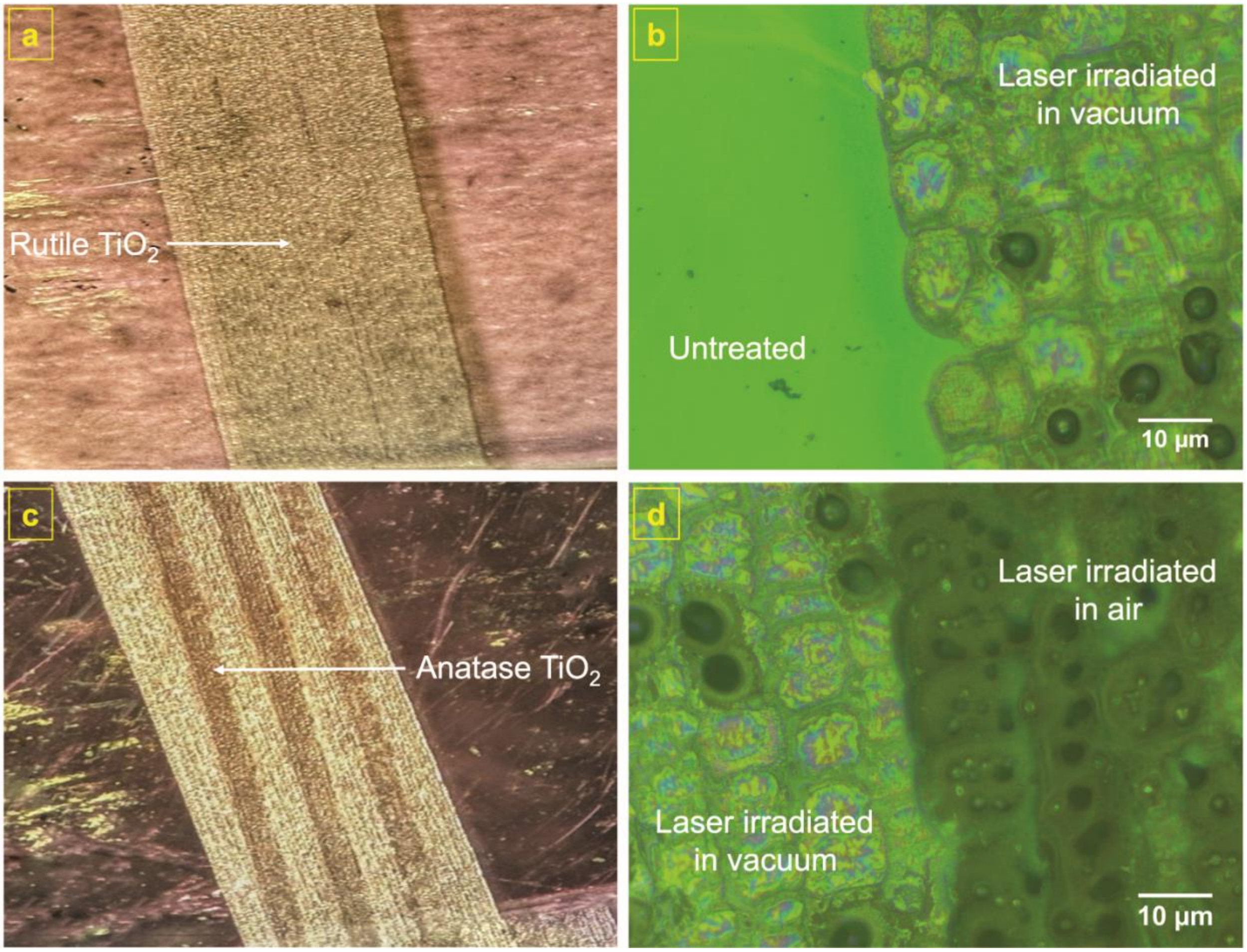

Figure 4.13: (a) Photograph of region (~ 1.5 mm wide, rutile) that was laser irradiated in vacuum. (b) Wide-field microscope image of (a) showing the interface between untreated and laser irradiated regions. (c) Photograph of stripes (~ 0.2 mm wide, anatase) that were laser irradiated in air. These stripes were written on a laser-defined rutile region similar to (a). (d) Wide-field microscope image of (c) showing the interface between regions laser irradiated in air and in vacuum.

Figure 4.14 shows Raman spectra of TiO_2 that was untreated, laser irradiated in vacuum, and laser irradiated in air. Five Raman-active vibrational modes at frequencies 143, 197, 395, 516, and 636 cm^{-1} confirm the anatase phase for the as-deposited, untreated region of the sample. Laser irradiation under vacuum causes a phase transition from anatase to rutile. Three Raman-active modes at 241, 436, and 607 cm^{-1} confirm the phase transformation. The spectra also consist of a faint peak at 147 cm^{-1}. The broad peak around 241 cm^{-1} is a specific feature of the rutile spectrum originating from strong second-order Raman scattering.[127]

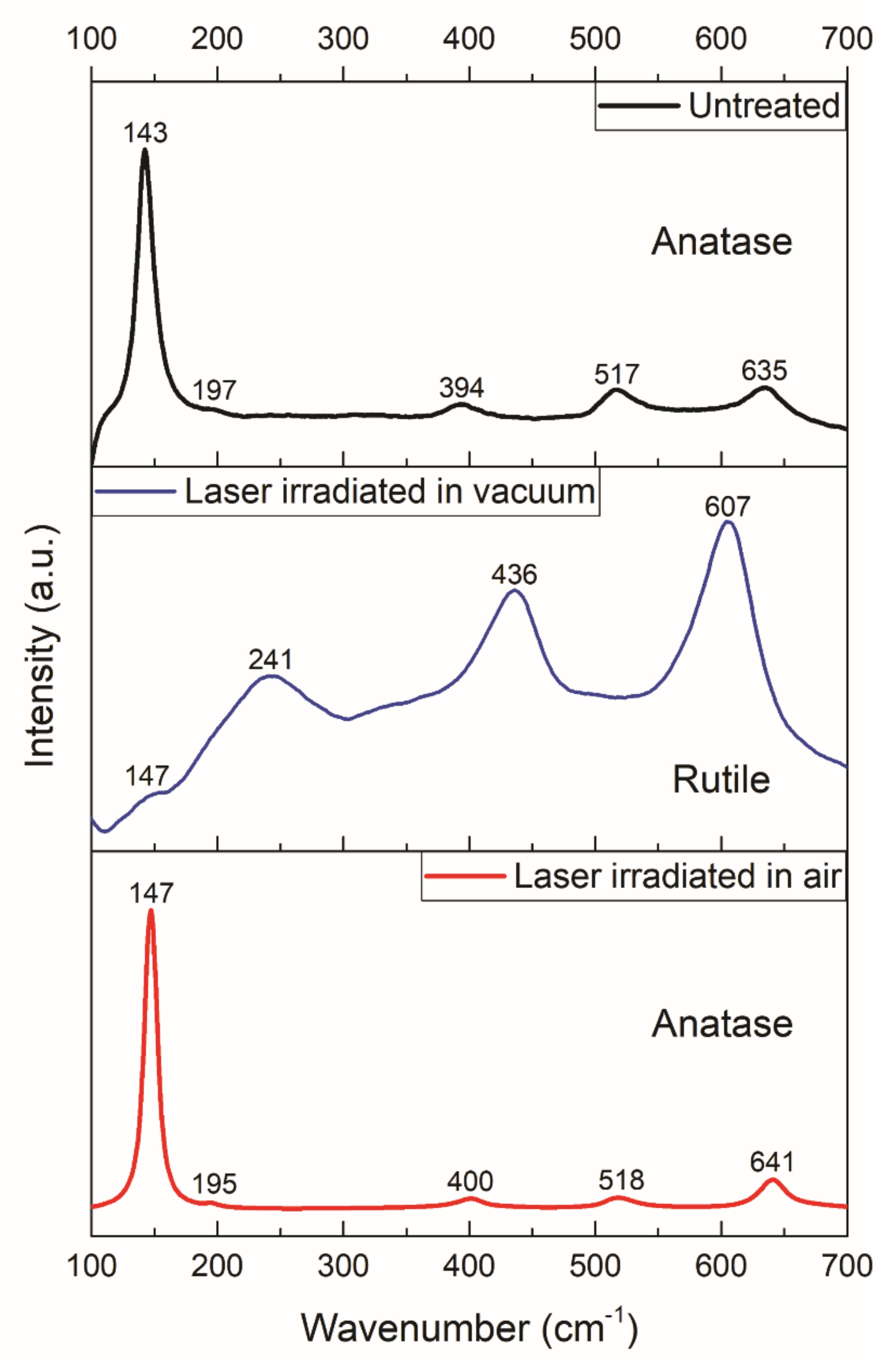

Figure 4.14: Raman spectra of three regions: as-deposited, laser irradiated in vacuum, and laser-irradiated in air.

To transform the phase back to anatase from rutile, laser irradiation in the air was performed on the rutile region. The observed rutile-to-anatase transformation is remarkable because rutile is thermodynamically stable. Five active Raman modes at frequencies 147, 195, 400, 518, and 641 cm^{-1} confirm the rutile-to-anatase phase transition. Peaks around 147, 400, 518, and 641 cm^{-1} are all blue-shifted except the peak at 195 cm^{-1}. The slight shifts in vibrational modes are consistent with disorder due to residual strain and V_O concentration.[125,126,129]

Figure 4.15 shows the Raman spectra of the unexposed laser-irradiated region in vacuum before and after laser irradiation on adjacent regions. The spectra show that the second-order scattering peak around 241 cm^{-1} is blue-shifted while E_g and A_{1g} both red-shifted to 426 and 603 cm^{-1} respectively. The red-shift corresponds to improved crystallinity and expansion of the material, which is consistent with the change in V_O concentration due to laser irradiation. The change in intensity of E_g and A_{1g} modes is consistent with the phonon confinement effects,[130] particularly prominent for the A_{1g} mode which suggests a decrease in crystallite size[131] due to neighboring laser irradiation in air.

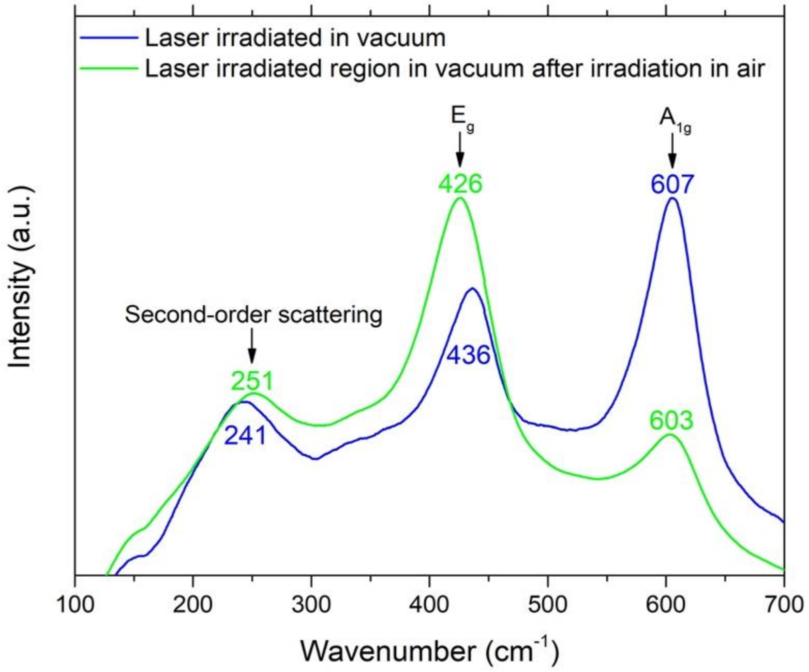

Figure 4.15: Raman spectra of laser irradiated unexposed rutile region in vacuum before and after nearby laser irradiation in air.

Laser irradiation of a TiO_2 thin layer in vacuum resulted in the creation of honeycomb-like repeating structures [Fig. 4.16(a)]. The spatial distribution of point shoot Raman spectra due to the anatase to rutile phase transition using laser irradiation in vacuum is shown in Figure 4.16(b). Our findings suggest that the most intense rutile spectra are found near the structure's edge. We found a faint anatase peak about 486 cm^{-1} in the core of our investigated structure.

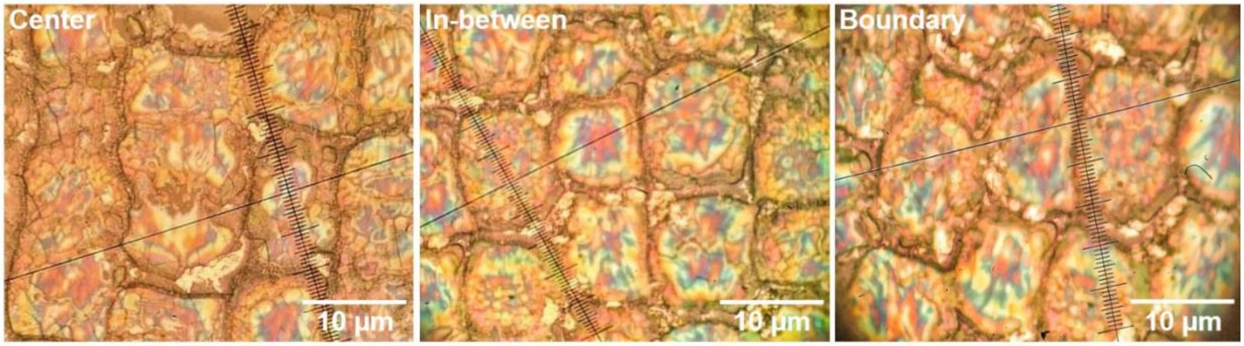

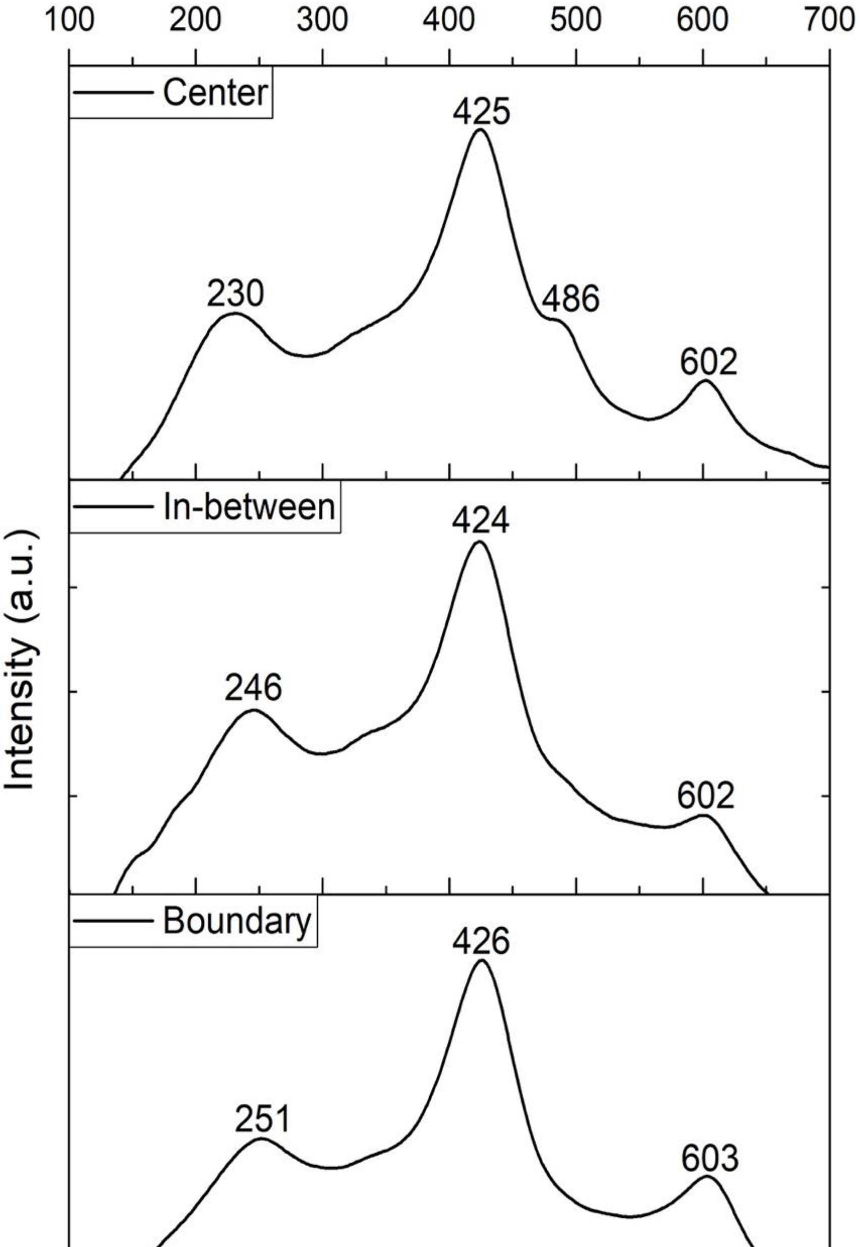

Figure 4.16: (a) Wide-field microscope image of laser treated region in vacuum. (b) Raman spectra across a honeycomb-like structure.

To investigate the phase transition progression from rutile to anatase, we did a similar analysis on the laser-irradiated area. Figure 4.17 shows the formation of sphere-like repeating structure after laser irradiation in the air on a vacuum laser irradiated rutile region (a). The spatial distribution of Raman spectra of the rutile to anatase phase transition using laser irradiation in air can be seen in Figure 4.17(b). Only the anatase phase was found in the middle of these formations. As we measure outside of these structures, the spectrum becomes amorphous, with few to no notable vibrational modes. We saw peaks connected to the rutile and anatase phases coexisting near the edges of the spheres, generating a hybrid phase.

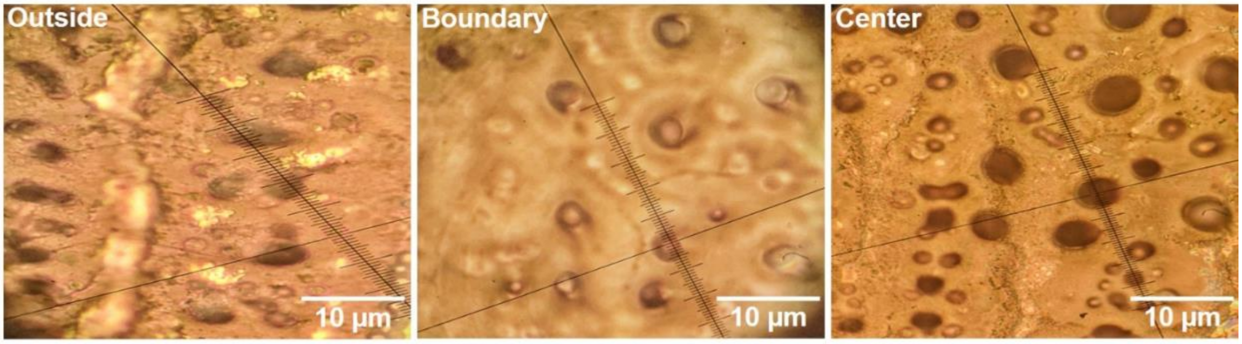

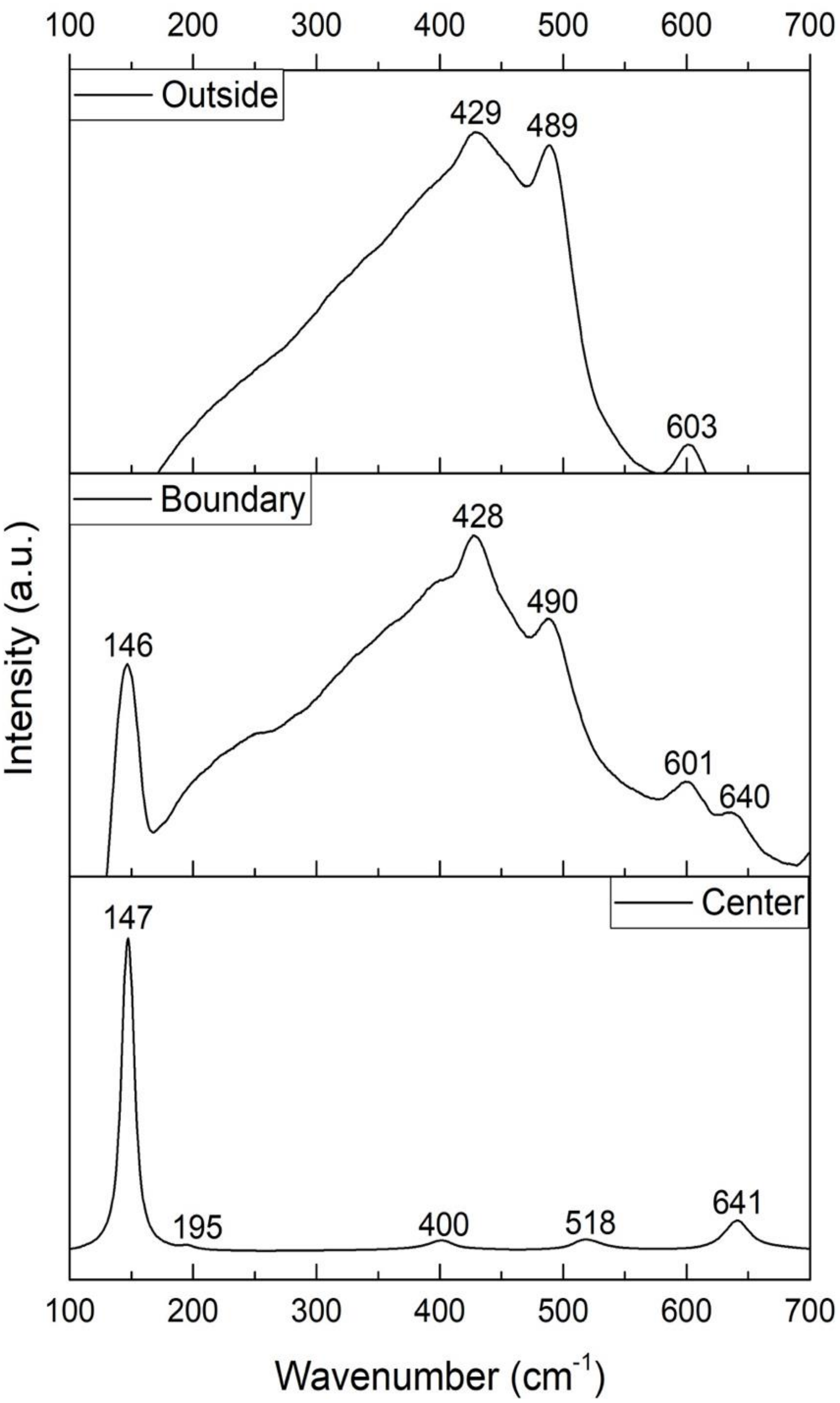

Figure 4.17: (a) Wide-field microscope image of laser treated region in air. (b) Raman spectra across a sphere-like structure.

Micro-Raman mapping was performed under ambient conditions on a $100 \times 100\ \mu m^2$ area. First, we examined the region that was irradiated in vacuum. Figure 4.18(a) shows a Raman map of the E_g mode of anatase TiO_2 (144 cm^{-1}) in red and the A_g mode of rutile TiO_2 (608 cm^{-1}) in green. The spatial Raman intensity distribution shows that anatase indeed transformed to rutile but there are a few residual anatase regions. The strongest rutile signal comes from the cell edges. Some regions in the cell interiors showed a weak, broad spectrum consistent with amorphous TiO_2.

Figure 4.18(b) shows the Raman spectra of regions A-D. Regions A and B are on the boundary of a cell while region C is inside. Regions A-C confirm the localized phase transition from anatase to rutile due to laser irradiation under vacuum. Region D, which is in the interior of a cell, shows no Raman peaks, characteristic of amorphous TiO_2.

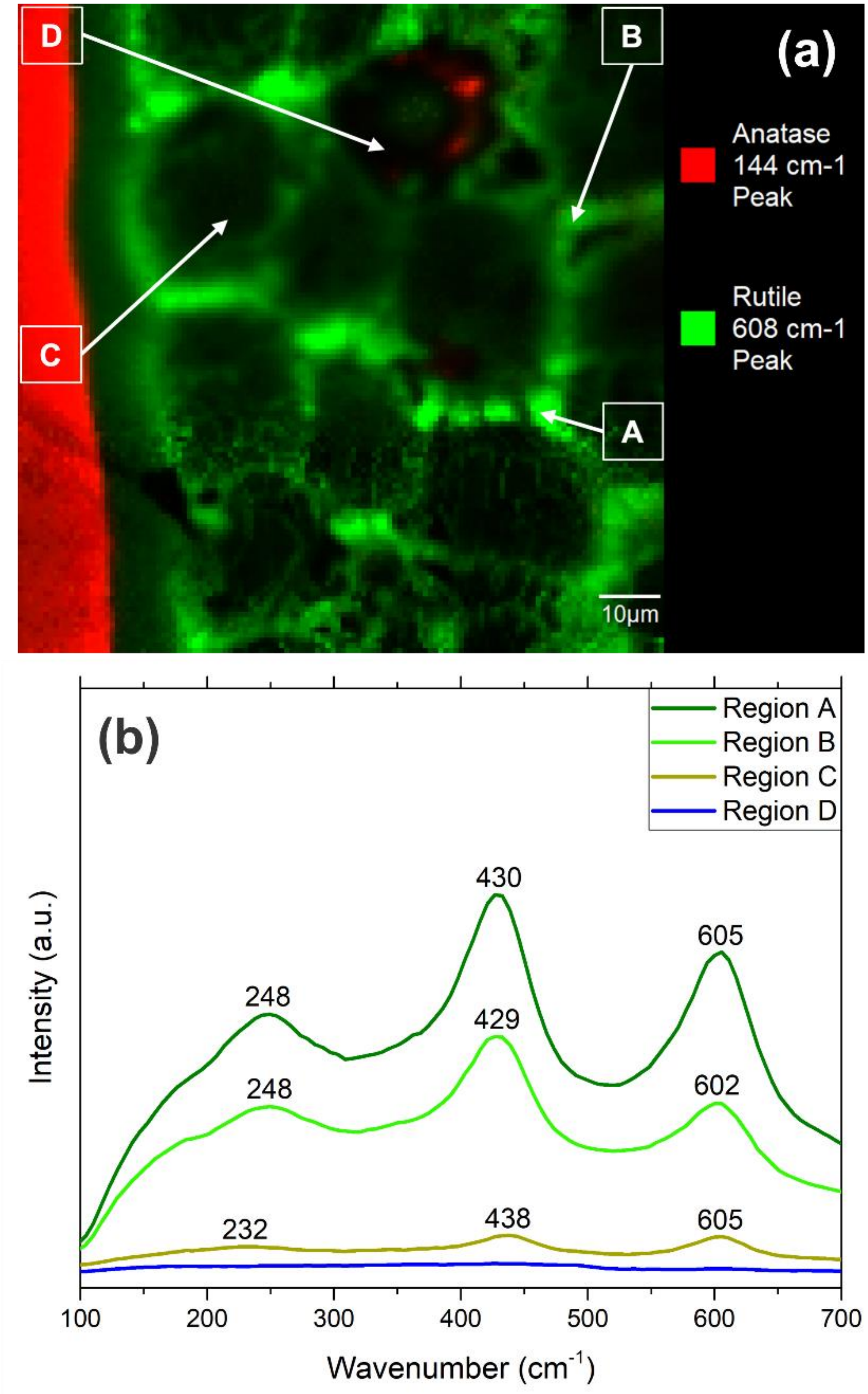

Figure 4.18: (a) Spatial Raman intensity distribution of vibrational modes E_g (anatase) and A_{1g} (rutile) with frequencies 144 cm^{-1} and 608 cm^{-1} respectively. (b) Raman spectra of regions A-D.

Laser irradiating the rutile region in air resulted in a rutile-to-anatase phase transition. Figure 4.19(a) shows a Raman map of rutile and anatase modes. The spatial Raman intensity distribution clearly shows that the anatase signal comes from spherical regions. The Raman active modes disappear as we move from the center towards the edge of the structures. Our results suggest that laser irradiation of the rutile region in air produces anatase spheres surrounded by amorphous material.

Figure 4.19(b) shows the Raman spectra of region A-D. Regions A and B are inside a sphere while regions C and D are located outside. Region A is at the center while B is near the edge, and both show the Raman spectra of anatase TiO_2. Region C is adjacent to a cluster and displays a weak anatase peak around 147 cm^{-1} while region D is far away and appears to be amorphous.

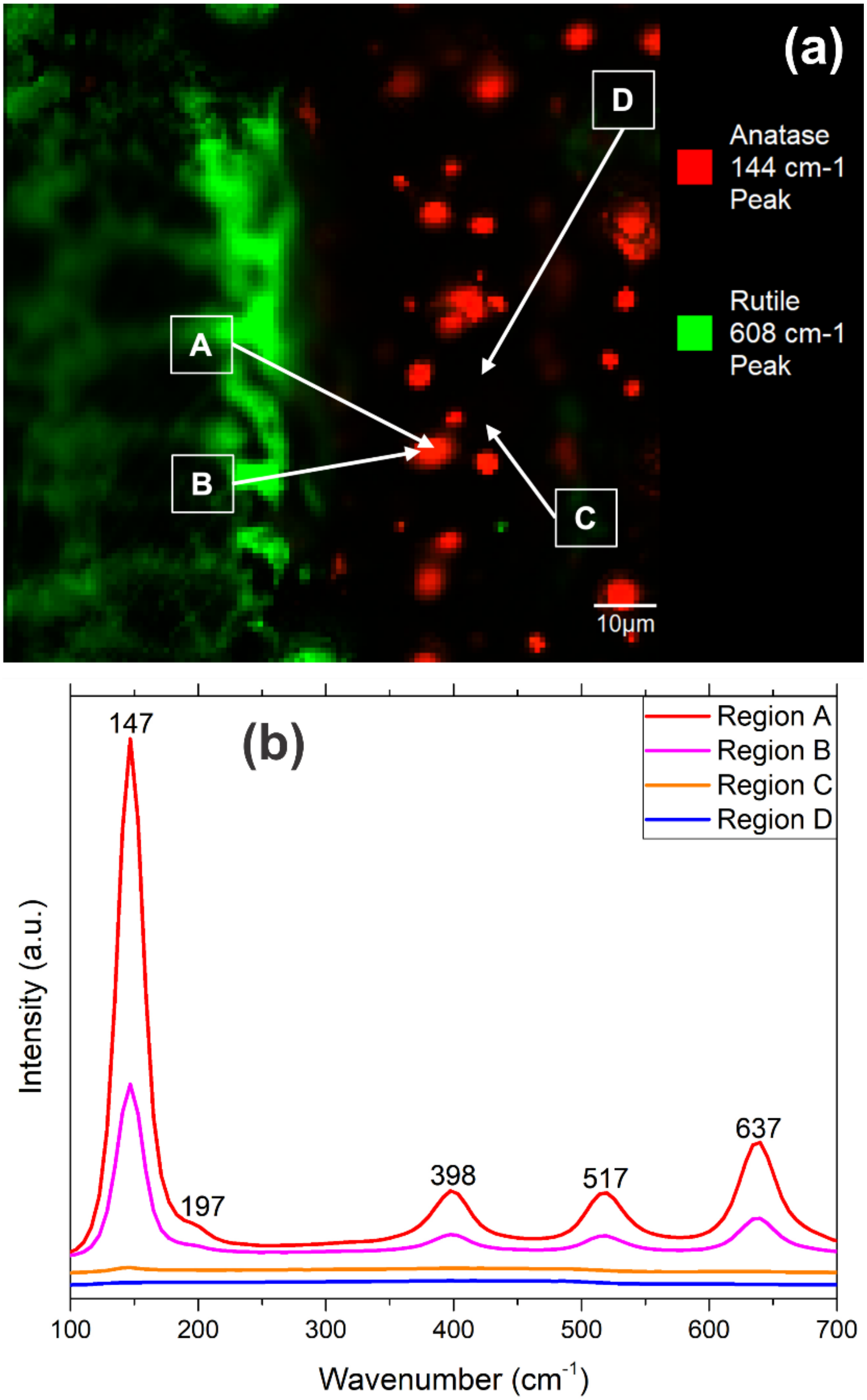
(a)
D
Anatase
144 cm-1
Peak
Rutile
608 cm-1
Peak
A
B
C
10µm
(b)
147
197
398
517
637
Region A
Region B
Region C
Region D
Intensity (a.u.)
100
200
300
400
500
600
700
Wavenumber (cm^{-1})

Figure 4.19: (a) Spatial Raman intensity distribution of vibrational modes A_{1g} (rutile) and E_g (anatase) with frequencies 608 cm^{-1} and 144 cm^{-1} respectively. (b) Raman spectra of regions A-D.

4.5.3: Discussion

Prior work on laser irradiation of TiO_2 nanostructures demonstrated that the atmosphere affects the crystal structure. Irradiation with a high-intensity laser source in the air increases the crystallinity of anatase TiO_2 nanoparticles in the air[132] while irradiation under vacuum, even with relatively low laser power density, degrades the crystalline phase to an amorphous phase.[133] In both cases, the underlying mechanism is athermal and surface oxygen plays a vital role in defining the crystalline structure.[132–134] For the anatase-to-rutile transition under dynamic vacuum, optical excitation generates surface defects, while in air, surface defects are annihilated due to interactions with the surrounding oxygen.[135–138]

In the present study, laser irradiation under vacuum results in an amorphous state and stimulates the desorption of oxygen molecules from the surface. As a result, there is a rapid increase in the oxygen vacancy concentration.[139] These vacancies act as nucleation sites for the stable rutile phase.[140,141] While the anatase-to-rutile transition is relatively straightforward, the *reverse* transition appears to go against thermodynamic stability. However, Raman mapping revealed that the anatase crystals are embedded in an amorphous matrix. It is therefore conceivable that laser irradiation (1) amorphizes the rutile regions and (2) anatase crystals nucleate within the amorphous material.

A schematic diagram for this process is shown in Fig. 4.20. Irradiating the rutile region in air amorphizes the area and leads to localized oxygen adsorption. An oxygen molecule is adsorbed at a surface oxygen vacancy site and stabilizes the surface structure by associating two adjacent Ti sites.[142] This facilitates the nucleation of anatase TiO_2. Our model is consistent with prior work on amorphous TiO_2 thin films, which can transform to anatase after annealing.[143] The fundamental idea is that the laser energy goes into amorphizing the material. The phase of the crystal regions formed within the amorphous matrix depends on the ambient conditions: high(low) oxygen partial pressure results in anatase(rutile).

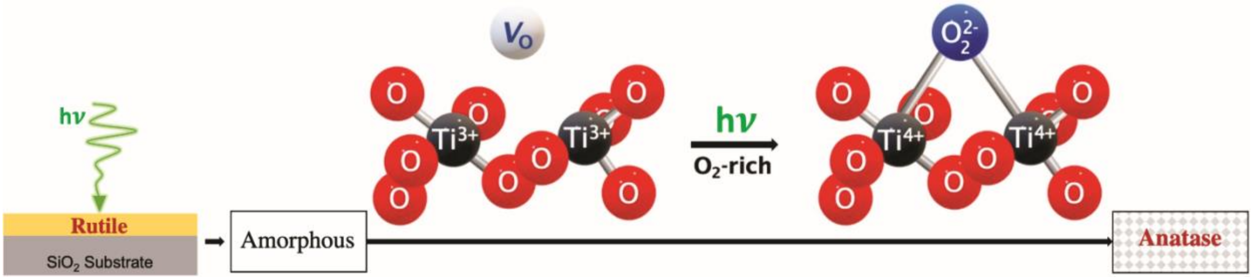

Figure 4.20: Schematic diagram of the rutile to amorphous/anatase phase transition.

4.6: Carbon contamination in thin film-based oxide semiconductors (TiO_2)

Anatase TiO_2 thin films of 300 nm thickness obtained from LGA thin films revealed substantial carbon contamination. When compared to as-deposited samples, the Raman spectra of vacuum annealed films shows the presence of carbon. New peaks appeared around 1300-1600 cm^{-1} after vacuum annealing, in addition to a broad peak at 2930 cm^{-1}. The as-deposited samples did not show any carbon-related Raman modes. However, secondary ion mass spectrometry (SIMS) measurements indicate that the as-deposited films are significantly contaminated with carbon. Furthermore, the IR absorbance spectra revealed peaks related to hydrocarbons.

4.6.1: Raman spectroscopy

Figure 4.21(a) shows Raman spectra of an as-deposited and vacuum-annealed TiO_2 thin film. The Raman measurements were made using a Klar Mini Pro microscope with a laser excitation wavelength of 532.357 nm. The detected spectral region ranged from 0 to 4500 cm^{-1}, with an integration duration of 8 seconds and a 50× objective. Raman peaks at 1350 and 1585 cm^{-1} in the annealed samples correspond to the D[144,145] and G[146] features. These features are common markers of disordered (D) and graphitic (G) C=C bonds.[146,147] The intensities of both peaks are about the same. The D band cannot be observed in completely crystalline graphite because it is composed of defect-induced Raman features, whereas the detection of the G band correlates to the presence of sp^2 carbon networks in the film.[146] The existence of D and G bands indicates that C atoms are congregated. The Raman feature at 2950 cm^{-1} is associated with a D + G combination mode and is known to be associated with disorder.[146] As shown in Fig. 4.21(b), we performed the experiment again with a pair of TiO_2 thin film samples from LGA for a thorough confirmation, which confirmed carbon contamination and the appearance of carbon-related Raman peaks that appeared only after the annealing treatment.

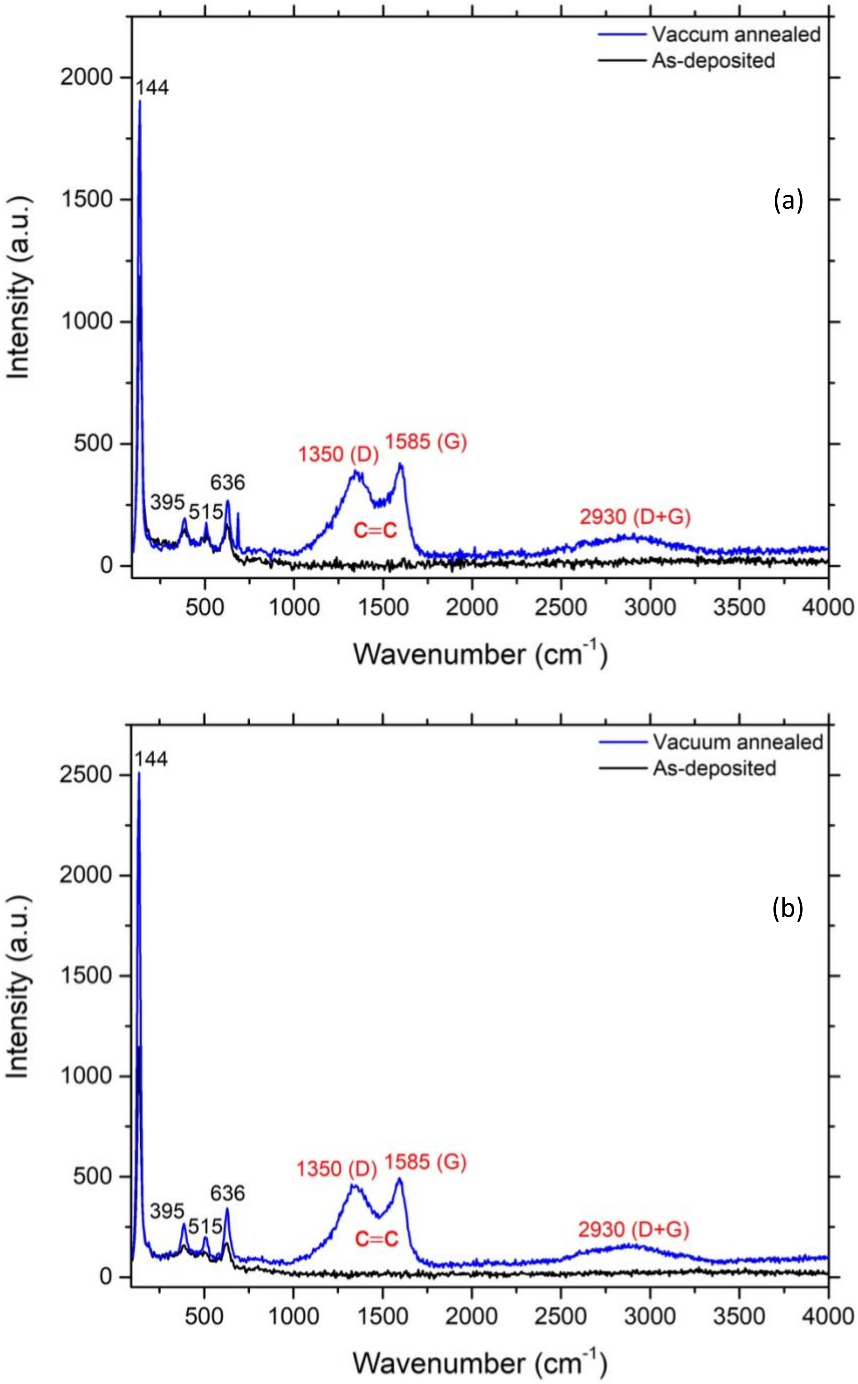

Figure 4.21: Raman spectra of as-deposited and vacuum annealed anatase TiO_2 thin films (800 °C for 3 hours) showing features related to carbon complexes and disorder. (a) and (b) corresponds to two different samples.

4.6.2: Secondary ion mass spectrometry (SIMS)

Secondary ion mass spectrometry (SIMS) was used to obtain chemical profiles of carbon to further investigate the source of contamination in TiO_2 thin films. SIMS analyses were performed with a sputtering beam, collecting secondary ejected ions. SIMS studies were carried out while maintaining a constant and steady surface potential, and the erosion rates in TiO_2 and SiO_2 were used to calibrate the depth scales.

SIMS measurements for an (a) as-deposited and (b) vacuum annealed TiO_2 thin film are shown in Figure 4.22. Both samples notably exhibit a large quantity of carbon. The SIMS data suggest that the as-deposited samples have a high concentration of carbon (~10^{20} atoms/cc) that is evenly distributed throughout the thickness of the film. Vacuum annealing did not change the carbon content significantly. Furthermore, the data suggest no substantial shift in concentration for Ti and O due to the annealing treatment.

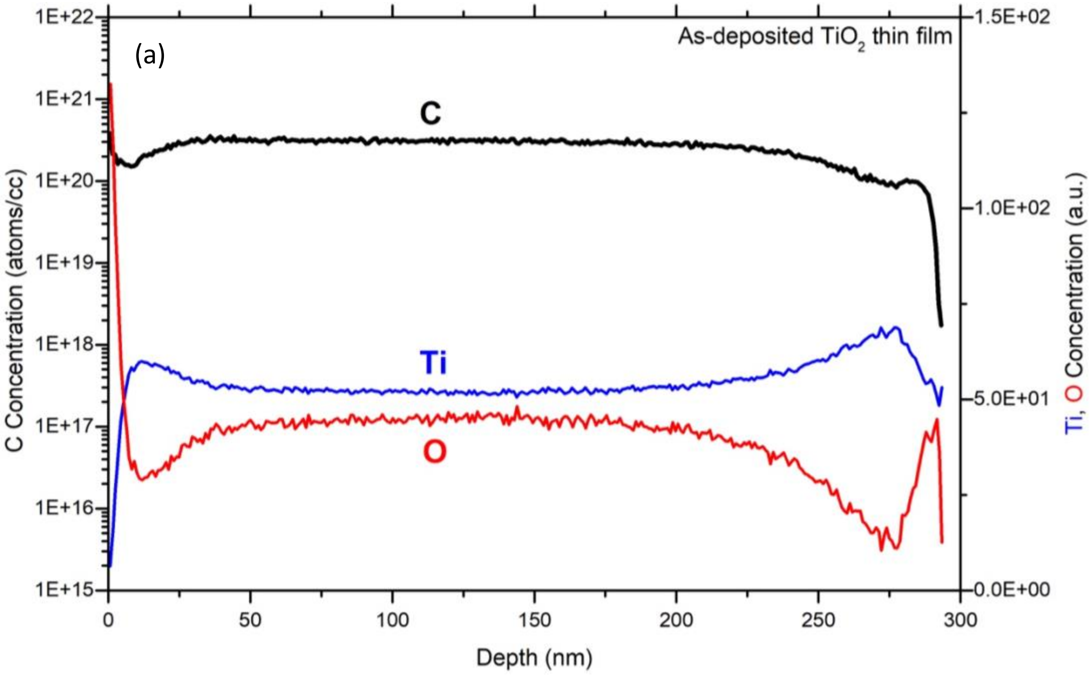

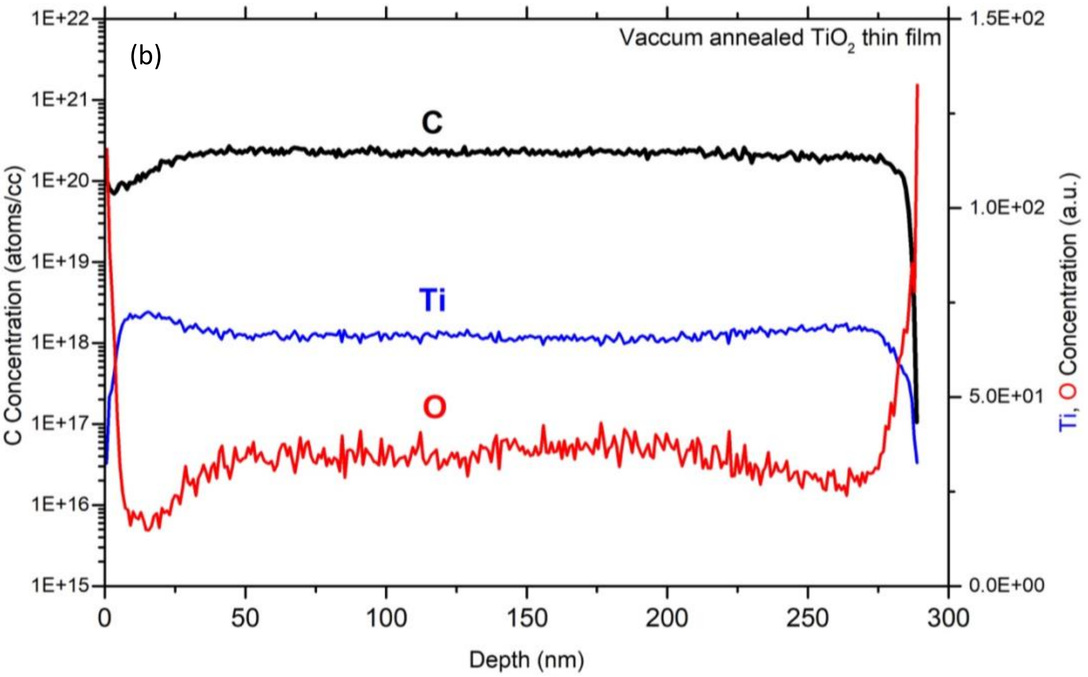

Figure 4.22: SIMS profiles of (a) as-deposited and (b) vacuum annealed (800 °C for 3 hours) anatase TiO_2 thin films. The horizontal axis represents depth of the film (thickness ~300 nm). The left vertical axis reflects the C concentration whereas the right vertical axis represents Ti and O intensity. SIMS data indicates the presence of C in as-received films and that vacuum annealing has no noticeable impact on C concentration.

SIMS measurements were performed to investigate the concentration of hydrogen in the films. The results indicate that the as-deposited samples contain a large amount of uniformly distributed hydrogen [Fig. 4.23(a)]. Vacuum-annealed films on the other hand, show a decrease in H concentration [Fig. 4.23(b)]. The hydrogen concentration decreases as a function of depth, implying that hydrogen trapped deep within the film escapes through the surface during the annealing process.

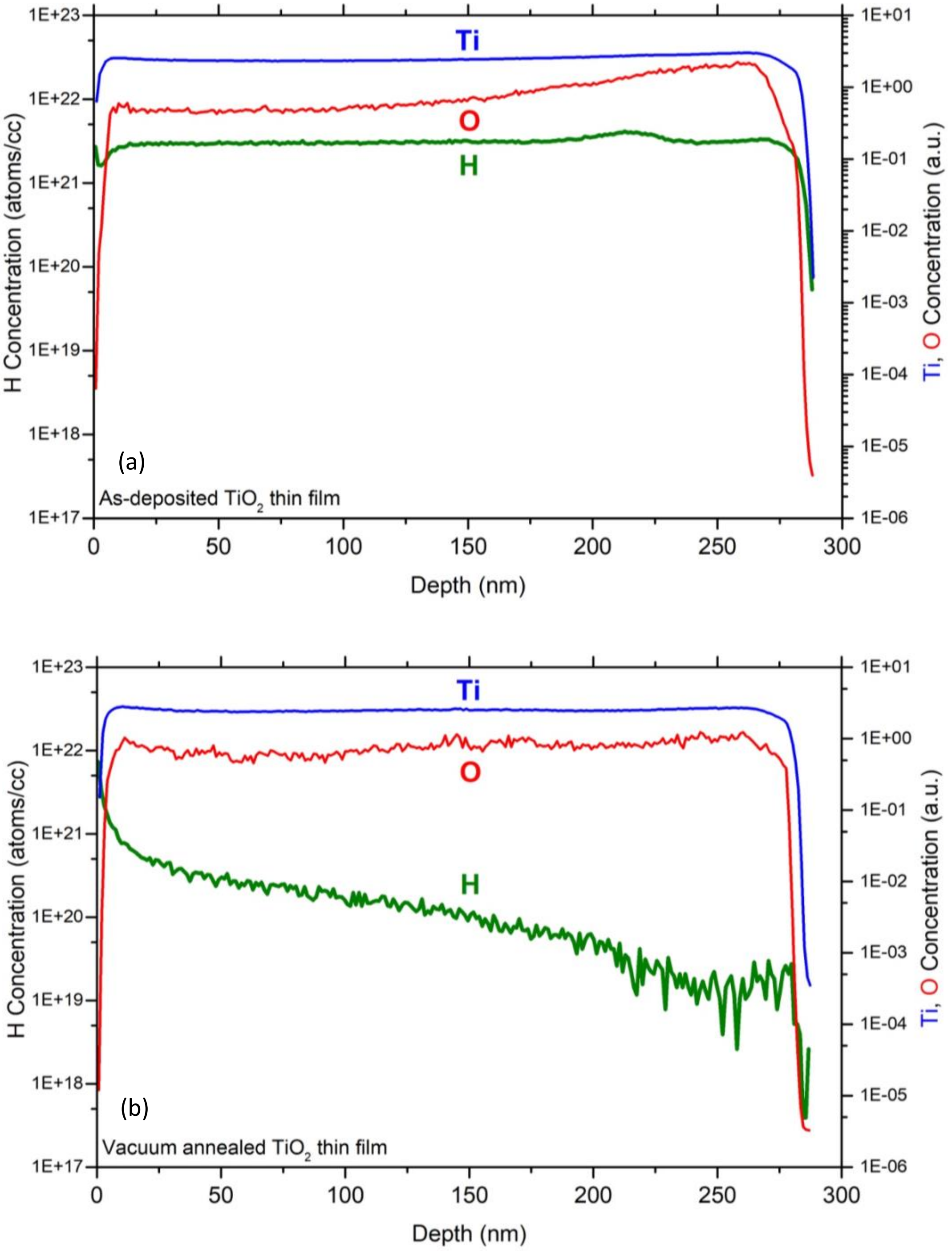

Figure 4.23: SIMS profiles of (a) as-deposited and (b) vacuum annealed (800 °C for 3 hours) anatase TiO_2 *thin films showing H, Ti, and O concentrations. The horizontal axis represents depth of the film (thickness ~300 nm). SIMS data indicates the presence of hydrogen in as-deposited films and demonstrates change in H concentration due to the annealing treatment.*

4.6.3: IR spectroscopy

The IR absorbance spectra of a vacuum annealed TiO_2 thin film is shown in Figure 4.24. The spectrum was baselined against the as-deposited film. The spectra show that the presence of hydrocarbons cause a slight shift in absorbance in the 2800-2900 cm^{-1} region. This region, however, overlaps with the equipment's background spectra and therefore not a reliable indicator of a change in carbon complexes due to the annealing treatment. The peak at 2340 cm^{-1} relates to CO_2, while the feature around 3670 cm^{-1} might be related to the fused silica substrate.

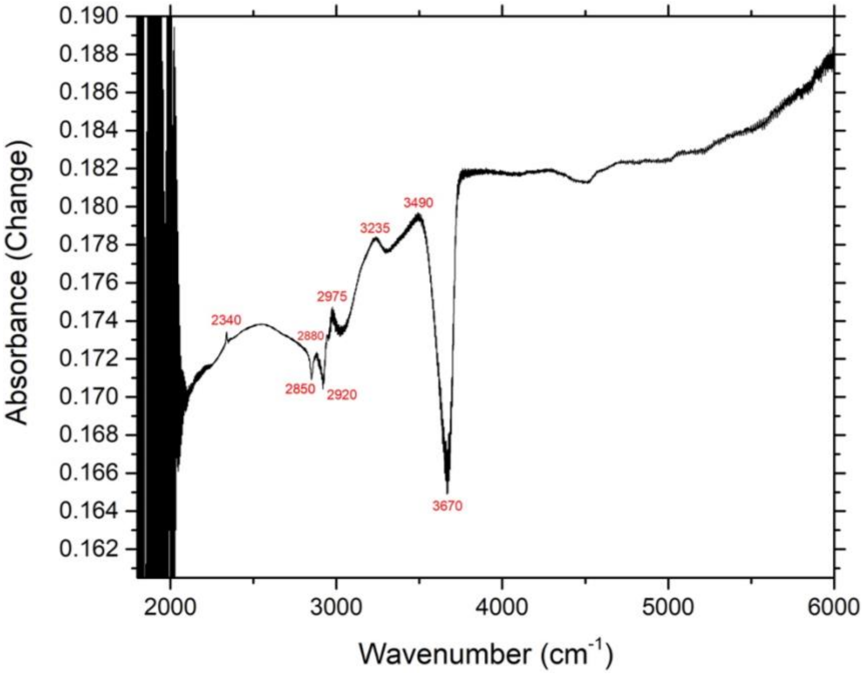

Figure 4.24: IR absorbance spectra of a vacuum annealed (800 °C for 3 hours) anatase TiO_2 thin film baselined against the as-deposited film showing change in absorbance related to hydrocarbons.

4.7: TiO_2 thin film with reduced levels of carbon contamination

To study the role of carbon in sub-bandgap photon absorption and processing thin film-based oxide semiconductors, we received anatase TiO_2 thin films with low contamination levels and comparable thickness sputtered on fused silica substrates. The films were sputtered[143] by the Tate group at Oregon State University (OSU).

The films were sputtered using an Orion 5 sputter deposition chamber at a base pressure of 5×10^7 mTorr. The sputtering process includes a metallic Ti target and a mixture of Ar + Ar/O_2 gases. The sputtering power was set to 90 W, and the deposition rate was tuned at approximately 2 nm/min. The precursor films were annealed in an AET Thermal RX Series Rapid Thermal Annealing (RTA) device in a flowing N_2 atmosphere to generate the anatase polymorph. The annealing process is to rapidly heat the films to 400 °C, maintain it for a few minutes, and then turn off the heat, allowing the films to rapidly drop to ambient temperature. The annealing furnace was not hermetically sealed, thus some oxygen from the atmosphere might diffuse into the sample.

The as-deposited and vacuum annealed TiO_2 thin films are shown in Figure 4.25. Films are conductive and roughly 365 nm thick when deposited. Consequently, as-deposited samples appeared dark, indicating that they absorb more in the visible regions of the spectrum. After vacuum annealing the films under the same conditions as the LGA samples, we measured an order of magnitude increase in resistance and improved transmission.

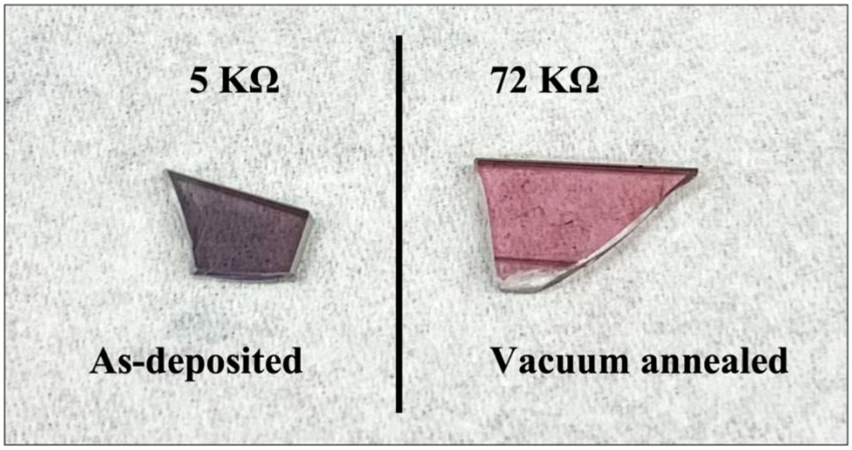

Figure 4.25: RF sputtered ~365 nm thick TiO_2 thin films, as-deposited and vacuum annealed. The as-deposited film shows a resistance of ~5 KΩ. Annealing the sample under vacuum increases the resistance to ~72 KΩ.

The anatase TiO_2 characteristic peaks are detected in the Raman spectra of the as-deposited and vacuum annealed samples (Fig. 4.26). Specifically, Raman peaks at 144, 395, 515, and 636 cm^{-1} confirm the anatase phase. As observed earlier, only the vacuum annealed film shows graphitic carbon-related features. consequently, as predicted, the level of carbon contamination is quite low in comparison to the LGA films.

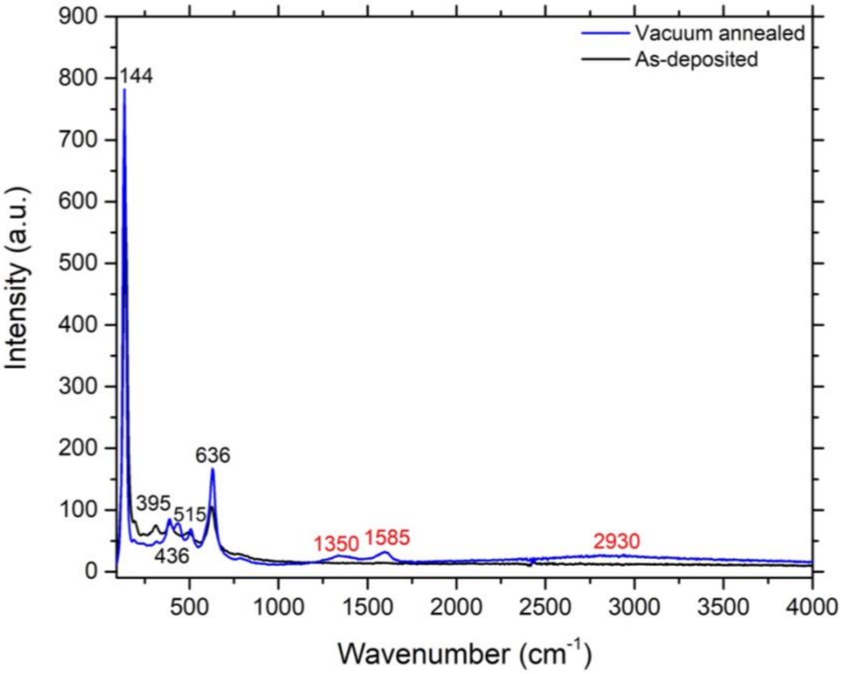

Figure 4.26: Raman spectra of as-deposited and vacuum-annealed 365 nm thick anatase TiO_2 thin films (800 °C for 3 hours). The vacuum annealed film shows faint features related to carbon.

An in-depth analysis of the vacuum annealed TiO_2 thin film Raman spectra [Fig. 4.27(a)] shows characteristic Raman peaks associated to the anatase phase, demonstrating that the annealing treatment has no effect on phase. Figure 4.27(b) shows small peaks associated with graphitic carbon modes. The faint peaks at 1350, 1585, and 2930 cm^{-1}, suggest a low concentration of disordered carbon networks.

Figure 4.27(c) compares carbon-related contamination in LGA and OSU TiO_2 thin films based on their peak intensity. The intensity of the Raman peaks associated to the graphitic carbon modes clearly shows, minimal levels of contamination in the OSU films in comparison to the considerable amount of carbon contamination in the LGA films.

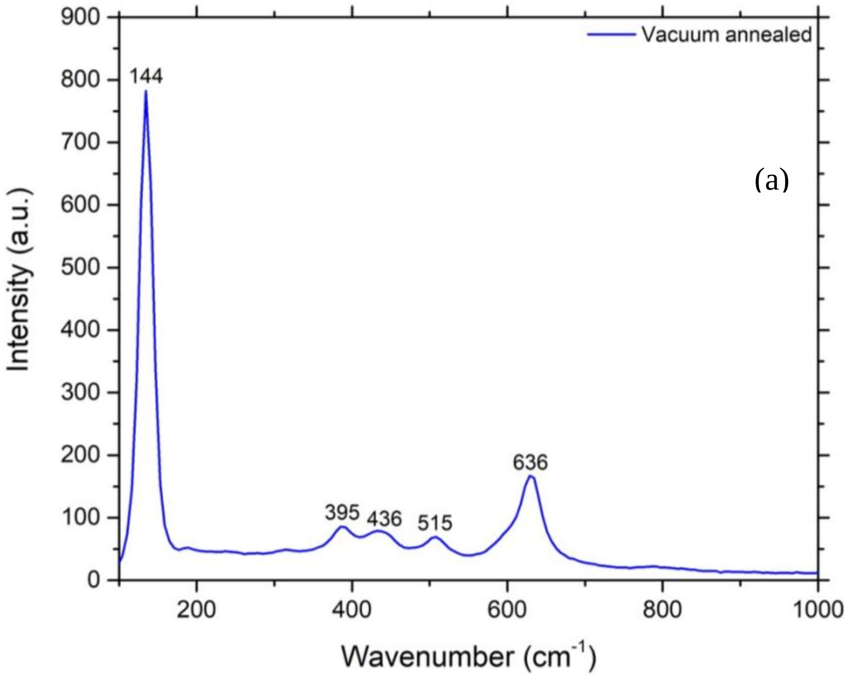
Vacuum annealed
(a)
144
395
436
515
636
Intensity (a.u.)
0
100
200
300
400
500
600
700
800
900
200
400
600
800
1000
Wavenumber (cm^{-1})

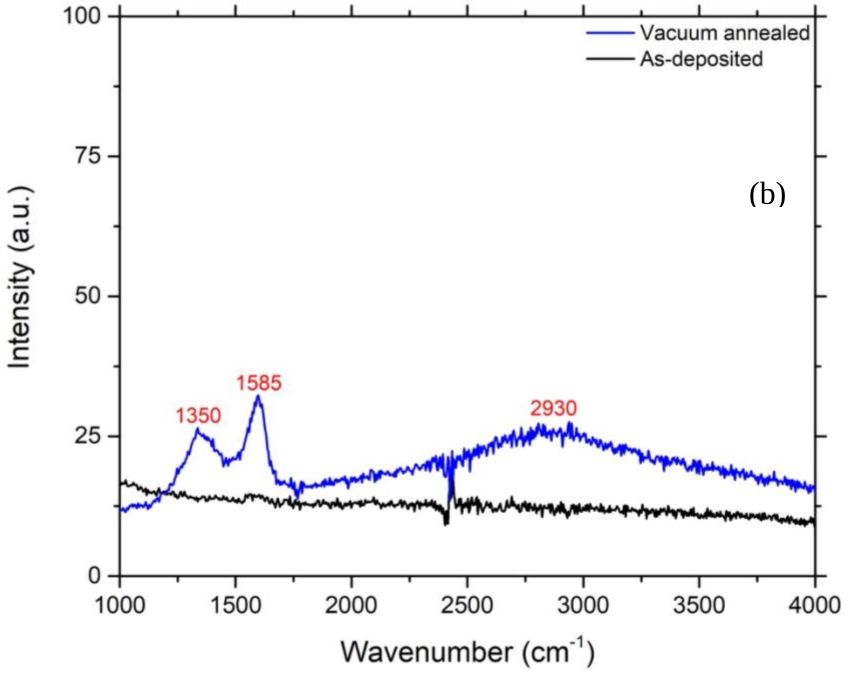
Vacuum annealed
As-deposited
(b)
1350
1585
2930
Intensity (a.u.)
0
25
50
75
100
1000
1500
2000
2500
3000
3500
4000
Wavenumber (cm^{-1})

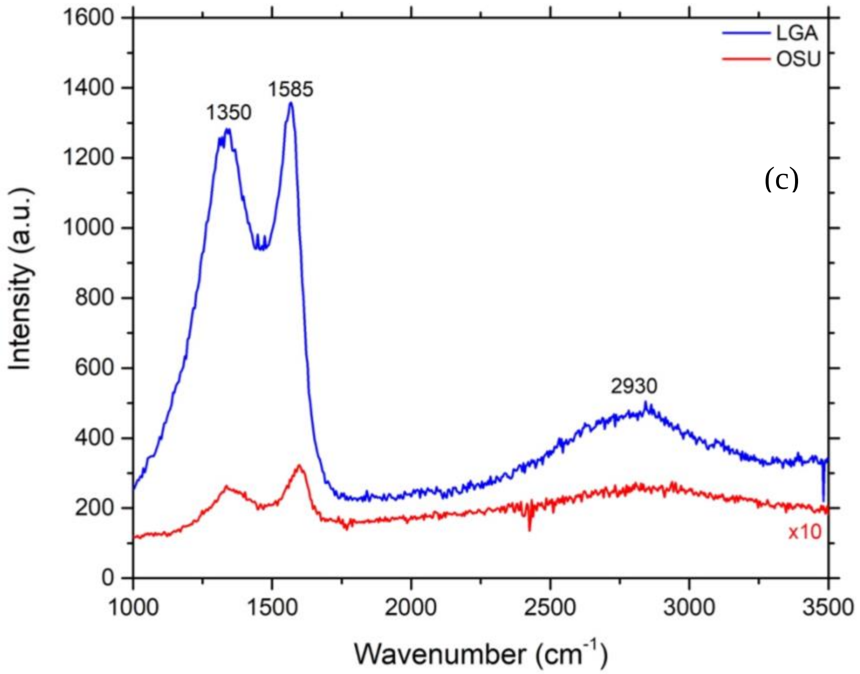

Figure 4.27: Raman spectra of a vacuum annealed anatase TiO_2 *thin film. (a) characteristic peaks of anatase* TiO_2*. (b) Showing weak peaks and faint feature related to carbon complexes and disorder. (c) Comparing carbon-related contamination between LGA and OSU (10× intensity)* TiO_2 *thin films.*

To study the effect of carbon contamination in interacting with sub-bandgap laser to facilitate the optical processing of thin film-based oxide semiconductors, an optically pumped semiconductor laser (Coherent Verdi G series) with a wavelength of 532 nm and a beam diameter of 2.25 mm was used to irradiate the thin films. The laser beam was focused to a diffraction-limited diameter of ~100 μm. To draw resistive regions, 1.6 W and 1 W of laser power was used as seen in Fig. 4.28. Exposure to sub-gap laser raised the film resistance by three orders of magnitude locally, whereas heavily contaminated films showed resistance increases roughly up to seven orders of magnitude (Sec 4.4.2.a). The optical transmission also increased in the laser-irradiated regions. There was no change in phase due to laser treatment. The reduced shift in resistance caused by laser irradiation might be attributed to lower levels of carbon contamination in the film, which could be partially responsible for localized heating and electronic excitation through facilitating increased absorptions in the sub-gap region.

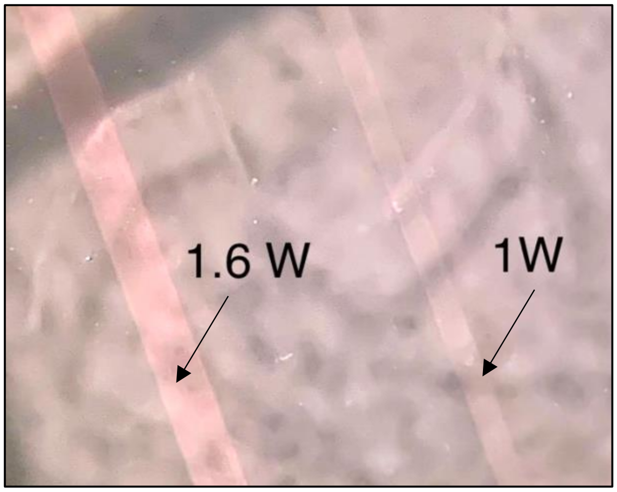

Figure 4.28: Photograph of a laser treated 365 nm thick anatase TiO_2 *thin film showing 1.6 W and 1 W laser irradiated resistive bands.*

4.8: Carbon cleaning using sub-bandgap laser

Laser treatment using a 532 nm sub-bandgap laser has the ability to decrease carbon contamination in oxide based thin film semiconductors. Figure 4.29 shows the Raman spectra of a vacuum-annealed untreated and laser treated TiO_2 thin film. The vacuum annealed film shows large amount of contamination. Irradiating the sample using a sub-bandgap laser, under ambient conditions, considerably decreases the carbon content locally and restores transmission partially. Raman spectra shows that the peaks associated with disordered graphitic carbon and combination mode are nearly gone following the laser treatment. The intensity of the peaks associated with the anatase phase also grows due to illumination showing an increase in crystallinity.

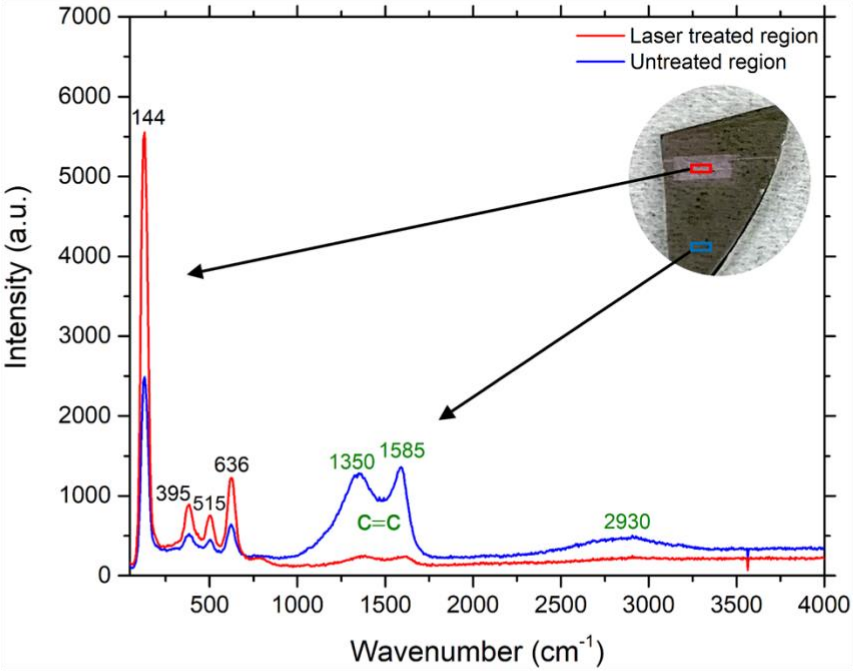

Figure 4.29: Raman spectra of vacuum annealed, laser treated region on a TiO_2 thin film demonstrating the carbon contamination and the impact of a 532 nm sub-bandgap laser in substantially reducing contamination level.

The effect of laser irradiation on carbon contamination was investigated further using Raman mapping. The Raman map (Fig. 4.30) demonstrates the difference in carbon content across the interface between the laser-treated and untreated regions of the film. Figure 4.30(a) shows the spatial Raman intensity distribution of the characteristic D (1350 cm^{-1}) band which is unique to the amorphous (sp^3) carbon[148] network. The map demonstrates that laser treatment significantly reduces the contamination locally. The slight fluctuation in peak intensity across the treated region could be related to the irradiation time.

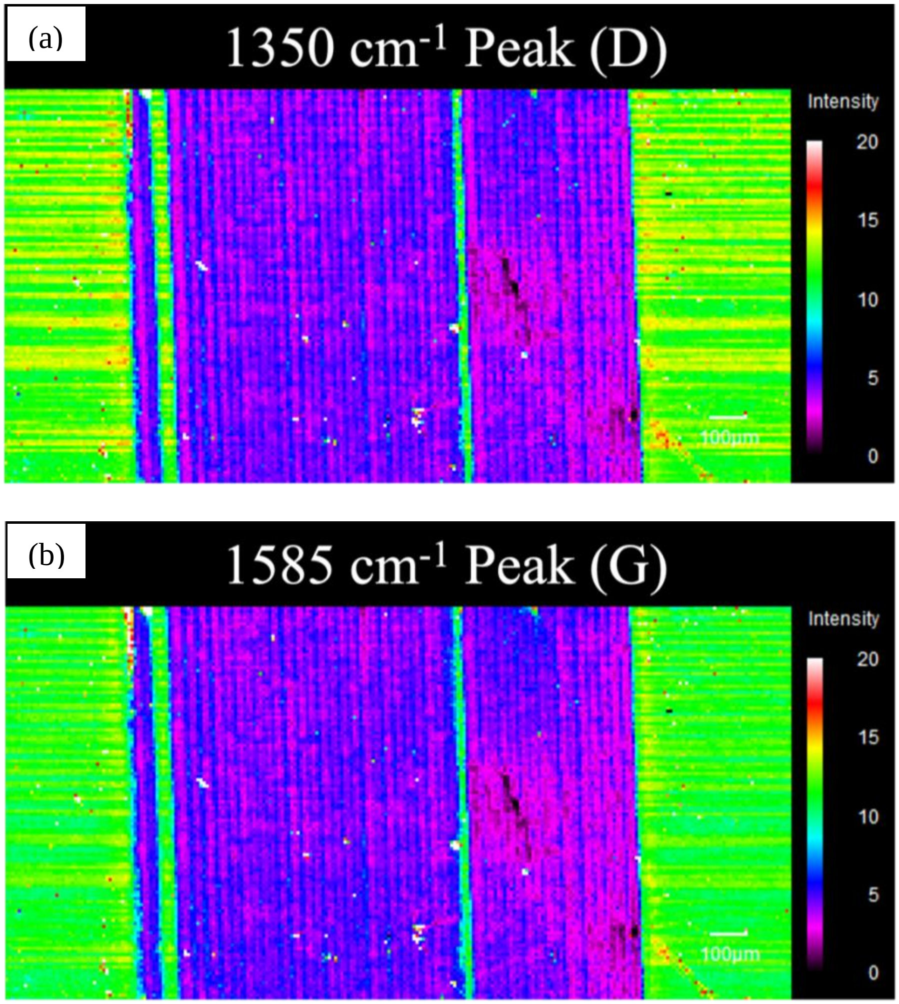

Figure 4.30: Raman map of vacuum annealed, laser treated region on a TiO_2 thin film showing the spatial Raman intensity distribution of the characteristic (a) D and (b) G modes. These images show the effect of a 532 nm sub-bandgap laser in reducing the carbon contamination level.

Figure 4.30(b) shows the spatial Raman intensity distribution of the characteristic G (1585 cm^{-1}) band. The band corresponds to the graphitic carbon (sp^2). The Raman map indicates that the laser treatment likewise diminishes the graphite mode. The relatively small variations in peak intensity over the treated region might be again attributable to the irradiation length. The intensity between the D and the G bands are quite comparable in both laser treated and untreated regions of the film. The I_D/I_G intensity ratio between the bands is roughly one, implying an equal quantity of amorphous and graphitic material precipitated during annealing,[148] which was decreased following laser irradiation.

A schematic diagram for the process is shown in Fig. 4.31. Carbon atoms in a TiO_2 thin film cluster following a vacuum anneal. Irradiating the annealed film in air, dissipates carbon locally and forms CO_2 (gas). The fundamental idea is that the carbon in the film improves visible absorptions, resulting in carbon combustion triggered by laser-assisted localized heating.

Carbon was gradually removed from the sample by laser irradiation. Irradiation treatment leads to increased crystallinity of the sample. However, irradiation-assisted carbon removal is not seamless. As a result, some C atoms persisted in the film.

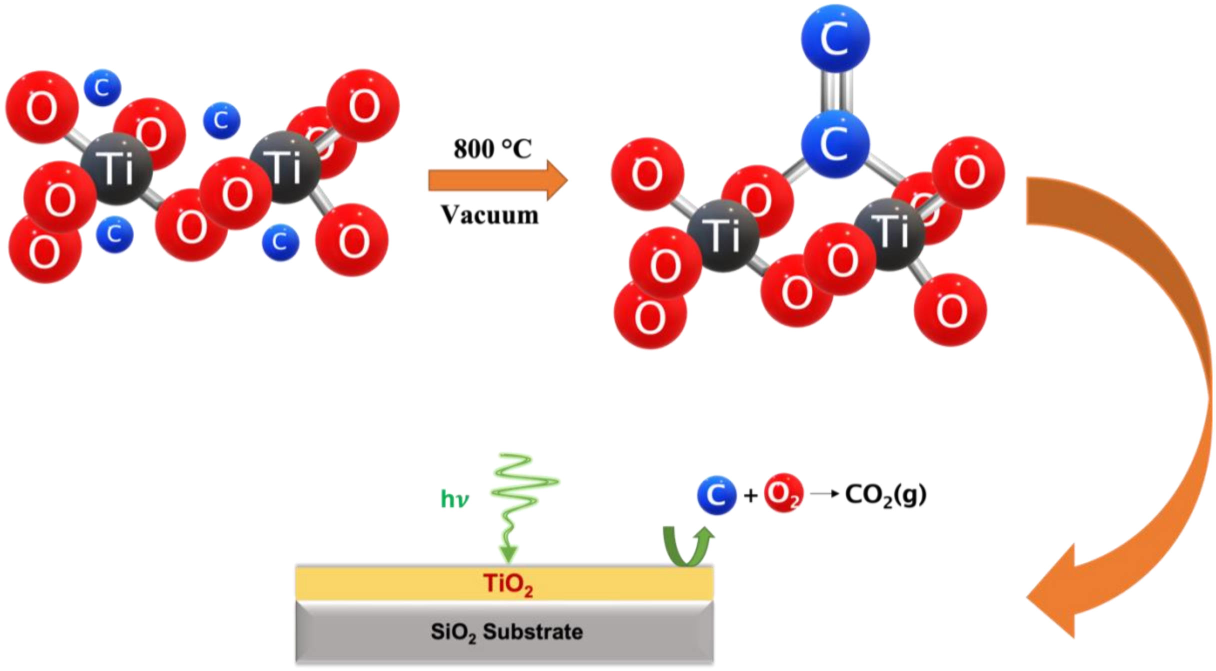

Figure 4.31: Schematic diagram of laser-assisted carbon cleaning process in sputtered TiO_2 thin films.

CHAPTER FIVE: TITANIUM DIOXIDE CONCLUSIONS AND FUTURE WORK

5.1: Conclusions

Localized laser irradiation with subgap photons can be used to optically fabricate resistive regions in a conductive TiO_2 thin film. First, vacuum annealing increases the number of oxygen vacancies in the film, resulting in increased conductivity and resistance values in the hundreds of KΩ range. Laser irradiation increases resistance by seven orders of magnitude, attributed to a reduction in the concentration of oxygen vacancies.[149] This is in contrast to hard-UV laser excitation, which creates, rather than eliminates, oxygen vacancies.[149] Optical transmission spectra showed visible absorption in the vacuum-annealed sample that is reduced upon laser treatment. Localized laser irradiation caused no substantial changes in surface morphology, composition, or vibrational structure. These findings imply that the laser treatment does not degrade the film or affect the material's phase. Changes in conductivity are persistent over time and annealing the sample again under vacuum with identical conditions restored the conductivity, suggesting that the process is reversible.

Anatase TiO_2 thin films transform to a mixture of rutile and amorphous material when irradiated by a green laser under vacuum. Subsequent irradiation in air leads to an amorphous/anatase mixture. This latter process is unusual because the rutile phase is thermodynamically stable. The key to the rutile-to-anatase transition is likely the formation of an intermediate amorphous phase. In the presence of oxygen, anatase crystals are nucleated in the amorphous matrix.

Raman mapping revealed that the rutile phase has a cell-like structure while the anatase phase occurs in spherical regions. The reason behind these different geometries is not clear.

However, they may be linked to the laser power dispersion during irradiation. Along these lines, the highly focused Raman laser spot does not induce a phase transition, which suggests that the specific beam profile parameters are important.

Carbon contamination in thin-film transparent oxide semiconductors might play a vital role in enhancing light absorption in the visible spectrum. The form of carbon present in the as-deposited TiO_2 appeared to be Raman inactive. Carbon precipitates out and forms clusters following an anneal under vacuum. SIMS data show that the as-deposited films contain large amount of carbon and hydrogen. For the vacuum-annealed sample, the hydrogen concentration decreases as a function of depth, suggesting that hydrogen out-diffuses through the surface during the annealing process. Raman peaks at 1350 and 1585 cm^{-1} in annealed samples refer to the D and G features. These features are representative of disordered (D) and graphitic (G) C=C bonds. The Raman feature at ~ 2930 cm^{-1} is linked with a D + G combination mode and is also due to disorder.

We propose that oxygen vacancies *and* carbon impurities both contribute to laser induced changes. 532 nm continuous wave (CW) laser light is absorbed by the V_O defect, resulting in an electronic excitation. This excitation is accompanied by localized heating due to absorption by graphitic carbon clusters. The combination of electron excitation and heating leads to a significant change in conductivity and/or promotes phase transitions. TiO_2 thin films with low carbon content show smaller changes in conductivity caused by laser irradiation.

Our results suggest that laser treatment can be used to reduce carbon contamination in thin-film transparent oxide semiconductors. Carbon cleaning in TiO_2 sputtered thin films could proceed as a two-step process. During the first step, vacuum annealing causes carbon precipitation, which leads to clustering. For the second step, photons are absorbed by the clusters. The carbon is oxidized and form CO_2 (gas), resulting in a significant drop in contamination levels.

5.2: Future work

Based on the studies on persistent photo-resistivity, localized laser irradiation can be used to define insulating pathways in TiO_2 thin films. Vacuum annealing can erase those patterns, enabling rewritable electronics. Further work can be carried out to define conductive channels at room temperature on an otherwise insulating film. Furthermore, our studies on crystal phase transitions using laser irradiation should be expanded to better understand the rutile to anatase phase transition mechanism. The role of carbon contamination in absorbing sub-bandgap light which acts as a catalyst for localized change in resistance and phase transition, should be explored.

Oxide semiconductors and insulators are currently used in a wide variety of devices and are being actively researched for applications in energy generation and storage, optoelectronics, and transparent electronics. The variety of characteristics displayed by oxide materials opens a plethora of opportunities for innovative electrical devices. The research insights can have far-reaching implications beyond TiO_2, resulting in a wide range of laser-processed materials.

TiO_2 is an *n*-type semiconductor whose conductivity is known to be largely influenced by the oxygen vacancies (V_O), which act as shallow donors. Adjusting the laser irradiation parameters to tailor the V_O, future studies can be done to define conducting regions on an otherwise insulating film and restore resistivity of a part of the pattern (Fig. 5.1). Additionally, designing variable conducting and resistive routes by altering the laser power density, is a promising research direction.

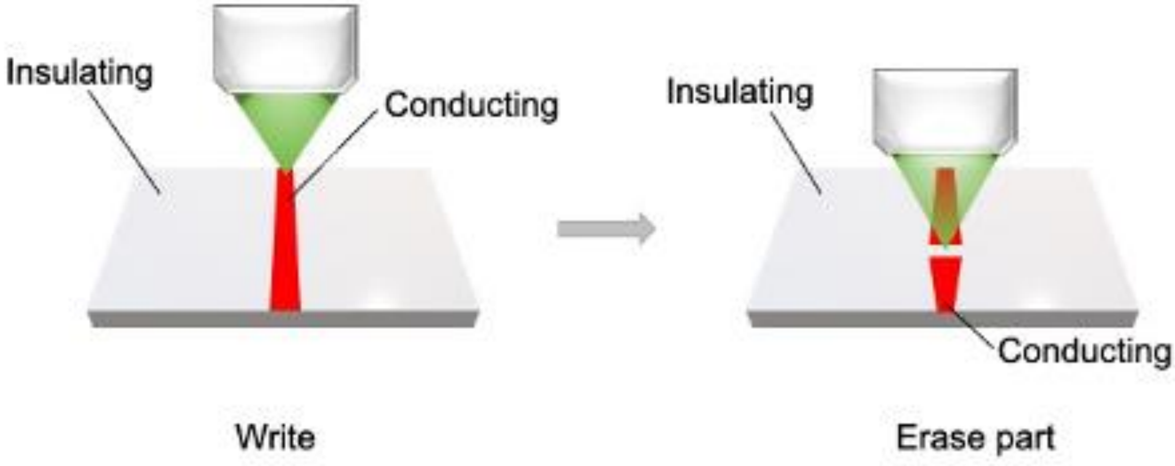

Figure 5.1: Conductive channel defined by laser irradiation. Irradiating under certain ambient conditions erases a portion of the path.

Electrical characteristics such as free electron concentration, mobility, and resistivity may be evaluated at a variety of temperatures[150] utilizing Hall-effect measurements to optimize the anatase TiO_2 thin film room temperature conductivity. Future research might increase understanding of the phonon scattering mechanisms that limit electron mobility in TiO_2 thin films by studying their electrical characteristics.

Future research should be conducted to determine the actual defect level responsible for the laser-induced electronic transition in TiO_2 thin film by investigating sub-bandgap absorption and its connection with oxygen vacancies using photoluminescence (PL) and photoluminescence excitation (PLE).

Future studies should be done to analyze the laser-material and laser-defect interactions to determine the effect of ambient conditions and the level of laser heating. Such studies would address the mechanism underlying phase transitions and conductivity changes associated with subgap laser irradiation. To evaluate the interaction dynamics and explore the temperature changes associated with laser treatment, in-situ Raman measurements may be performed during irradiation under different ambient conditions, laser power density, and exposure time. To assess the influence of contact heat conduction, different substrates can be explored.

Future tests might be carried out to illustrate the impact of the laser processing technique by printing test patterns on TiO_2 thin films (Fig. 5.2). Insulating lines with varied widths, resistors with varying conductivity, 3D circuits, and structures with mixed anatase/rutile phase are some of the potential candidates. These test patterns will allow to further investigate the spatial limits and future applications of the laser-based processing technique.

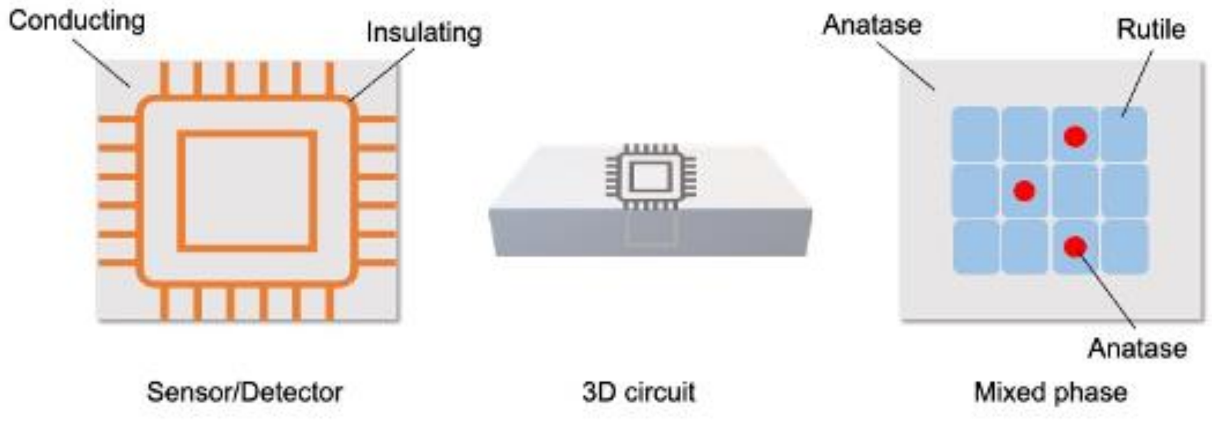

Figure 5.2: Schematics of the possible test patterns defined by sub-bandgap laser irradiation.

Future research can focus on intentionally doping TiO_2 thin films with carbon to create better performing photocatalyst. Carbon doped TiO_2 bandgap may then be tuned locally using our novel laser processing approach. This might open new opportunities for fabricating next generation photocatalytic transparent circuits and sensors.

Carbon is one of the most ubiquitous impurities,[151] and it is known for altering the lattice's physical and chemical characteristics.[147,152] Future research should look towards using laser cleaning to remove undesired carbon from sputtered thin films.[151] This could enable the development of a cost-effective and long-term approach of removing carbon contaminants.

CHAPTER SIX: ROOM TEMPERATURE PERSISTENT PHOTOCONDUCTIVITY IN BARIUM CALCIUM TITANATE ALLOYS ($Ba_{1-x}Ca_xTiO_3$)

6.1: Introduction and motivations

6.1.1: Barium titanate ($BaTiO_3$)

The electrical properties of barium titanate ($BaTiO_3$, BTO)-based semiconductor material including high dielectric constant, low dielectric dissipation, ferroelectric and piezoelectric behavior have been thoroughly investigated. Additionally, the optical applications of BTO include image processing, optical signal amplification and optical data storage.[153] Among perovskite oxides and photorefractive materials, BTO is one of the most promising candidates owing to its physical properties,[154–156] strong holographic sensitivity,[157] and large electrooptic coefficients.[158] BTO has a wide range of applications in piezoelectric transducers, actuators, microwave electronics, infrared detectors, multi-layer ceramic capacitors (MLCCs), pulse generating, voltage tunable, and charge storage devices.[159–161]

6.1.2: Alloying with calcium (Ca)

$BaTiO_3$ is ferroelectric at room temperature with the space group P4mm. At the growth temperature, hexagonal BTO crystals are generated from a melt of stoichiometric composition.[162] A reconstructive phase transition to the cubic form begins at 1450 °C,[162] at which point the crystals can be damaged due to cracking. As a result, cubic BTO must be produced at temperatures below 1400 °C, from solutions with an excess of TiO_2[163] or from KF fluxes[164] which further increases the solvent inclusion probability and low growth rates.[165–167] Current advancements in high performance micro-electronics[168] demand MLCCs to increase the operating temperature range to 150° C. Studies found that substituting the Ba site in BTO with metal ions can tailor its working temperature range.[169] Furthermore, alkaline earth metal dopants are well recognized for producing a variety of physical features including ferroelectricity, structural changes, and plays a key role reducing electrical resistance[170] in BTO based semiconducting materials.

Calcium on the barium site can help prevent the formation of the undesirable hexagonal phase[171] and can lower the orthorhombic to tetragonal phase ($T_{\text{O-T}}$) transition temperature. The substitution of Ca in BTO has a considerable influence on the Curie temperature (T_{C}) and electrical characteristics.[172–174] In addition, calcium inclusion can also change the dielectric constant and introduce enhanced piezoelectric properties.[175–177]

6.2: Persistent photoconductivity (PPC) in wide bandgap semiconductors

Photoconductivity is the phenomenon in which a substance absorbs electromagnetic radiation and as a result becomes more electrically conductive. In semiconductors, this means that light exposure increases the number of free electrons or holes. This can occur if electrons are promoted from defect levels to the conduction band or if incoming light has sufficient energy to stimulate electrons across the bandgap. After the light is turned off, this effect usually fades away very quickly. PPC is light-induced conductivity that lasts for longer time scales after the termination of the excitation source.

A photo-ionized neutral donor becomes positively charged and relaxes to its new energy minimum. The sample's conductivity increases as a result of the free electron created during the process. Hence, PPC is distinguished by an increase in electrical conductivity, up to several orders of magnitude, that can persist for weeks or longer.[90,178,179] Furthermore, an increase in free carrier absorption can also be detected using infrared (IR) spectroscopy.[178]

PPC can occur at low temperatures due to deep level point defects knows as DX centers.[180] PPC has previously also been reported at room temperatures in wide bandgap semiconductors, but the increase in conductivity measured is less than an order of magnitude.[181,182] Poole et al.[179] demonstrated that PPC may be selectively induced in specific portions of a crystal, allowing for rewritable optically written circuits and holographic data storage. The electrical excitation of substitutional hydrogen (H_O) is thought to be the mechanism underpinning PPC.[92,183] Additionally, Pansegrau et al.[91] showed that when exposed to 2.9 eV photons, BTO annealed at 1200 °C in a flowing humid hydrogen environment exhibits PPC at ambient temperature which further persist over several days. The optical threshold agrees with the previously predicted 2.9 eV ionization energy of H_O^+.[183]

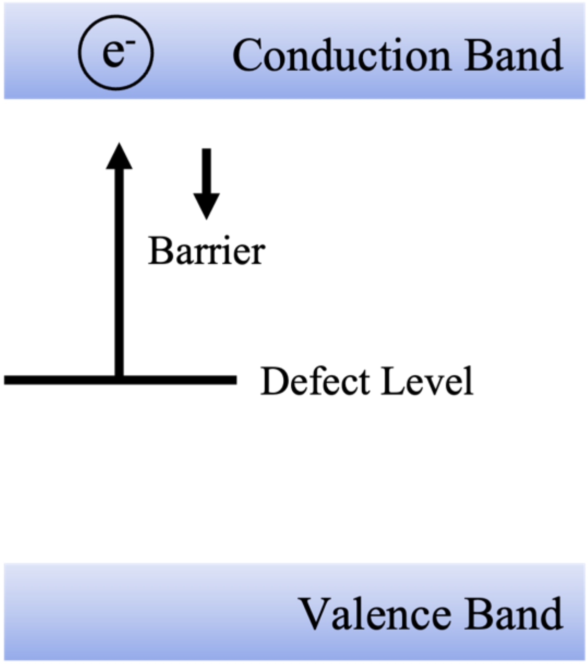

Figure 6.1: Energy diagram showing the persistent photoconductivity effect.

6.3: Barium Calcium Titanate (BCT) alloy

$Ba_{1-x}Ca_xTiO_3$ (BCT) samples were grown using Czochralski (CZ) method in an Iridium (Ir) crucible under inert atmosphere. There was little to no evaporation of the BCT during the growth. The surfaces were polished on a glass slide with Al grinding medium.

The chemical composition of the BCT crystal was investigated using energy dispersive spectroscopy (EDS). The EDS profile in Fig. 6.2 shows overlapping Ba and Ti peaks, which occurs within the energy resolution. The presence of O and Ca can also be seen in the EDS profile. The EDS spectra were analyzed by the onboard software, and just 2.88 At% Ca was found. However, this value was influenced by the inaccurate Ba and Ti concentrations. The Ca content is estimated to be about ~14.5% by

$$\frac{x}{3} = \frac{[Ca]}{[O]}$$

$$x = \frac{2.88}{59.53} \times 3 \approx 14.5\%$$

Where, [Ca] and [O] are the measured At% of Ca and O respectively. The estimates accounts for the overlapping Ba and Ti peaks by considering the O At% as a normalization constant.

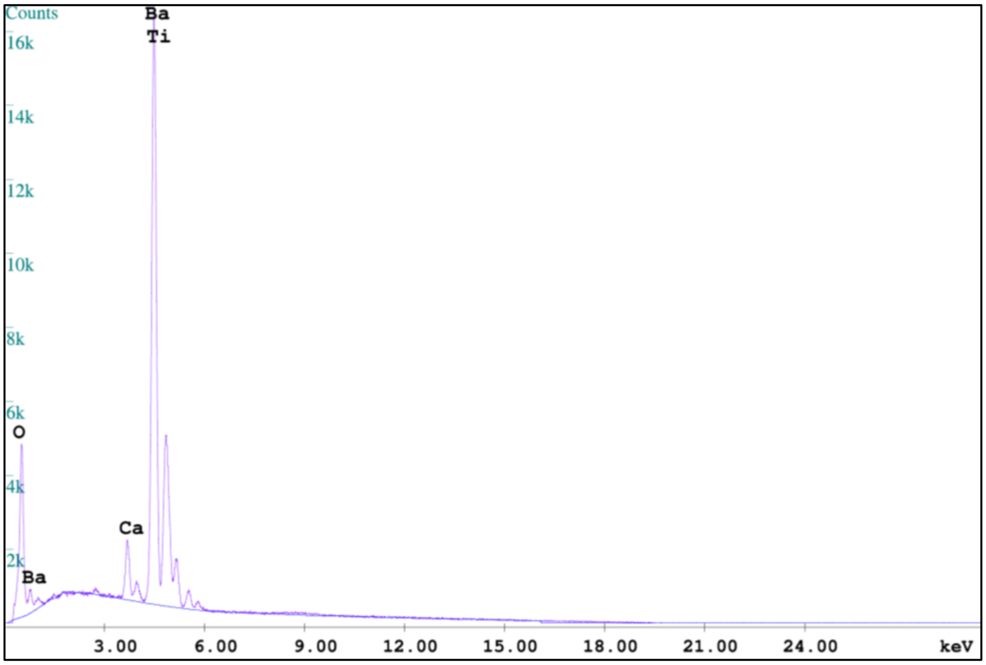

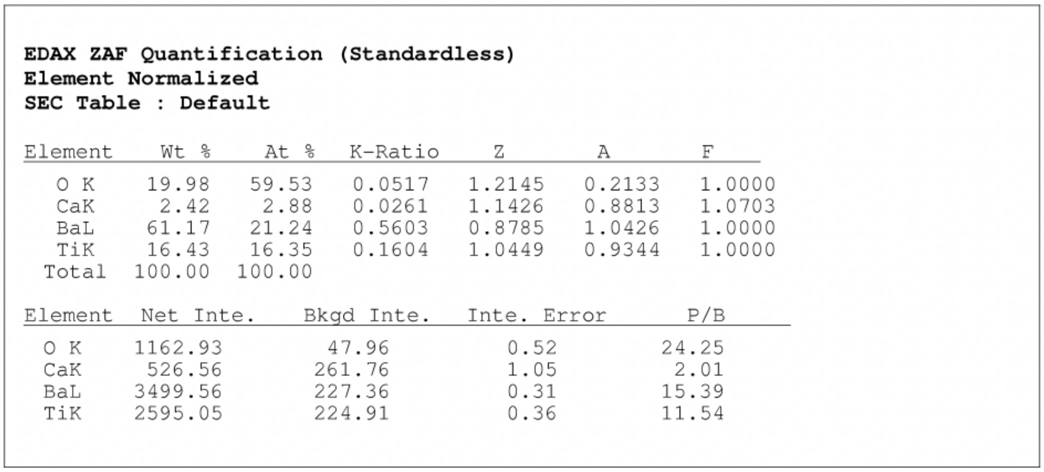

```
EDAX ZAF Quantification (Standardless)
Element Normalized
SEC Table : Default

Element    Wt %     At %   K-Ratio     Z        A        F

   O K     19.98    59.53   0.0517   1.2145   0.2133   1.0000
   CaK      2.42     2.88   0.0261   1.1426   0.8813   1.0703
   BaL     61.17    21.24   0.5603   0.8785   1.0426   1.0000
   TiK     16.43    16.35   0.1604   1.0449   0.9344   1.0000
  Total   100.00   100.00

Element  Net Inte.    Bkgd Inte.   Inte. Error      P/B

 O K     1162.93        47.96         0.52         24.25
 CaK      526.56       261.76         1.05          2.01
 BaL     3499.56       227.36         0.31         15.39
 TiK     2595.05       224.91         0.36         11.54
```

Figure 6.2: EDS spectrum and composition quantification table of $Ba_{1-x}Ca_xTiO_3$ crystal.

Figure 6.3 displays a Si peak in the EDS spectrum, which might be the result of an inclusion picked up during polishing BCT on a Si glass slide. Only one of these inclusions was detected; the remainder of the surface was polished and uniform.

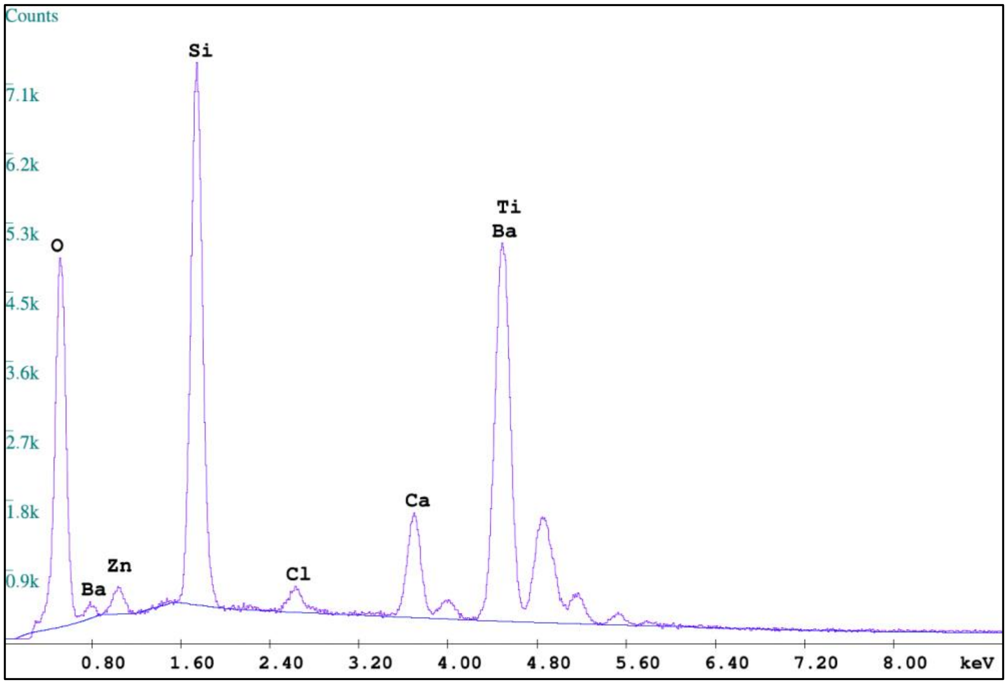

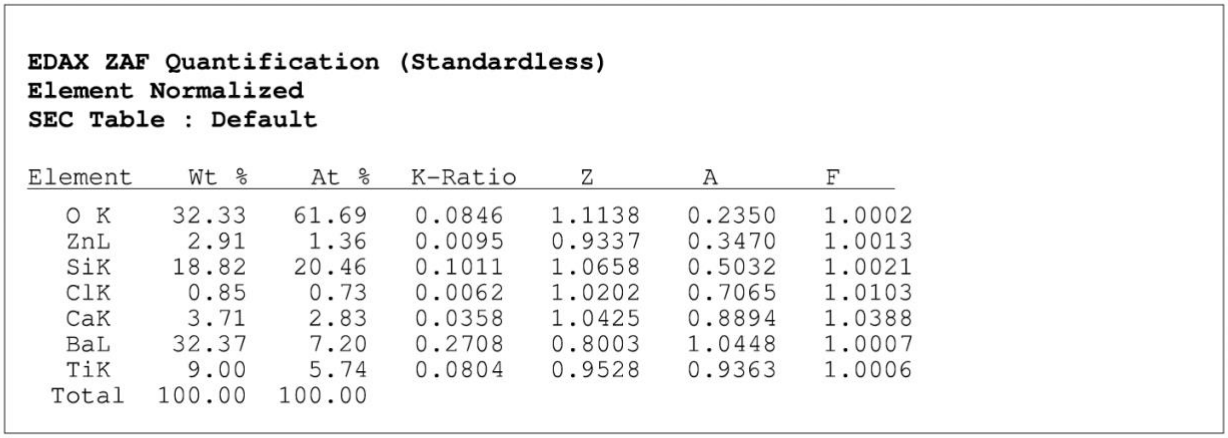

```
EDAX ZAF Quantification (Standardless)
Element Normalized
SEC Table : Default

Element    Wt %     At %    K-Ratio     Z         A         F
   O K     32.33    61.69   0.0846    1.1138    0.2350    1.0002
   ZnL      2.91     1.36   0.0095    0.9337    0.3470    1.0013
   SiK     18.82    20.46   0.1011    1.0658    0.5032    1.0021
   ClK      0.85     0.73   0.0062    1.0202    0.7065    1.0103
   CaK      3.71     2.83   0.0358    1.0425    0.8894    1.0388
   BaL     32.37     7.20   0.2708    0.8003    1.0448    1.0007
   TiK      9.00     5.74   0.0804    0.9528    0.9363    1.0006
  Total   100.00   100.00
```

Figure 6.3: EDS spectrum and composition quantification table of $Ba_{1-x}Ca_xTiO_3$ crystal with Si inclusion.

Raman measurements were carried out using a Klar Mini Pro microscope on an MTI supplied one sided polished, 10 ×10 × 0.5 mm, (100) orientated single crystal $BaTiO_3$ (BTO) and crystal along with BCT crystal at room temperatures. The BTO crystal was grown using the top-seeded solution process. The microscope used was equipped with a fiber-coupled 532 nm CW laser and an Ocean Insight QE Pro spectrometer. The laser power was set to 20 mW at the sample. The microscope laser did not generate any phase changes, despite its comparatively high laser power density. The integration time was set to 8 s with a detected spectral region of 100 – 4000 cm^{-1}.

The Raman peaks of BTO crystal are located at 175, 275, 525, and 723 cm^{-1} as illustrated in Fig. 6.4.[184] BCT has peaks around 150 cm^{-1} and 250 cm^{-1} which are ~25 cm^{-1} lower than the corresponding BTO modes.[184] However, the peak near 524 cm^{-1} is nearly identical to that in BTO. The peak around 725 cm^{-1} is unique to BCT in the tetragonal phase.[185] The sharp 133 cm^{-1} peak is due to the breaking of selection rules caused by Ca disorder in the $BaTiO_3$ lattice.[184] Since Ca does not exactly substitute for Ba ions, a small displacement of Ca ions about the Ba site is responsible for the stronger 133 cm^{-1} peak in BTO.

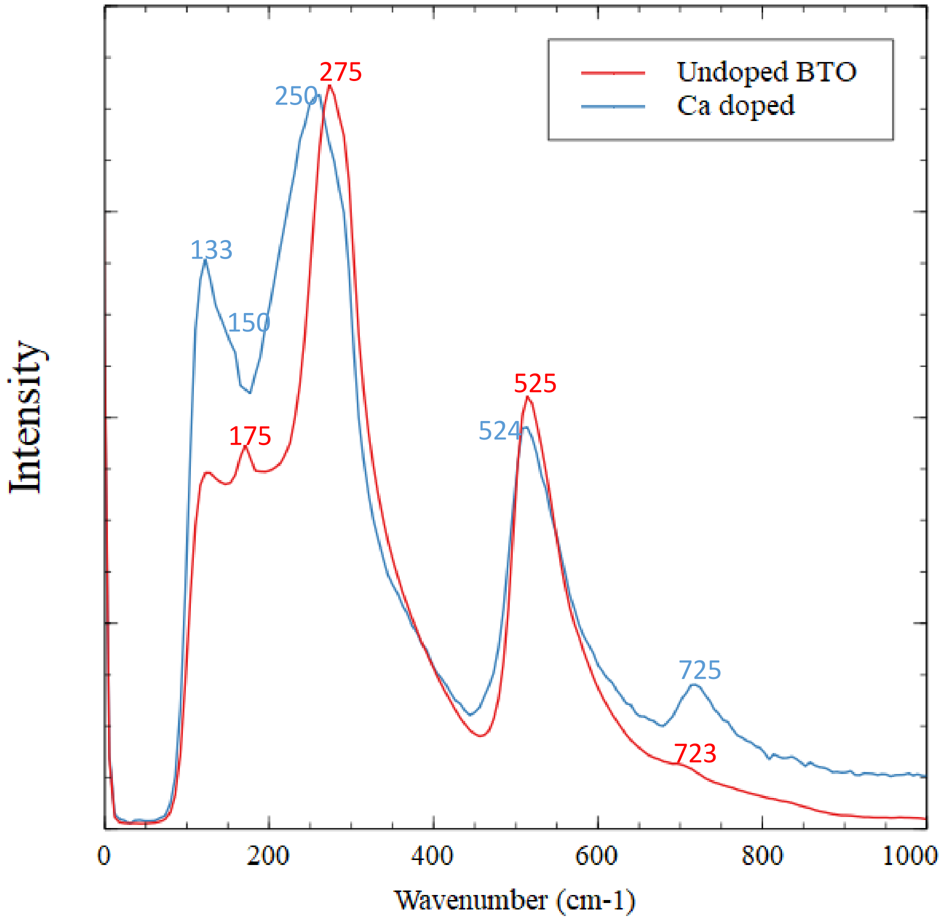

Figure 6.4: Raman spectra of $BaTiO_3$ (BTO) and Ca alloyed $BaTiO_3$ (BCT).

Inside a horizontal tube furnace, BCT samples were annealed under a flowing gas mixture of humid argon and 98% argon + 2% hydrogen gas. The humid argon was created by blowing ultra-high purity argon in high-performance liquid chromatography (HPLC) grade water. After the bubbler, the two gas sources were combined, and the relative humidity was measured and maintained at around 40% throughout the annealing process.

Bulk BCT crystals were annealed inside a sealed fused silica tube. Before switching on the furnace, the annealing chamber was purged for 30 minutes with a hydrogen-argon gas mixture at a rate of 2.0 standard cubic feet per hour (scf/h). Purging reduces any remaining ambient gases that may be trapped within the sealed chamber. The furnace was turned on after the purge and the sample was annealed for 1 hour at 1200 °C with a temperature ramp rate of 550 °C/h. After the anneal, the complete gas tube assembly was transported outside of the furnace to a point so that the region containing the sample can undergo rapid cooling under dark. The gas continued to flow for another hour, which further assist in cooling.

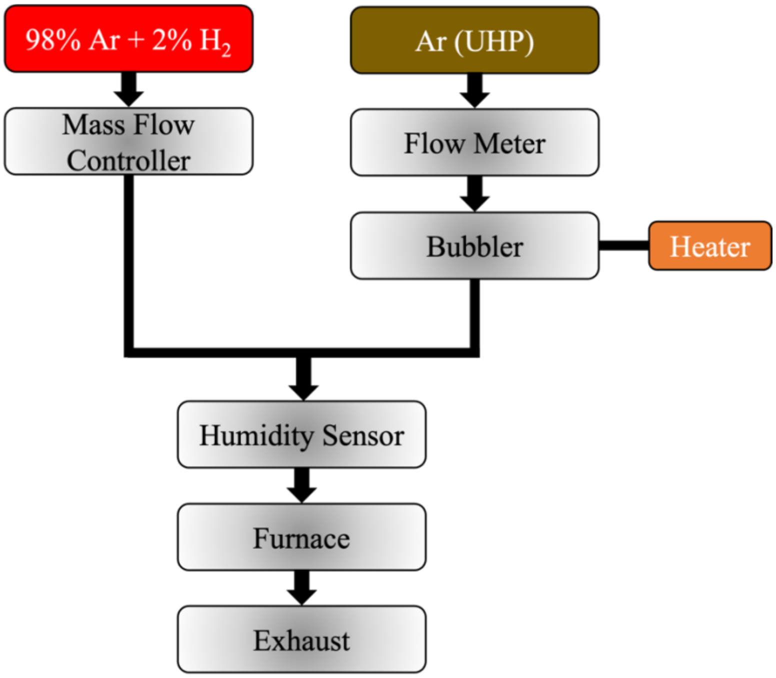

Figure 6.5: Schematic diagram of the BCT annealing process.

6.4: Room temperature persistent photoconductivity (PPC) in BCT

6.4.1: Photo-induced onset of PPC

Electrical measurements may be used to directly examine the change in conductivity; however, this is not the only method. An increase or reduction in the optical absorption in the IR region of the spectrum correlates to a change in the free carrier absorption.[186] In BCT, we analyzed PPC using change in absorbance in the IR spectra; a decrease in transmitted IR intensity correlates to an increase in free carrier absorption.

A Bomem DA8 Fourier transform infrared (FTIR) spectrometer was used to acquire IR spectra. A SiC source, InSb detector, and KBr beam splitter were used to obtain spectra in a region 1800 – 6000 cm^{-1} at room temperature. In order to illuminate the BCT crystal during spectrum collection, a light emitting diode (LED) was installed in the sample chamber. Spectra were captured with the light on and off in an alternating pattern, with LEDs employed in order of increasing photon energy. The LED light intensity was controlled by setting the current provided to ~0.8 A for all of them.

Figure 6.6 shows the IR transmission intensity of BCT after LED exposure ranging from 1.98 eV to 3.06 eV. The unexposed crystal is represented by the dotted black spectrum. The IR transmission intensity decreased significantly after the sample was exposed to higher-energy LEDs with a threshold of 2.72 eV (455 nm).

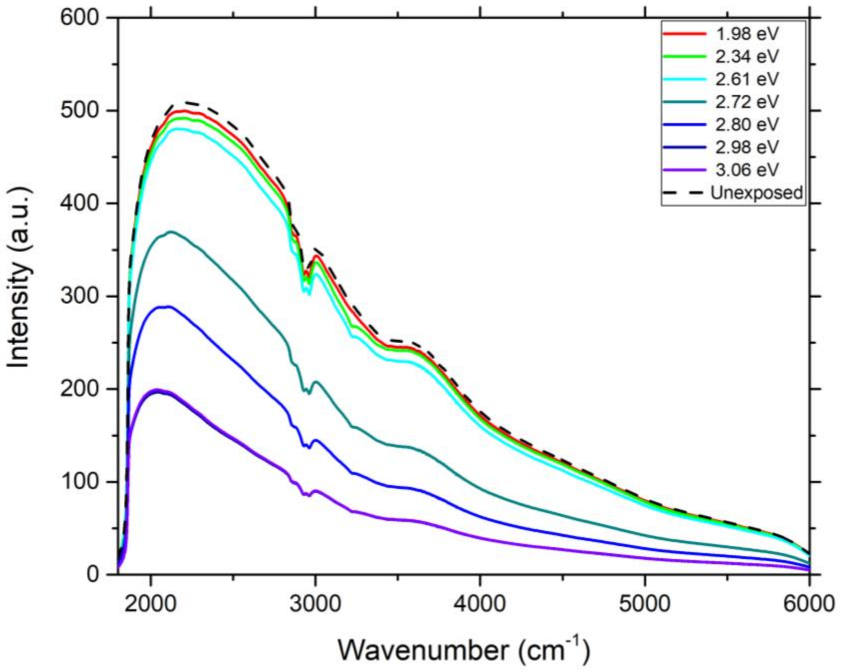

Figure 6.6: IR transmission spectra with InSb detector of BCT crystal. The significant amplitude reduction in intensity following light exposure with a 3.06 eV LED with a threshold of 2.72 eV demonstrates PPC.

Figure 6.7 depicts the change in IR absorbance after LED exposure. To compute the change in absorbance, the post-LED treated spectra were compared to the original spectrum recorded before any light exposure. Photons with energy below 2.72 eV had no discernible effect. However, illuminating photons with an energy starting at 2.72 eV up to 3.06 eV generated a considerable and broad increase in absorbance. This effect can be related to an increase in free-carrier density generated by photons with energies ≥ 2.72 eV. The peak around 3220 cm^{-1} is tentatively assigned to an O–H stretching vibration.

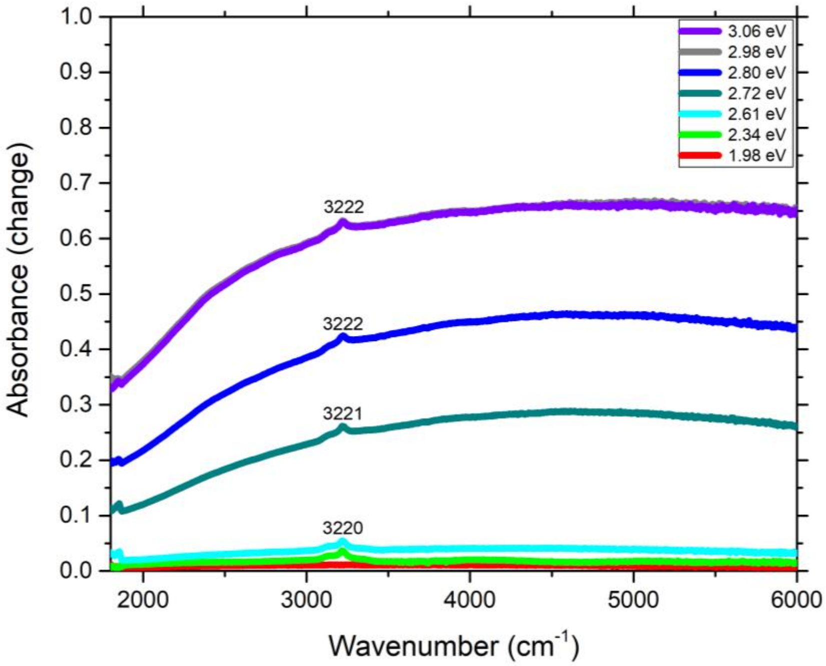

Figure 6.7: Room temperature IR absorbance spectra of a BCT crystal annealed under flowing 2 scf/h H_2. After annealing, the unexposed spectrum was used to establish a baseline. The sample was then exposed to LEDs of increasing photon energy.

6.4.2: PPC lifetime

The change in IR transmission spectra after 3.06 eV LED exposure is seen in Fig. 6.8. The spectra were taken in 24-hour increments for a total of 168 hours. The data suggest that the transmission intensity begins to increase slowly after LED treatment.

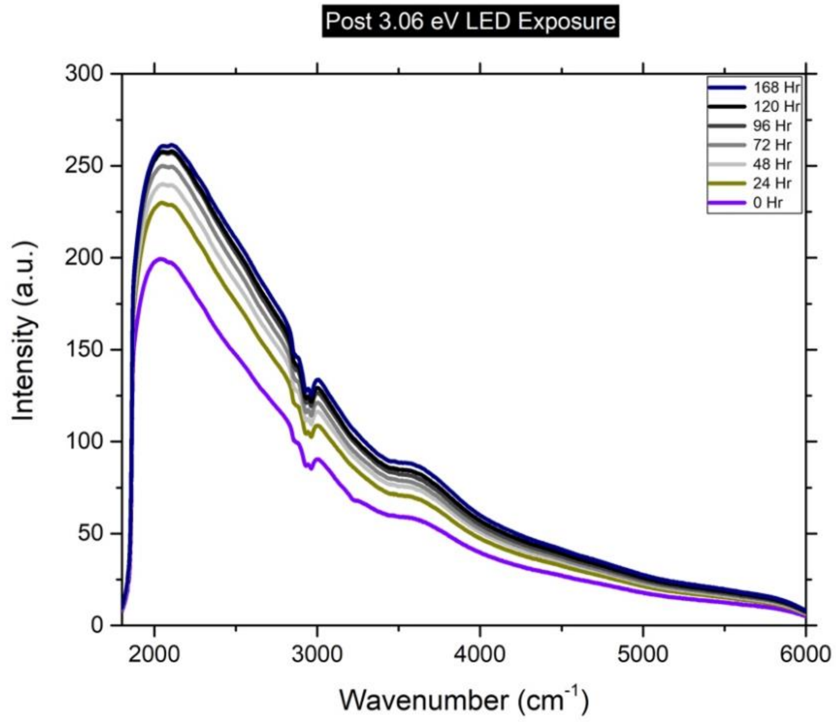

Figure 6.8: FTIR transmission spectra after 3.06 eV LED exposure.

The IR absorbance change was observed for seven days to assess the duration of PPC effect post 3.06 eV LED illumination (Fig. 6.9). The sample was screened from visible and UV radiation throughout this period. The spectra were compared to a baseline unexposed spectrum. The results indicates that the photo-induced change in absorbance is long-lasting. The first 24 hours post LED treatment saw the most significant drop in absorbance. The absorbance change beyond the initial 48 hours mark was minimal. The peak at 3220 wavenumbers was gone 24 hours after illumination.

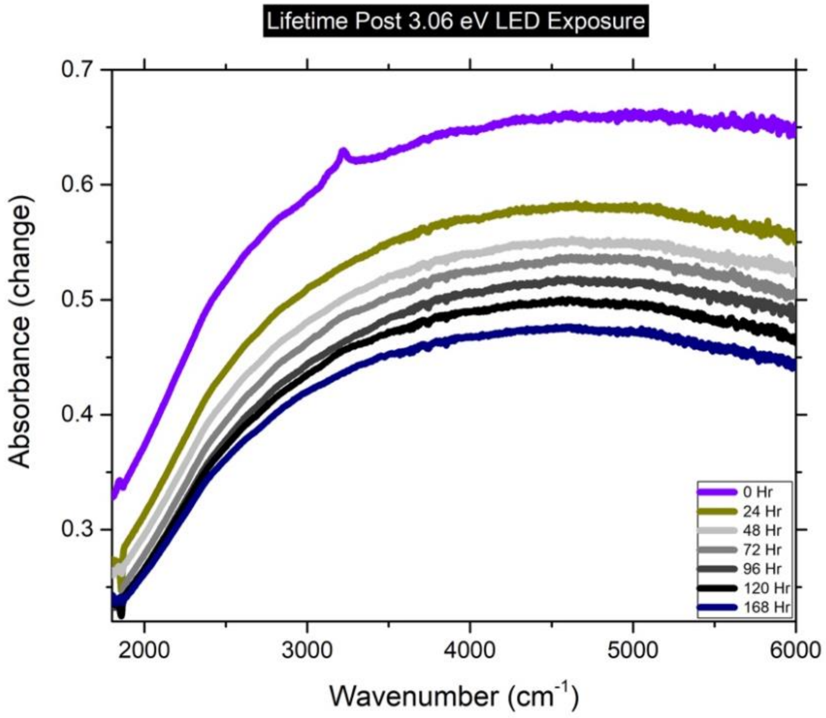

Figure 6.9: Change in IR absorbance spectra after 3.06 eV LED exposure.

6.4.3: PPC reset

The PPC effect can be reset by heating the crystal to 400 °C for 30 minutes under ambient conditions. This effectively restores the sample's pre-LED exposure state. Fig. 6.10 shows that there is a significant decrease in IR transmission spectra post LED treatment. Heating the sample on a hot plate, on the other hand, returns the sample's transmission to near-pre-light exposure levels, suggesting that the photo-induced PPC effect may be erased.

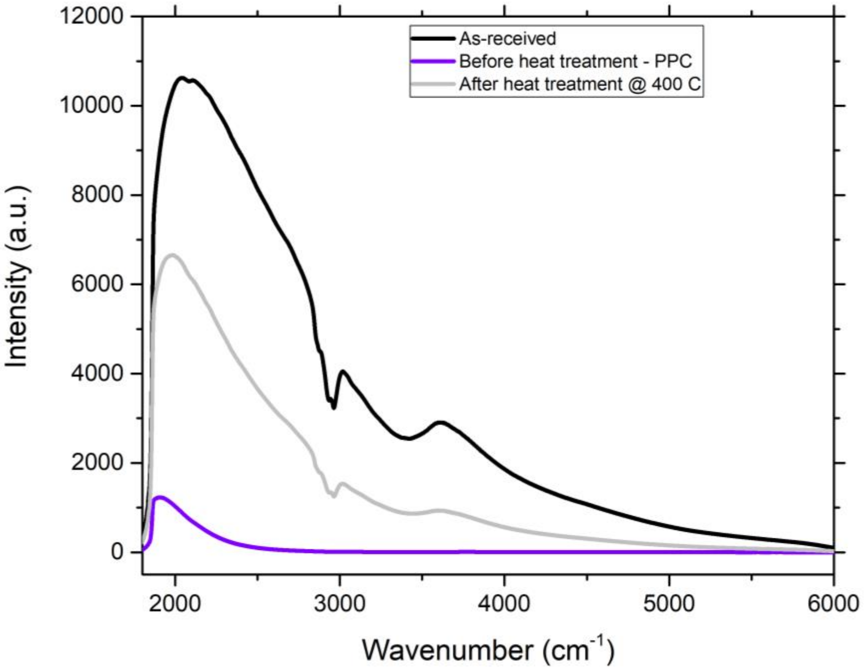

Figure 6.10: Change in IR transmission spectra after hot plate treatment for 30 minutes at 400 °C.

Figure 6.11 shows that the induced PPC effect resets following the hot plate treatment, indicating that the BCT crystals can be restored to its initial state and reused.

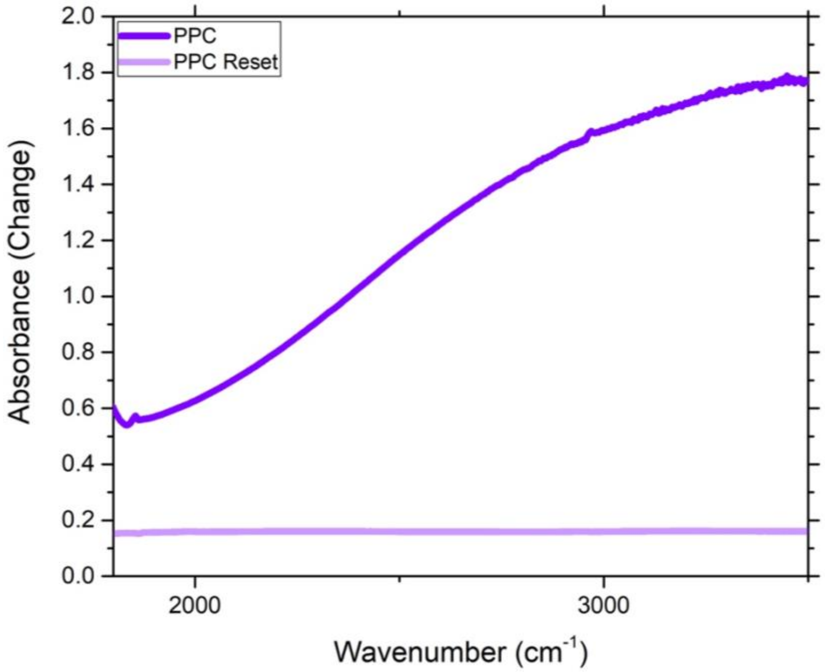

Figure 6.11: The absorbance spectra changed after a 30-minute hot plate treatment at 400 °C, suggesting that the BCT crystal was reset to its pre-annealing state.

6.5: Electrical measurements

Semiconductors' electrical characteristics are critical for their application in electronic devices. For example, one must know the material's resistance in order to select the appropriate current for the device to work at the specified voltage. The net doping concentration can also be determined using conductivity and mobility tests. Furthermore, to create fundamental semiconductor circuit elements like a p-n junction, it is necessary to know if the carriers are electrons or holes.

Parallel to the post-exposure lifetime test, two-point electrical measurements with pressed indium contacts were carried out. Prior to light exposure, the initial resistance was measured to be ~14 KΩ. The measured resistance reduced to around 9.9 KΩ after exposure to 3.06 eV light, as seen in Fig. 6.12. During the next 24 hours, this value increased to ~10.2 KΩ and did not change much thereafter for up to 7 days.

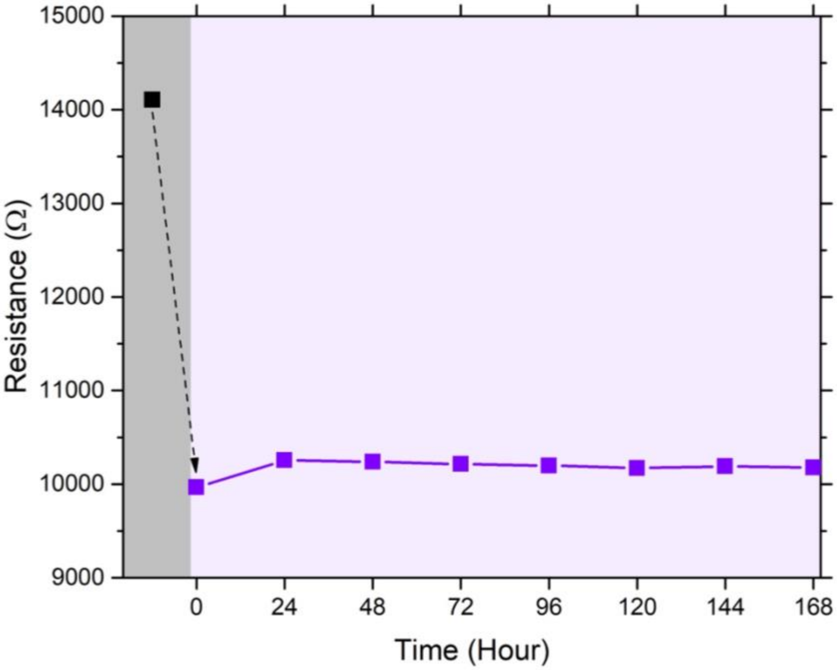

Figure 6.12: Two-point electrical measurements of annealed BCT crystal fitted with pressed indium contacts. The grey zone represent resistance before light exposure. The violet zone corresponds to the resistance change post 3.06 eV (405 nm) LED exposure measured every 24 hours up to 7 days.

As-received samples have a very high resistance of roughly ~10^{10} Ω. The material was too resistive to get reliable Hall measurements at room temperature. However, resistivities in the hydrogenated sample range from 1-6 Ω cm. PPC results in a minor change in electrical properties based on the Hall measurements. The change in resistivity, density, and mobility values that accompany PPC after 3.06 eV LED exposure is shown in Table 6.1. There is minimal change in resistivity, which contradicts the large increase seen in free carrier absorption in the IR spectra upon illumination.

Exposure State	Resistivity (Ω cm)	Density (cm^{-3})	Mobility (cm^2/Vs)	Carrier Type
Before exposure	6.2612	2.0681×10^{17}	0.26126	Holes
Post 3.06 eV LED exposure	6.2661	-5.6561×10^{16}	-2.170	Electrons

Table 6.1: Hall effect measurements before and after LED exposure.

6.6: Summary

In conclusion, when exposed to 2.72 eV photons, BCT annealed at 1200 °C in a flowing humid 2% hydrogen environment shows PPC at ambient temperatures along with a subtle change in conductivity. The optical threshold is in close match with BTO crystal 2.9 eV PPC optical threshold energy[91] and predicted 2.9 eV ionization energy for H_O^+ .[183] The observed findings are substantially influenced by the presence of hydrogen in the annealing environment, implying that the PPC mechanism is comparable to that of BTO.[91] Furthermore, BCT was returned to its pre-exposure state by simply annealing it on a hot plate under ambient conditions, indicating that the process is reversible.

REFERENCES

[1] J.A. Fleming, US803684A (7 November 1905).

[2] L.D. Forest, Trans. Am. Inst. Electr. Eng. **XXV**, 735 (1906).

[3] J. Bardeen and W.H. Brattain, Phys. Rev. **74**, 230 (1948).

[4] M. Riordan, L. Hoddeson, and C. Herring, in *More Things Heaven Earth Celebr. Phys. Millenn.*, edited by B. Bederson (Springer, New York, NY, 1999), pp. 563–578.

[5] S. William, US2569347A (25 September 1951).

[6] T.H. Lee, *The Design of CMOS Radio-Frequency Integrated Circuits* (Cambridge University Press, 2003).

[7] X. Yu, T.J. Marks, and A. Facchetti, Nat. Mater. **15**, 383 (2016).

[8] K. Ellmer, Nat. Photonics **6**, 809 (2012).

[9] S. C. Dixon, D. O. Scanlon, C. J. Carmalt, and I. P. Parkin, J. Mater. Chem. C **4**, 6946 (2016).

[10] J.F. Wager, Science **300**, 1245 (2003).

[11] J.F. Wager, D.A. Keszler, and R.E. Presley, *Transparent Electronics* (Springer, 2008).

[12] L.L. Liu, M.K. Li, D.Q. Yu, J. Zhang, H. Zhang, C. Qian, and Z. Yang, Appl. Phys. A **98**, 831 (2010).

[13] J.F. Wager and R. Hoffman, IEEE Spectr. **48**, 42 (2011).

[14] K. Nomura, H. Ohta, K. Ueda, T. Kamiya, M. Hirano, and H. Hosono, Science **300**, 1269 (2003).

[15] K. Nomura, H. Ohta, A. Takagi, T. Kamiya, M. Hirano, and H. Hosono, Nature **432**, 488 (2004).

[16] H. Yabuta, M. Sano, K. Abe, T. Aiba, T. Den, H. Kumomi, K. Nomura, T. Kamiya, and H. Hosono, Appl. Phys. Lett. **89**, 112123 (2006).

[17] T. Hirao, M. Furuta, T. Hiramatsu, T. Matsuda, C. Li, H. Furuta, H. Hokari, M. Yoshida, H. Ishii, and M. Kakegawa, IEEE Trans. Electron Devices **55**, 3136 (2008).

[18] J. Lee, D. Kim, D. Yang, S. Hong, K. Yoon, P. Hong, C. Jeong, H.-S. Park, S.Y. Kim, S.K. Lim, S.S. Kim, K. Son, T. Kim, J. Kwon, and S. Lee, SID Symp. Dig. Tech. Pap. **39**, 625 (2008).

[19] J.K. Jeong, J.H. Jeong, J.H. Choi, J.S. Im, S.H. Kim, H.W. Yang, K.N. Kang, K.S. Kim, T.K. Ahn, H.-J. Chung, M. Kim, B.S. Gu, J.-S. Park, Y.-G. Mo, H.D. Kim, and H.K. Chung, SID Symp. Dig. Tech. Pap. **39**, 1 (2008).

[20] R. Martins, I. Ferreira, and E. Fortunato, Phys. Status Solidi RRL – Rapid Res. Lett. **5**, 332 (2011).

[21] D. Tobjörk and R. Österbacka, Adv. Mater. **23**, 1935 (2011).

[22] M. Kimura, Jpn. J. Appl. Phys. **58**, 090503 (2019).

[23] O. Carp, C.L. Huisman, and A. Reller, Prog. Solid State Chem. **32**, 33 (2004).

[24] X.-Q. Gong and A. Selloni, J. Phys. Chem. B **109**, 19560 (2005).

[25] X.-Q. Gong, A. Selloni, and A. Vittadini, J. Phys. Chem. B **110**, 2804 (2006).

[26] M. Lazzeri and A. Selloni, Phys. Rev. Lett. **87**, 266105 (2001).

[27] M. Lazzeri, A. Vittadini, and A. Selloni, Phys. Rev. B **63**, 155409 (2001).

[28] A. Vittadini, A. Selloni, F.P. Rotzinger, and M. Grätzel, Phys. Rev. Lett. **81**, 2954 (1998).

[29] A. Vittadini, M. Casarin, and A. Selloni, Theor. Chem. Acc. **117**, 663 (2007).

[30] L. Forro, O. Chauvet, D. Emin, L. Zuppiroli, H. Berger, and F. Lévy, J. Appl. Phys. **75**, 633 (1994).

[31] A. Janotti, J.B. Varley, P. Rinke, N. Umezawa, G. Kresse, and C.G. Van de Walle, Phys. Rev. B **81**, 085212 (2010).

[32] M. Setvin, C. Franchini, X. Hao, M. Schmid, A. Janotti, M. Kaltak, C.G. Van de Walle, G. Kresse, and U. Diebold, Phys. Rev. Lett. **113**, 086402 (2014).

[33] K. Tennakone, G.R.R.A. Kumara, I.R.M. Kottegoda, V.P.S. Perera, and P.S.R.S. Weerasundara, J. Photochem. Photobiol. Chem. **117**, 137 (1998).

[34] H. Long, A. Chen, G. Yang, Y. Li, and P. Lu, Thin Solid Films **517**, 5601 (2009).

[35] N. Golego, S.A. Studenikin, and M. Cocivera, J. Electrochem. Soc. **147**, 1592 (2000).

[36] K. Page, R. G. Palgrave, I. P. Parkin, M. Wilson, S.L. P. Savin, and A. V. Chadwick, J. Mater. Chem. **17**, 95 (2007).

[37] Q. Li, S. Mahendra, D.Y. Lyon, L. Brunet, M.V. Liga, D. Li, and P.J.J. Alvarez, Water Res. **42**, 4591 (2008).

[38] M. Wagemaker, W.J.H. Borghols, and F.M. Mulder, J. Am. Chem. Soc. **129**, 4323 (2007).

[39] D. Deng, M.G. Kim, J.Y. Lee, and J. Cho, Energy Environ. Sci. **2**, 818 (2009).

[40] C.G. Kuo, C.Y. Hsu, S.S. Wang, and D.C. Wen, Appl. Surf. Sci. **258**, 6952 (2012).

[41] B. O'Regan and M. Grätzel, Nature **353**, 737 (1991).

[42] A. Fujishima and K. Honda, Nature **238**, 37 (1972).

[43] A.L. Linsebigler, G. Lu, and J.T. Yates, Chem. Rev. **95**, 735 (1995).

[44] X. Chen and S.S. Mao, Chem. Rev. **107**, 2891 (2007).

[45] P. Kondaiah, M.C. Sekhar, S.V.J. Chandra, R. Martins, S. Uthanna, and E. Elangovan, IOP Conf. Ser. Mater. Sci. Eng. **30**, 012005 (2012).

[46] H. Poelman, D. Poelman, D. Depla, H. Tomaszewski, L. Fiermans, and R. De Gryse, Surf. Sci. **482–485**, 940 (2001).

[47] G.D. Wilk, R.M. Wallace, and J.M. Anthony, J. Appl. Phys. **89**, 5243 (2001).

[48] A. Fujishima, Jpn. Nanonet Bull. **44**, 1 (2005).

[49] L. Chu, Z. Qin, J. Yang, and X. Li, Sci. Rep. **5**, 12143 (2015).

[50] J. Li and D. Xu, Chem. Commun. **46**, 2301 (2010).

[51] G. Mogilevsky, Q. Chen, A. Kleinhammes, and Y. Wu, Chem. Phys. Lett. **460**, 517 (2008).

[52] D.A.H. Hanaor and C.C. Sorrell, Adv. Eng. Mater. **16**, 248 (2014).

[53] K. Okada, N. Yamamoto, Y. Kameshima, A. Yasumori, and K.J.D. MacKenzie, J. Am. Ceram. Soc. **84**, 1591 (2001).

[54] H. Shin, H.S. Jung, K.S. Hong, and J.-K. Lee, J. Solid State Chem. **178**, 15 (2005).

[55] A. Matthews, Am. Mineral. **61**, 419 (1976).

[56] R.L. Penn and J.F. Banfield, Am. Mineral. **84**, 871 (1999).

[57] R.D. Shannon and J.A. Pask, J. Am. Ceram. Soc. **48**, 391 (1965).

[58] J.C. Jamieson and B. Olinger, Am. Mineral. **54**, 1477 (1969).

[59] C.N.R. Rao, Can. J. Chem. **39**, 498 (1961).

[60] M. Batzill, E.H. Morales, and U. Diebold, Phys. Rev. Lett. **96**, 026103 (2006).

[61] G.H. Lee and J.-M. Zuo, J. Am. Ceram. Soc. **87**, 473 (2004).

[62] S. Riyas, G. Krishnan, and P.N.M. Das, Adv. Appl. Ceram. **106**, 255 (2007).

[63] E.F. Heald and C.W. Weiss, Am. Mineral. **57**, 10 (1972).

[64] F.C. Gennari and D.M. Pasquevich, J. Mater. Sci. **33**, 1571 (1998).

[65] S.J. Smith, R. Stevens, S. Liu, G. Li, A. Navrotsky, J. Boerio-Goates, and B.F. Woodfield, Am. Mineral. **94**, 236 (2009).

[66] J. Muscat, V. Swamy, and N.M. Harrison, Phys. Rev. B **65**, 224112 (2002).

[67] Y. Zhang, in *Geochemistry* (Springer Netherlands, Dordrecht, 1998), pp. 120–123.

[68] A. NAVROTSKY and O.J. KLEPPA, J. Am. Ceram. Soc. **50**, 626 (1967).

[69] T. Mitsuhashi and O.J. Kleppa, J. Am. Ceram. Soc. **62**, 356 (1979).

[70] F.D. Rossini, (1972).

[71] J. Zhang, P. Zhou, J. Liu, and J. Yu, Phys. Chem. Chem. Phys. **16**, 20382 (2014).

[72] T. Luttrell, S. Halpegamage, J. Tao, A. Kramer, E. Sutter, and M. Batzill, Sci. Rep. **4**, 4043 (2014).

[73] P. Kar, S. Zeng, Y. Zhang, E. Vahidzadeh, A. Manuel, R. Kisslinger, K.M. Alam, U.K. Thakur, N. Mahdi, P. Kumar, and K. Shankar, Appl. Catal. B Environ. **243**, 522 (2019).

[74] S. Mereym, S. Nasreen, M. Siddique, and R. Khan, Rev. Chem. Eng. **34**, (2017).

[75] A.C.M. Padilha, H. Raebiger, A.R. Rocha, and G.M. Dalpian, Sci. Rep. **6**, 28871 (2016).

[76] J. Li, R. Lazzari, S. Chenot, and J. Jupille, Phys. Rev. B **97**, 041403 (2018).

[77] X. Pan, M.-Q. Yang, X. Fu, N. Zhang, and Y.-J. Xu, Nanoscale **5**, 3601 (2013).

[78] L.-B. Xiong, J.-L. Li, B. Yang, and Y. Yu, J. Nanomater. **2012**, (2011).

[79] T. Bak, D. Chu, A.R. Francis, W. Li, and J. Nowotny, Catal. Today **224**, 200 (2014).

[80] J. Nowotny, M. Abdul Alim, T. Bak, M. Asri Idris, M. Ionescu, K. Prince, M. Zainizan Sahdan, K. Sopian, M.A.M. Teridi, and W. Sigmund, Chem. Soc. Rev. **44**, 8424 (2015).

[81] J. Strunk, W.C. Vining, and A.T. Bell, J. Phys. Chem. C **114**, 16937 (2010).

[82] J.F. Ihlefeld, D.T. Harris, R. Keech, J.L. Jones, J.-P. Maria, and S. Trolier-McKinstry, J. Am. Ceram. Soc. **99**, 2537 (2016).

[83] G.L. Brennecka, J.F. Ihlefeld, J.-P. Maria, B.A. Tuttle, and P.G. Clem, J. Am. Ceram. Soc. **93**, 3935 (2010).

[84] Sonia, R.K. Patel, P. Kumar, C. Prakash, and D.K. Agrawal, Ceram. Int. **38**, 1585 (2012).

[85] E.A. Stern, Phys. Rev. Lett. **93**, 037601 (2004).

[86] R.E. Cohen, Nature **358**, 136 (1992).

[87] T.R. Shrout and S.J. Zhang, J. Electroceramics **19**, 113 (2007).

[88] C. Kuper, R. Pankrath, and H. Hesse, Appl. Phys. A **65**, 301 (1997).

[89] H. Veenhuis, T. Börger, K. Peithmann, M. Flaspöhler, K. Buse, R. Pankrath, H. Hesse, and E. Krätzig, Appl. Phys. B **70**, 797 (2000).

[90] M.C. Tarun, F.A. Selim, and M.D. McCluskey, Phys. Rev. Lett. **111**, 187403 (2013).

[91] C. Pansegrau and M.D. McCluskey, J. Appl. Phys. **131**, 095701 (2022).

[92] V.M. Poole, J. Huso, and M.D. McCluskey, J. Appl. Phys. **123**, 161545 (2018).

[93] C.V. Raman and K.S. Krishnan, Nature **121**, 501 (1928).

[94] I.R. Lewis and H. Edwards, *Handbook of Raman Spectroscopy: From the Research Laboratory to the Process Line* (CRC Press, 2001).

[95] V. Balan, C.-T. Mihai, F.-D. Cojocaru, C.-M. Uritu, G. Dodi, D. Botezat, and I. Gardikiotis, Materials **12**, 2884 (2019).

[96] M.D. McCluskey and E.E. Haller, *Dopants and Defects in Semiconductors* (CRC Press, 2018).

[97] A. Jilani, M.S. Abdel-wahab, and A. HosnyHammad, *Advance Deposition Techniques for Thin Film and Coating* (IntechOpen, 2017).

[98]*Handbook of Thin Film Deposition Techniques Principles, Methods, Equipment and Applications, Second Editon* (CRC Press, 2002).

[99] P.M. Martin, editor, in *Handb. Depos. Technol. Films Coat. Third Ed.* (William Andrew Publishing, Boston, 2010), pp. 297–313.

[100] D.B. Chrisey and G.K. Hubler, editors, *Pulsed Laser Deposition of Thin Films* (J. Wiley, New York, 1994).

[101] F.C. Frank, Discuss. Faraday Soc. **5**, 48 (1949).

[102] D. Wicaksana, A. Kobayashi, and A. Kinbara, J. Vac. Sci. Technol. A **10**, 1479 (1992).

[103] M.D. Wiggins, M.C. Nelson, and C.R. Aita, J. Vac. Sci. Technol. A **14**, 772 (1996).

[104] K.N. Rao, M.A. Murthy, and S. Mohan, Thin Solid Films **176**, 181 (1989).

[105] Hae-Yong Lee and Ho-Gin Kim, Thin Solid Films **229**, 187 (1993).

[106] G.A. Battiston, R. Gerbasi, M. Porchia, and A. Marigo, Thin Solid Films **239**, 186 (1994).

[107] L.M. Williams and D.W. Hess, J. Vac. Sci. Technol. A **1**, 1810 (1983).

[108] A. Ranjitha, N. Muthukumarasamy, M. Thambidurai, R. Balasundaraprabhu, and S. Agilan, Optik **124**, 6201 (2013).

[109] J. Ion, *Laser Processing of Engineering Materials* (Elsevier, 2005).

[110] P.B. Nair, V.B. Justinvictor, G.P. Daniel, K. Joy, V. Ramakrishnan, and P.V. Thomas, Appl. Surf. Sci. **257**, 10869 (2011).

[111] G. Mattioli, P. Alippi, F. Filippone, R. Caminiti, and A. Amore Bonapasta, J. Phys. Chem. C **114**, 21694 (2010).

[112] P. Deák, B. Aradi, and T. Frauenheim, Phys. Rev. B **86**, 195206 (2012).

[113] I. Justicia, P. Ordejón, G. Canto, J.L. Mozos, J. Fraxedas, G.A. Battiston, R. Gerbasi, and A. Figueras, Adv. Mater. **14**, 1399 (2002).

[114] D.C. Cronemeyer, Phys. Rev. **87**, 876 (1952).

[115] A. Taherniya and D. Raoufi, Semicond. Sci. Technol. **31**, 125012 (2016).

[116] M. Landmann, E. Rauls, and W.G. Schmidt, J. Phys. Condens. Matter **24**, 195503 (2012).

[117] R. Swanepoel, J. Phys. [E] **16**, 1214 (1983).

[118] S.H. Mohamed, O. Kappertz, T.P.L. Pedersen, R. Drese, and M. Wuttig, Phys. Status Solidi A **198**, 224 (2003).

[119] H.C. Choi, Y.M. Jung, and S.B. Kim, Vib. Spectrosc. **37**, 33 (2005).

[120] V. Swamy, A. Kuznetsov, L.S. Dubrovinsky, R.A. Caruso, D.G. Shchukin, and B.C. Muddle, Phys. Rev. B **71**, 184302 (2005).

[121] C. Pighini, D. Aymes, N. Millot, and L. Saviot*, J. Nanoparticle Res. **9**, 309 (2007).

[122] J.-G. Li, T. Ishigaki, and X. Sun, J. Phys. Chem. C **111**, 4969 (2007).

[123] N. Khatun, S. Tiwari, C.P. Vinod, C.-M. Tseng, S. Wei Liu, S. Biring, and S. Sen, J. Appl. Phys. **123**, 245702 (2018).

[124] W.-J. Yin, B. Wen, C. Zhou, A. Selloni, and L.-M. Liu, Surf. Sci. Rep. **73**, 58 (2018).

[125] D.C. Hurum, A.G. Agrios, K.A. Gray, T. Rajh, and M.C. Thurnauer, J. Phys. Chem. B **107**, 4545 (2003).

[126] D. Padayachee, A.S. Mahomed, S. Singh, and H.B. Friedrich, ACS Catal. **10**, 2211 (2020).

[127] G. Li, C.P. Richter, R.L. Milot, L. Cai, C.A. Schmuttenmaer, R.H. Crabtree, G.W. Brudvig, and V.S. Batista, Dalton Trans. 10078 (2009).

[128] L.K. Gaur, P. Kumar, D. Kushavah, K.R. Khiangte, M.C. Mathpal, V. Agrahari, S.P. Gairola, M.A.G. Soler, H.C. Swart, and A. Agarwal, J. Alloys Compd. **780**, 25 (2019).

[129] F. Tian, Y. Zhang, J. Zhang, and C. Pan, J. Phys. Chem. C **116**, 7515 (2012).

[130] C.A. Melendres, A. Narayanasamy, V.A. Maroni, and R.W. Siegel, J. Mater. Res. **4**, 1246 (1989).

[131] V. Swamy, B.C. Muddle, and Q. Dai, Appl. Phys. Lett. **89**, 163118 (2006).

[132] C.R. Aita, Appl. Phys. Lett. **90**, 213112 (2007).

[133] C.-H. Yang and Z.-Q. Ma, Appl. Opt. **51**, 5438 (2012).

[134] H.L. Ma, J.Y. Yang, Y. Dai, Y.B. Zhang, B. Lu, and G.H. Ma, Appl. Surf. Sci. **253**, 7497 (2007).

[135] S.E. Ahmed, J. Huso, J.R. Ritter, J. Igo, Y. Gu, and M.D. McCluskey, J. Vac. Sci. Technol. B **38**, 032203 (2020).

[136] P.P. Lottici, D. Bersani, M. Braghini, and A. Montenero, J. Mater. Sci. **28**, 177 (1993).

[137] P.C. Ricci, A. Casu, M. Salis, R. Corpino, and A. Anedda, J. Phys. Chem. C **114**, 14441 (2010).

[138] P.C. Ricci, C.M. Carbonaro, L. Stagi, M. Salis, A. Casu, S. Enzo, and F. Delogu, J. Phys. Chem. C **117**, 7850 (2013).

[139] H.H. Pham and L.-W. Wang, Phys. Chem. Chem. Phys. **17**, 541 (2015).

[140] C. Rath, P. Mohanty, A.C. Pandey, and N.C. Mishra, J. Phys. Appl. Phys. **42**, 205101 (2009).

[141] M.-H. Tsai, P. Shen, and S.-Y. Chen, J. Appl. Phys. **100**, 114313 (2006).

[142] K. Komaguchi, T. Maruoka, H. Nakano, I. Imae, Y. Ooyama, and Y. Harima, J. Phys. Chem. C **114**, 1240 (2010).

[143] O. Agirseven, D.T. Rivella, J.E.S. Haggerty, P.O. Berry, K. Diffendaffer, A. Patterson, J. Kreb, J.S. Mangum, B.P. Gorman, J.D. Perkins, B.R. Chen, L.T. Schelhas, and J. Tate, AIP Adv. **10**, 025109 (2020).

[144] F. Tuinstra and J.L. Koenig, J. Chem. Phys. **53**, 1126 (1970).

[145] F. Tuinstra and J.L. Koenig, J. Compos. Mater. **4**, 492 (1970).

[146] M. A. Pimenta, G. Dresselhaus, M. S. Dresselhaus, L. G. Cançado, A. Jorio, and R. Saito, Phys. Chem. Chem. Phys. **9**, 1276 (2007).

[147] G. Impellizzeri, V. Scuderi, L. Romano, E. Napolitani, R. Sanz, R. Carles, and V. Privitera, J. Appl. Phys. **117**, 105308 (2015).

[148] M. Vázquez Piñón, B. Cárdenas Benítez, B. Pramanick, V.H. Perez-Gonzalez, M.J. Madou, S.O. Martinez-Chapa, and H. Hwang, Sens. Actuators Phys. **262**, 10 (2017).

[149] S. Moser, L. Moreschini, J. Jaćimović, O.S. Barišić, H. Berger, A. Magrez, Y.J. Chang, K.S. Kim, A. Bostwick, E. Rotenberg, L. Forró, and M. Grioni, Phys. Rev. Lett. **110**, 196403 (2013).

[150] F. Bekisli, W.B. Fowler, and M. Stavola, Phys. Rev. B **86**, 155208 (2012).

[151] J. Daughtry, A.S. Alotabi, L. Howard-Fabretto, and G.G. Andersson, Nanoscale Adv. **3**, 1077 (2021).

[152] P. Phuinthiang, D.T.T. Trinh, D. Channei, K. Ratananikom, S. Sirilak, W. Khanitchaidecha, and A. Nakaruk, Nanomaterials **11**, 1493 (2021).

[153]*Photorefractive Materials and Their Applications 1*.

[154] R.H. Upadhyay, A.P. Argekar, and R.R. Deshmukh, Bull. Mater. Sci. **37**, 481 (2014).

[155] Y. Wei, Y. Song, X. Deng, B. Han, X. Zhang, Y. Shen, and Y. Lin, J. Mater. Sci. Technol. **30**, 743 (2014).

[156] P. Kumar Patel, J. Rani, N. Adhlakha, H. Singh, and K.L. Yadav, J. Phys. Chem. Solids **74**, 545 (2013).

[157] E. Krätzig, F. Welz, R. Orlowski, V. Doormann, and M. Rosenkranz, Solid State Commun. **34**, 817 (1980).

[158] A.R. Johnston, J. Appl. Phys. **42**, 3501 (1971).

[159] V.S. Puli, Mater Res Bull **46**, 2527 (2011).

[160] V.S. Puli, A. Kumar, D.B. Chrisey, M. Tomozawa, J.F. Scott, and R.S. Katiyar, J. Phys. Appl. Phys. **44**, 395403 (2011).

[161] W. Liu and X. Ren, Phys. Rev. Lett. **103**, 257602 (2009).

[162] D.E. Rase and R. Roy, J. Am. Ceram. Soc. **38**, 102 (1955).

[163] A. von Hippel, *HIGH DIELECTRIC CONSTANT MATERIALS AND FERROELECTRICITY* (MASSACHUSETTS INST OF TECH CAMBRIDGE LAB FOR INSULATION RESEARCH, 1963).

[164] J.P. Remeika and W.M. Jackson, J. Am. Chem. Soc. **76**, 940 (1954).

[165] P.G. Schunemann, D.A. Temple, R.S. Hathcock, H.L. Tuller, H.P. Jenssen, D.R. Gabbe, and C. Warde, JOSA B **5**, 1685 (1988).

[166] D. Rytz, B.A. Wechsler, C.C. Nelson, and K.W. Kirby, J. Cryst. Growth **99**, 864 (1990).

[167] S. Ajimura, K. Tomomatsu, O. Nakao, A. Kurosaka, H. Tominaga, and O. Fukuda, JOSA B **9**, 1609 (1992).

[168] H. Kishi, Y. Mizuno, and H. Chazono, Jpn. J. Appl. Phys. **42**, 1 (2003).

[169] M.T. Buscaglia, V. Buscaglia, M. Viviani, P. Nanni, and M. Hanuskova, J. Eur. Ceram. Soc. **20**, 1997 (2000).

[170] K. Asokan, J.C. Jan, J.W. Chiou, W.F. Pong, P.K. Tseng, I.N. Lin, and IUCr, J. Synchrotron Radiat. **8**, (2001).

[171] Z. Yu, C. Ang, R. Guo, and A.S. Bhalla, Mater. Lett. **61**, 326 (2007).

[172] L. Zhang, O.P. Thakur, A. Feteira, G.M. Keith, A.G. Mould, D.C. Sinclair, and A.R. West, Appl. Phys. Lett. **90**, 142914 (2007).

[173] D.F.K. Hennings and H. Schreinemacher, J. Eur. Ceram. Soc. **15**, 795 (1995).

[174] S. Lee, W.H. Woodford, and C.A. Randall, Appl. Phys. Lett. **92**, 201909 (2008).

[175] R.C. Pullar, Y. Zhang, L. Chen, S. Yang, J.R.G. Evans, A.N. Salak, D.A. Kiselev, A.L. Kholkin, V.M. Ferreira, and N.McN. Alford, J. Electroceramics **22**, 245 (2009).

[176] M.R. Panigrahi and S. Panigrahi, Phys. B Condens. Matter **405**, 2556 (2010).

[177] F.V. Motta, A.P.A. Marques, J.W.M. Espinosa, P.S. Pizani, E. Longo, and J.A. Varela, Curr. Appl. Phys. **10**, 16 (2010).

[178] V.M. Poole, C.D. Corolewski, and M.D. McCluskey, AIP Adv. **5**, 127217 (2015).

[179] V.M. Poole, S.J. Jokela, and M.D. McCluskey, Sci. Rep. **7**, 6659 (2017).

[180] D.V. Lang and R.A. Logan, Phys. Rev. Lett. **39**, 635 (1977).

[181] M.T. Hirsch, J.A. Wolk, W. Walukiewicz, and E.E. Haller, Appl. Phys. Lett. **71**, 1098 (1997).

[182] J.Z. Li, J.Y. Lin, H.X. Jiang, J.F. Geisz, and S.R. Kurtz, Appl. Phys. Lett. **75**, 1899 (1999).

[183] Z. Zhang and A. Janotti, Phys. Rev. Lett. **125**, 126404 (2020).

[184] I.B. Ouni, D. Chapron, H. Aroui, and M.D. Fontana, J. Appl. Phys. **121**, 114102 (2017).

[185] Y. Yang, H. Hao, L. Zhang, C. Chen, Z. Luo, Z. Liu, Z. Yao, M. Cao, and H. Liu, Ceram. Int. **44**, 11109 (2018).

[186] W.S. Baer, Phys. Rev. **144**, 734 (1966).